

Winter 1997

Response of outer radiation belt electrons to a magnetic storm

Donald Hugh Brautigam
University of New Hampshire, Durham

Follow this and additional works at: <https://scholars.unh.edu/dissertation>

Recommended Citation

Brautigam, Donald Hugh, "Response of outer radiation belt electrons to a magnetic storm" (1997). *Doctoral Dissertations*. 1988.
<https://scholars.unh.edu/dissertation/1988>

This Dissertation is brought to you for free and open access by the Student Scholarship at University of New Hampshire Scholars' Repository. It has been accepted for inclusion in Doctoral Dissertations by an authorized administrator of University of New Hampshire Scholars' Repository. For more information, please contact nicole.hentz@unh.edu.

INFORMATION TO USERS

This manuscript has been reproduced from the microfilm master. UMI films the text directly from the original or copy submitted. Thus, some thesis and dissertation copies are in typewriter face, while others may be from any type of computer printer.

The quality of this reproduction is dependent upon the quality of the copy submitted. Broken or indistinct print, colored or poor quality illustrations and photographs, print bleedthrough, substandard margins, and improper alignment can adversely affect reproduction.

In the unlikely event that the author did not send UMI a complete manuscript and there are missing pages, these will be noted. Also, if unauthorized copyright material had to be removed, a note will indicate the deletion.

Oversize materials (e.g., maps, drawings, charts) are reproduced by sectioning the original, beginning at the upper left-hand corner and continuing from left to right in equal sections with small overlaps. Each original is also photographed in one exposure and is included in reduced form at the back of the book.

Photographs included in the original manuscript have been reproduced xerographically in this copy. Higher quality 6" x 9" black and white photographic prints are available for any photographs or illustrations appearing in this copy for an additional charge. Contact UMI directly to order.

UMI

A Bell & Howell Information Company
300 North Zeeb Road, Ann Arbor MI 48106-1346 USA
313/761-4700 800/521-0600

**RESPONSE OF OUTER RADIATION BELT ELECTRONS
TO A MAGNETIC STORM**

BY

DONALD HUGH BRAUTIGAM
B.S., University of New Hampshire, 1977
M.S., University of New Hampshire, 1980

DISSERTATION

Submitted to the University of New Hampshire
in Partial Fulfillment of
the Requirements for the Degree of

Doctor of Philosophy

in

Physics

December, 1997

UMI Number: 9819671

**UMI Microform 9819671
Copyright 1998, by UMI Company. All rights reserved.**

**This microform edition is protected against unauthorized
copying under Title 17, United States Code.**

UMI
300 North Zeeb Road
Ann Arbor, MI 48103

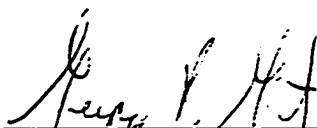
This dissertation has been examined and approved.



Dissertation Director, Lynn M. Kistler
Associate Research Professor of Physics and the
Institute for the Study of Earth, Oceans, and Space



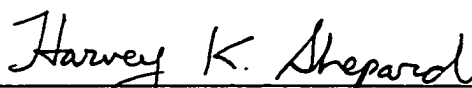
Terry G. Forbes
Research Professor of Physics and the
Institute for the Study of Earth, Oceans, and Space



Gregory P. Ganet
Air Force Research Laboratory



M. Susan Gussenhoven
Air Force Research Laboratory



Harvey K. Shepard
Professor of Physics

11/26/97

Date

I
dedicate
this thesis to
my parents, Rena and Mike
my wife, Beth
and my daughters, Misa, Shana, and Naomi

ACKNOWLEDGEMENTS

I would first like to thank my supervisor at the Air Force Research Laboratory (AFRL), Gary Mullen, and Sue Gussenhoven, both of whom were impressed enough with my initial work for them to encourage me to return to school to obtain my doctoral degree. This thesis was made possible through the Air Force's Long Term-Full Time Training program which generously funded my years at UNH. I thank Gary for his patience over the years while I struggled to find an appropriate research topic. I trust that my extended sabbatical from normal duties will pay off; now my 'real' work begins.

I am also grateful to my advisor, Dr. Lynn Kistler, who helped me focus on and jump start the writing process - long before I knew what the final punch line of this thesis would be. I would also like to thank my other committee members, Drs. Terry Forbes and Harvey Shepard from UNH, and Drs. Greg Ginnet and Sue Gussenhoven from AFRL, for reading through my thesis and providing helpful comments and corrections.

The numerous 'theory meetings' held at AFRL with Drs. Jay Albert and Bob Hilmer from Boston College, and Drs. Greg Ginnet and Sue Gussenhoven helped me move along the radiation belt diffusion theory learning curve. I am particularly indebted to Jay and Bob for providing me with computer code. I also would like to thank Dan Madden of Boston College for helping me out greatly with CRRES data processing.

Finally, thanks to Carolyn Jordan, an ex-AFRL colleague and friend, now a UNH graduate student, who shared many a physics class with me and helped me to re-enter the classroom scene; and to the lunchtime 'Ultimate' players who helped me celebrate!!

TABLE OF CONTENTS

DEDICATION	iii
ACKNOWLEDGEMENTS	iv
TABLE OF CONTENTS	v
LIST OF TABLES	viii
LIST OF FIGURES	ix
ABSTRACT	xi
CHAPTER	PAGE
1. INTRODUCTION	1
2. DISCOVERY OF THE VAN ALLEN RADIATION BELTS	7
3. THE SOLAR - MAGNETOSPHERE SYSTEM	16
4. THEORETICAL BACKGROUND	22
4.0 Introduction	22
4.1 Test Particle Motion	22
4.2 Guiding Center Approximation	25
4.3 Equatorial Drifts	28
4.4 Adiabatic Invariants	29
4.5 The 'L' Parameter	31
4.6 Kinetic Theory	33
5. GENERIC MAGNETIC STORM PHENOMENOLOGY	36
6. OVERVIEW OF ELECTRON RADIATION BELT RESEARCH	38
6.0 Introduction	38
6.1 False Starts	38
6.2 Early Observations of Magnetic Storm Effects	39
6.3 Adiabatic Variations	41
6.4 Non-Adiabatic Processes / Diffusive	43

6.5	Non-Adiabatic Processes / Impulsive	44
6.6	High Speed Solar Wind Streams	45
7.	RADIATION BELT DIFFUSION	48
7.0	Introduction.....	48
7.1	Radial Diffusion.....	49
7.2	Pitch Angle Diffusion.....	59
7.3	Multi-Modal Diffusion.....	66
7.4	Radial Diffusion Coefficients (Semi-empirical)	69
	Derivations of D_{LL}^M	71
	Derivations of D_{LL}^E	74
	Derivations of D_{LL}^P	76
	Comparison of D_{LL}	80
7.5	Summary of Diffusion Topics	83
8.	DIFFUSION MODELING.....	85
9.	DATABASES.....	89
9.0	Introduction.....	89
9.1	CRRES Electron Magnetic Spectrometer.....	91
9.2	CRRES Fluxgate Magnetometer	92
9.3	CRRES Electric Field / Langmuir Probe Instrument.....	93
9.4	CRRES Plasma Wave Experiment	94
9.5	Solar Wind / Magnetospheric Activity Indices.....	94
9.6	Los Alamos Geosynchronous Electrons	95
10.	SURVEY OF MAGNETIC STORM	97
10.0	Introduction.....	97
10.1	Interplanetary and Magnetospheric Parameters versus Electron Fluxes...97	
10.2	Quasi-Static Electric Field	110
11.	MAGNETIC FIELD MODEL	113
11.0	Introduction.....	113
11.1	Selection of Magnetic Field Model.....	114
11.2	Tsyganenko 1989 Magnetic Field Model.....	117
11.3	Comparison With CRRES Measurements	118
12.	TRANSFORMATION OF $j(X,E,\alpha)$ TO $f(\mu,J,L^*)$	127
13.	STORM ADIABATIC VARIATIONS.....	132
13.0	Introduction.....	132
13.1	Adiabatic Variation in Flux at Fixed Position and Energy	133
13.2	Evidence for Non-Adiabatic Flux Losses.....	140

14.	STORM DYNAMICS.....	143
14.0	Introduction.....	143
14.1	Phase Space Density Survey	144
14.2	Time Dependent D_{LL}	148
	Time Dependent D_{LL}^E	149
	Time Dependent D_{LL}^M	153
14.3	Radial Diffusion Modeling: Algorithm	154
14.4	Radial Diffusion Modeling: Parameterization	155
14.5	Radial Diffusion Modeling: Results	158
15.	SUMMARY AND DISCUSSION.....	167
15.0	Summary	168
15.1	Inner Source for >1 MeV Electrons.....	169
15.2	Pitch Angle Dependent Diffusion Coefficients.....	174
15.3	Injections.....	176
16.	CONCLUSIONS	178
	LIST OF REFERENCES.....	180
	Appendix A: COORDINATE SYSTEMS	191
	Appendix B COMPUTER PROGRAM FLOW DIAGRAMS	192

LIST OF TABLES

7. Radiation Belt Diffusion Research

Table 7.1: Radial Diffusion Coefficient Summary	80
---	----

11. Magnetic Field Model

Table 11.1: CRRES and Model Magnetic Field Comparisons	116
--	-----

LIST OF FIGURES

1. INTRODUCTION

Figure 1.1 CRRESRAD radiation dose models [*Kerns and Gussenhoven, 1992*].....2

2. DISCOVERY OF THE VAN ALLEN RADIATION BELTS

Figure 2.1: Data from Explorer III [*Van Allen, et al., 1958*]10

Figure 2.2: Single radiation belt intensity contours [*Van Allen, et al., 1959*].....12

Figure 2.3: Double radiation belt intensity contours [*Van Allen, 1959*].....13

3. THE SOLAR-MAGNETOSPHERE SYSTEM

Figure 3.1: Schematic of magnetospheric boundaries [*Lyons and Williams, 1984*] ...18

Figure 3.2 Convection plus corotation electric fields [*Lyons and Williams, 1984*]...21

4. THEORETICAL BACKGROUND

Figure 4.1: The fundamental periodicities [*Spjeldvik and Rothwell, 1985*].....25

Figure 4.2 L dependence of gyro, bounce, and drift frequencies27

Figure 4.3: Equatorial magnetic field contours [*Fairfield, 1968*]29

Figure 4.4 Dipole field line coordinates [*Roederer, 1970*]32

7. RADIATION BELT DIFFUSION

Figure 7.1 Empirical electron lifetimes [*Roberts, 1968*].....63

Figure 7.2a Theoretical electron lifetimes [*Lyons, et al., 1972*].....66

Figure 7.2b Theoretical and empirical electron lifetimes [*Lyons, et al., 1972*].....66

Figure 7.3: Classic flux profile signature of radial diffusion [*Frank, et al., 1964*]70

Figure 7.4 Dependence of D^M_o on K_p ($L=4$) [*Lanzerotti and Morgan, 1973*]73

Figure 7.5: Dependence of D^M_o on K_p ($L=6$) [*Lanzerotti, et al., 1978*]73

Figure 7.6: Flux profiles used for inferring D^{P}_{LL} [*Lanzerotti, et al., 1970*]78

Figure 7.7: Composite plot of radial diffusion coefficients ($K_p=1$)81

9. DATABASES

Figure 9.1 CRRES orbit and LANL geosynchronous satellite orbit90

10. SURVEY OF 9 OCTOBER 1990 MAGNETIC STORM

Figure 10.1: Survey of interplanetary parameters99

Figure 10.2: Survey of magnetospheric parameters and electron flux101

Figure 10.3: Survey of LANL geosynchronous electron flux.....102

Figure 10.4: Orbit 186 survey of 0.27 MeV electron flux with injection106

Figure 10.5: Survey of electron flux.....109

Figure 10.6: Electric field survey for orbits 183-186 and 189-190112

11. Magnetic Field Model

Figure 11.1: Model magnetic field line profiles [Tsyganenko, 1989].....	117
Figure 11.2a: Comparison of IGRF85, T89, and CRRES (orbits 182).....	122
Figure 11.2b: Comparison of IGRF85, T89, and CRRES (orbits 184).....	123
Figure 11.2c: Comparison of IGRF85, T89, and CRRES (orbits 185).....	124
Figure 11.2d: Comparison of IGRF85, T89, and CRRES (orbits 186).....	125
Figure 11.2e: Comparison of IGRF85, T89, and CRRES (orbits 204).....	126

12. Transformation of $j(X,E,\alpha)$ to $f(\mu,J,L^*)$

Figure 12.1: Overall data processing scheme for transforming $j(X,E,\alpha)$ to $f(\mu,J,L^*)$..	128
Figure 12.2: Second invariant (J) dependence on equatorial pitch angle	130
Figure 12.3: First invariant (μ) dependence on energy.....	131

13. Storm Adiabatic Variations

Figure 13.1: Comparison of orbit 182 and 185 parameters.....	134
Figure 13.2: Drift shells at $K_p=1,5$ for (a) $L^*=3.93$ and (b) $L^*=5.44$	135
Figure 13.3a: Comparison of observed and theoretical spectra (orbits 182, 185).....	138
Figure 13.3b: Comparison of observed and theoretical spectra (orbits 182, 185).....	139
Figure 13.4: Observed 'butterfly' pitch angle distribution.....	141

14. Storm Dynamics

Figure 14.1 Survey of phase space density.....	145
Figure 14.2 J dependence of $f(\mu,J,L^*,t)$	147
Figure 14.3 DC convection electric field [Rowland and Wygant, 1997].....	150
Figure 14.4 Average E_{ms} as a function of K_p	151
Figure 14.5: D_{LL}^E as a function of L and K_p	153
Figure 14.6: D_{LL}^M as a function of L and K_p	153
Figure 14.7: Electron lifetimes versus L for $\mu=100 - 1000$ MeV/G.....	156
Figure 14.8 Radial diffusion results for ($\mu=100$ MeV/G).....	159
Figure 14.9 Radial diffusion results for ($\mu=1000$ MeV/G).....	162
Figure 14.10 Comparison of empirical and model $f(L)$ for orbit 189.....	164
Figure 14.11 Comparison of empirical and model $f(L)$ for orbit 204.....	165

15. Discussion

Figure 15.1: Plasma wave survey for orbits 182 and 192.....	171
---	-----

Appendix B

Figure B.1: Flow diagram for <i>roederer.f</i>	193
Figure B.2: Flow diagram for <i>aibin.c</i>	194
Figure B.3: Flow diagram for <i>rdiffuse.f</i>	195

ABSTRACT

RESPONSE OF OUTER RADIATION BELT ELECTRONS TO A MAGNETIC STORM

by

Donald Hugh Brautigam
University of New Hampshire, December, 1997

To advance our understanding of the magnetic storm dynamics of the outer radiation belt relativistic electrons, the magnetic storm which commenced on 9 October 1990 was analyzed in detail using data from the Combined Release and Radiation Effects Satellite (CRRES) and the Los Alamos National Laboratory geosynchronous satellite 1989_046. Electron differential flux was transformed into phase space density as a function of the three adiabatic invariants. The invariants were determined by magnetic field data from CRRES and the Tsyganenko 1989 K_p driven model. The unique work of this thesis is the storm time radial diffusion modeling performed using time dependent radial diffusion coefficients (D_{LL}) and a time dependent outer boundary condition. The results show that $D_{LL}(t)$, parameterized by K_p, can efficiently couple outer boundary condition variations (sources and sinks) to deep into the radiation belt interior, thus accounting for both significant flux decreases and increases throughout the region. It was found that an internal source is required to account for the gradual increase in the highest energy electrons throughout the recovery phase. A potential source mechanism is energy diffusion via wave particle interactions with whistler chorus waves which were observed by CRRES to be greatly enhanced throughout the recovery phase.

CHAPTER 1

INTRODUCTION

When one looks up at the stars at night, one perceives the vast space between the Earth and the stars as a great empty void. Yet we now know that this is far from the truth. In particular, the 'near-Earth-space', that region which is home to increasingly more and more satellite traffic, is home to numerous populations of charged particles which participate in an intricate balance of energy between the Sun and the Earth. Those electrons and protons which orbit the Earth, trapped within the confines of its magnetic field, are collectively known as the Van Allen radiation belts, named after the scientist credited with their discovery in 1958, Dr. James Van Allen.

As traditionally described, the radiation belts form a two zone structure, envisioned as two concentric doughnuts centered about the Earth, symmetric about the Earth's magnetic equator. This clear separation into two distinct zones is somewhat artificial and overly simplistic since the distinction is strongly dependent upon the particle species and energy ranges being considered, as well as upon the magnetospheric activity at the moment and recent past. However, empirical radiation dose models help sharpen the definition of the two zone structure.

Figure 1.1 shows two CRRESRAD models [*Kerns and Gussenhoven, 1992*; *Gussenhoven, et al., 1992*] giving average dose maps produced from data taken over an

eight month period from two dosimeter channels on the CRRES satellite. Both models give average dose rates (Rads per second) received behind a specified shielding thickness (82.5 mils of aluminum) within $8 R_E$ of the Earth (azimuthal symmetry about the Earth is assumed). The top panel is a map of average dose rates from a channel which measured the response to >20 MeV protons. The bottom panel is a map of average dose rates from a channel which measured the response to both >1 MeV electrons and >100 MeV protons (the >100 MeV protons are limited to the inner zone).

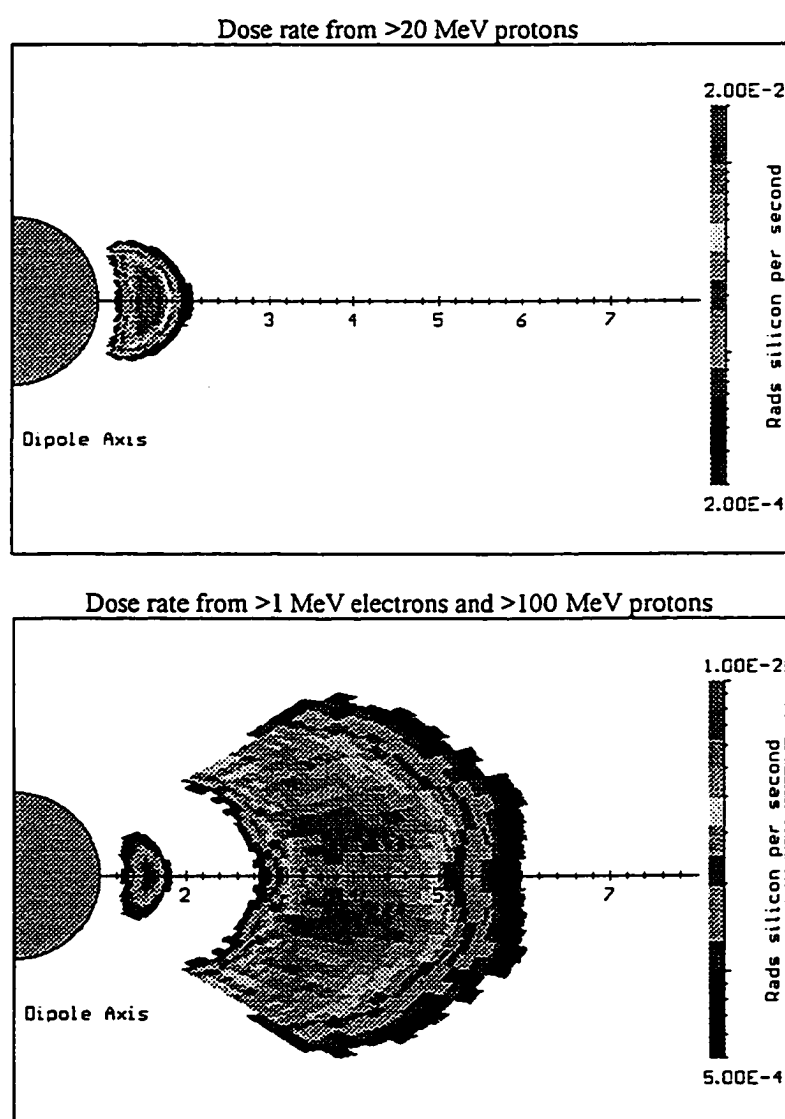


Figure 1.1 : CRRESRAD radiation dose rate models [*Kerns and Gussenhoven, 1992*].

From these dose maps, the separation of the radiation belts into two distinct zones is clear. Considering the dose rates from protons and electrons at these energies, the inner zone extends from ~ 1.2 to $\sim 2.5 R_E$ ($R_E \equiv$ Earth radius = 6371 km) and is dominated by >20 MeV protons. There are still large uncertainties in the intensity of the >1 MeV electron population in the inner zone (bottom panel). The outer zone (bottom panel) extends from ~ 2.8 to $\sim 6.8 R_E$, where the primary source of dose shown is from >1 MeV electrons. In the bottom panel, the region from ~ 2 to $2.8 R_E$ is void of significant dose and is referred to as the slot region. Relative to the inner zone, the outer zone electrons are an extremely variable population, with intensities varying by orders of magnitude within a time scale of hours. During very large magnetic disturbances, the slot region is filled by intense radiation.

Understanding the morphology and dynamics of the radiation belt particle populations is not only of academic interest, but is also of great practical importance. The network of satellites in orbit is growing at a fast pace. Once only the realm of government surveillance and weather satellites, an increasing number of commercial communication satellites now pass through the radiation belts which represent a hazardous environment to on board radiation-sensitive microelectronic devices.

Statistical, long term average static models of the electron [Vette, 1991] and proton [Sawyer and Vette, 1976] radiation belts were developed from satellite data collected over the 1960s and 1970s. A theoretical framework for interpreting the long term average features of the radiation belts was well established by the early 1970s [Northrop, 1963; Roederer, 1970; Schulz and Lanzerotti, 1974], and research in the field

subsequently declined significantly. However, in 1990, a joint effort by the USAF and NASA led to the launch of the Chemical Release and Radiation Effects Satellite (CRRES). One of CRRES's primary goals was to accurately characterize the radiation belt environment and its effect on a wide range of microelectronic devices. Despite CRRES's premature failure after a 14 month lifetime, its unprecedented observations of an extraordinary magnetospheric event may be credited with the recent revival in radiation belt studies. On 23 March 1991, a large solar proton event reached the Earth, followed shortly thereafter, by a very large solar wind shock. CRRES was fortuitously positioned to witness the dramatic creation of a secondary high energy proton belt [Mullen and Gussenhoven, 1991], and the equally dramatic injection (acceleration) of an electron population up to 15 MeV deep in the slot region [Blake, *et al.*, 1992]. This event helped spawn a new wave of interest and research in radiation belt dynamics.

Not only has the CRRES mission lead to new statistical radiation belt models [Brautigam, *et al.*, 1992; Gussenhoven, *et al.*, 1996a; Gussenhoven, *et al.*, 1996b], but it still offers an unprecedented opportunity to further our understanding of radiation belt dynamics. With its extensive array of instruments, CRRES provides detailed measurements of not only the radiation belt electron (and proton) populations, but also the magnetic field which controls the motion of high energy charged particles to zeroth order, and the electromagnetic waves which randomly perturb this motion and result in various modes of particle transport.

This thesis will examine in detail the response of the outer zone relativistic electrons, as observed by CRRES, to the moderate magnetic storm whose storm sudden

commencement (SSC) occurred on 9 October 1990. The response of the outer zone electrons during all phases of the storm will be explored, including the initial depletion of electrons during the initial and main phase of the storm, the rapid injection of 100s keV electrons following the onset of the recovery phase, and the gradual increase in intensity of the ~ 1 MeV electrons throughout the recovery phase.

The uniqueness of this work lies in both the extensive CRRES data sets available and in the approach followed in modeling the radial diffusion process throughout the entire storm period. The dynamic variations of the outer zone electrons throughout an entire magnetic storm have never been modeled in such detail as here, with time dependent radial diffusion coefficients and boundary conditions. A chapter outline of this thesis follows.

Chapter 2 presents a brief history leading up to and including the discovery of the radiation belts. Chapter 3 introduces the solar-magnetosphere system fundamentals which are key to understanding the mechanisms which drive the radiation belt dynamics. Chapter 4 discusses introductory concepts necessary for understanding radiation belt diffusion theory, and Chapter 5 outlines the phenomenology and physics of a generic magnetic storm. Chapter 6 provides a broad overview of the areas of radiation belt electron research that have been pursued in the past, and includes some of the most recent studies. A more detailed investigation of the research which has lead to the radiation belt diffusion paradigm, including results which are used in later chapters, is presented in Chapter 7. A discussion of previous diffusion modeling studies is given in Chapter 8. Details of the satellite orbits and data bases used for this study are presented

in Chapter 9. Chapter 10 provides an overview of the 9 October 1990 magnetic storm. The selection of the magnetic field model used in this analysis, and a comparison with CRRES measurements, is covered in Chapter 11. The computer algorithms employed to calculate the adiabatic invariants, and the procedures for binning the data, will be discussed in Chapter 12. The degree to which adiabatic variations are able to account for the flux dropout during the main phase of the storm period is determined in Chapter 13. Chapter 14 models the non-adiabatic behavior throughout the storm in terms of time dependent radial diffusion. Finally, the results will be discussed in Chapter 15, and conclusions drawn in Chapter 16.

CHAPTER 2

DISCOVERY OF THE VAN ALLEN RADIATION BELTS

The study of the charged particle environment in the upper atmosphere was well under way during the early 1900s and provided the necessary backdrop for the imminent discovery of the radiation belts. During the pre-WWI years, V.F. Hess was responsible for a series of balloon flights designed to investigate the radiation environment of the upper atmosphere. He found that the intensity decreased from the surface of the Earth to about 2000 feet (as expected assuming a ground source), but then began to increase to at least the balloons' maximum altitude of 30,000 feet. Based upon this intensity profile, Hess proposed that what was being measured was an extremely energetic form of radiation from outer space. R.A. Millikan coined the term 'cosmic radiation' to describe this radiation [Haymes, 1971].

Cosmic ray research escalated throughout the 1930s, with a brief interlude during WWII, and then picked up again in the late 1940s. In 1945, the US Army transferred a large surplus of German V-2 rocket components back to the US to assemble and test. A panel (including James Van Allen) was established to promote the scientific utilization of these rockets. The test flights of the V-2 rockets beginning in 1946 was a significant landmark in the rocket launching of scientific payloads. During the years 1952-1957, Van Allen utilized a hybridized form of launching referred to as a "rockoon" in which a

rocket would be carried aloft by a balloon to about 15 miles, and then fired up to a maximum altitude of about 60-70 miles. Van Allen used these rockoons to investigate the cosmic ray intensities at high latitudes. In 1953 two rockoon flights at auroral latitudes yielded an unexpected signature superimposed upon the typical cosmic ray signature. These were the first *in situ* measurements of 'soft auroral particle radiation' (~10 keV electrons) and provided the first glimpse into the yet to be discovered magnetosphere. [Van Allen, 1983].

On 1 February 1958, Van Allen and his team of researchers at the University of Iowa opened the door to magnetospheric research with a successful launch of the Explorer I satellite into an orbit with an inclination of 33° , a perigee of 360 km, and an apogee of 2500 km. There was a single Geiger counter on board, and the scientific objective was to create a global map of the cosmic radiation surrounding the Earth. The first data back from Explorer I was sparse because there was no on-board data recorder. Only 1 to 2 minute real-time data segments, telemetered down while passing directly overhead of select groundstations, were retained for archival. Several such passes showed cosmic ray count rates (extrapolated back to 100 km) which agreed with what the researchers were accustomed to from previous rocket flights. However, there were also several high altitude passes over South America which showed the count rate abruptly dropping to zero. The University of Iowa group were perplexed and could not explain the anomalous readings. Yet, with launch deadlines approaching for the following Explorer, the researchers felt that the routine analysis of the cosmic ray data would have to wait.

The data stream from Explorer I ceased on 15 March 1958. Explorer II was launched, but failed to achieve orbit and fell into the ocean. Explorer III was successfully launched on 26 March 1958 into an orbit very similar to Explorer I's. It carried a Geiger counter essentially identical to that on Explorer I, and also included a data tape recorder which enabled the acquisition of continuous data records throughout entire orbits. On 28 March, Van Allen obtained the first available data listing of a complete orbit. As recounted by Van Allen, "I put the record in my briefcase and returned to my hotel room, where, with the aid of graph paper, a ruler, and my slide rule, I worked out the counting rate of our Geiger tube as a function of time for a full 102-minute period and plotted the data." [Van Allen, 1983]. A version of this plot, which was the first explicit evidence of the newly discovered phenomenon, is provided here as Figure 2.1 [Van Allen, et al., 1958]. As in the case with Explorer I, Van Allen found that the Geiger counter would jump abruptly from the typical cosmic ray count rates, up to the counter's maximum rate, and then back down to near zero count rate. Van Allen sensed the tremendous implications of this plot. Conveying the excitement of discovery, he recalls that "At 3:00 A.M. I packed my work sheets and graph and turned in for the night with the conviction that our instruments on both *Explorers I and III* were working properly, and that we were encountering a mysterious physical effect of a real nature" [Van Allen, 1983]. The following day Van Allen returned to the University of Iowa to consult with two of his coworkers, Carl McIlwain and Ernest Ray, about his 'late night' plot of the orbit's anomalous signature. McIlwain had conducted tests on a prototype Geiger counter the previous day, so that when he was shown Van Allen's plot, it was

immediately apparent that Explorer I and III had passed through regions of very intense radiation, that the instrumentation was suffering severe dead-time effects, and that this was pushing the counting rate to its maximum and forcing a reset to nearly zero. The obvious, but profound conclusion, was that the anomalous readings were not the result of equipment error, but were “caused by a blanking of the Geiger tube by an intense radiation field.” [Van Allen, et al., 1958].

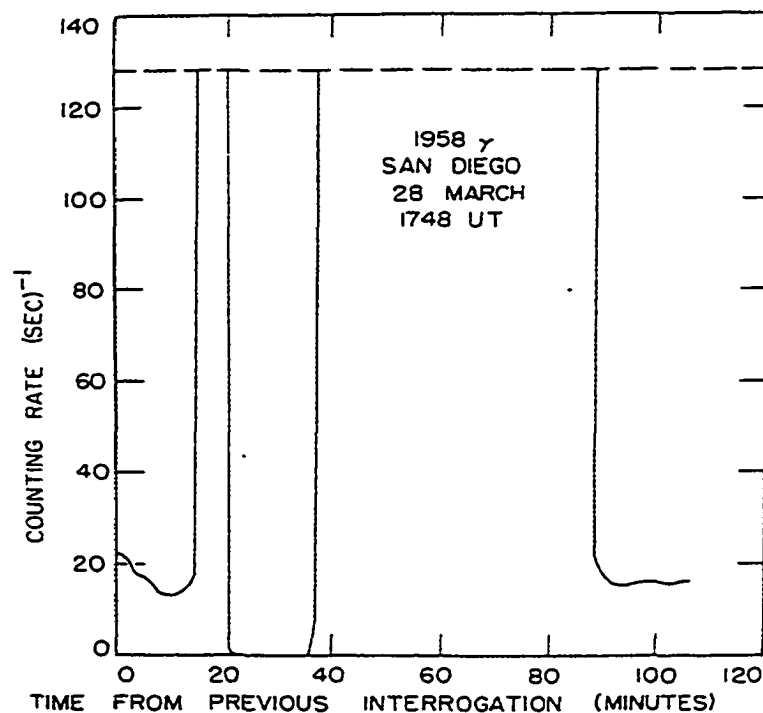


Figure 2.1 : Data from Explorer III showing cosmic ray count rates for the first ten minutes followed by anomalous recording due to instrument saturation upon entering the ‘yet to be discovered’ inner radiation belt [Van Allen, et al., 1958].

The exact nature of this ‘intense radiation field’ was not absolutely identified immediately, but it was largely assumed that it was due to charged particles. Because of past low altitude rocket observations of intense ‘soft auroral’ radiation, it was natural to speculate that the high intensity radiation detected by Explorer I and III was due to

auroral type particles with a mean energy of ~ 30 keV. The Geiger tubes, it was speculated, were responding to the bremsstrahlung produced in the satellite shell by the auroral electrons. An admittedly more remote possibility, was that the Geiger counter was responding to more energetic directly penetrating particles (protons > 35 MeV and/or electrons > 3 MeV). It wasn't until later that it was realized that this 'remote possibility' was in fact the correct explanation [O'Brien, et al., 1962].

Van Allen was familiar with the fundamentals of magnetically trapped particle motion from his earlier laboratory work at Princeton, and he concluded that the particle population which he and his research team had discovered were trapped in the Earth's magnetic field and were executing the three cyclical motions of gyration about a field line, field line bounce between magnetic poles, and azimuthal drift about the Earth. He also reasoned that as the particles moved to low altitudes during their bounce motion that their intensity would diminish due to their interaction with the denser atmosphere.

On 1 May 1958, Van Allen presented the above picture derived from the Explorer I and III findings to a joint session of the American Physical Society and the National Academy of Sciences. During the following press conference, a reporter, confronted with such cumbersome phrases as 'geomagnetically trapped corpuscular radiation' to describe the particle distribution encircling the Earth, asked Van Allen, "Do you mean like a belt?". With Van Allen's reply, "Yes, like a belt", the discovery of the Earth's radiation belt became history. That summer at the International Atomic Energy Agency meeting, Robert Jastrow coined the term *Van Allen radiation belt*.

At this point, based on Explorer I and III observations, the Van Allen radiation belt was just that, a single belt. Riding on the wave of excitement of the new discovery of the radiation belt, further satellite explorations were quickly planned. Explorer IV was launched on 26 July 1958, at a higher inclination (55°) than the previous Explorers but approximately the same apogee (2200 km). Explorer IV carried a shielded and an unshielded Geiger counter. The shielded counter responded to > 30 MeV protons, > 3 MeV electrons, and to > 50 keV bremsstrahlung x-rays. Pioneer III, was launched on 6 December 1958 into an orbit with an apogee of $1.09 \cdot 10^5$ km and carried two Geiger counters similar to the shielded detector flown on Explorer IV.

In early 1959, having analyzed the results from Explorer IV, Van Allen and his coworkers submitted a manuscript to the *Journal of Geophysical Research (JGR)* which was published in March [Van Allen, et al., 1959]. This article included a figure (reproduced here as Figure 2.2) which depicted a single radiation belt.

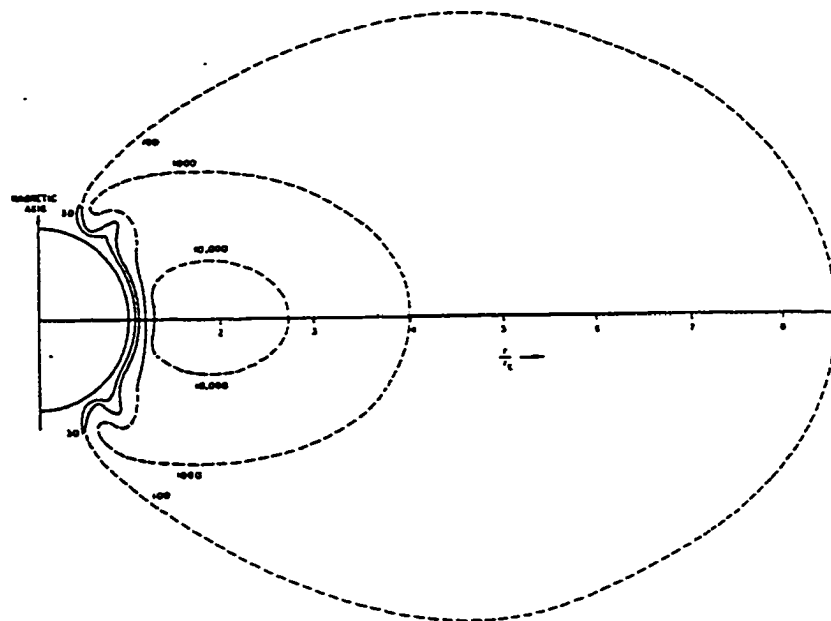


Figure 2.2 : Single radiation belt intensity contours based on Explorer IV measurements (solid curves) and as extended based on speculation (dashed curves) [Van Allen, et al., 1959].

figure are low altitude contours drawn from Explorer IV measurements (solid curves), as well as a speculative extension of these contours which were field-line-mapped out to the magnetic equator (dashed lines).

However, in the interim between the submission and publication of this *JGR* article, the single belt became a double belt. With the extensive low altitude (less than 2200 km) coverage of Explorer IV, and the high altitude observations from Pioneer III, came the realization that there were two distinct regions of radiation encircling the Earth. The first picture of the double belt structure of the radiation belts (reproduced here as Figure 2.3) appeared in the February issue of *Nature* [Van Allen and Frank, 1959].

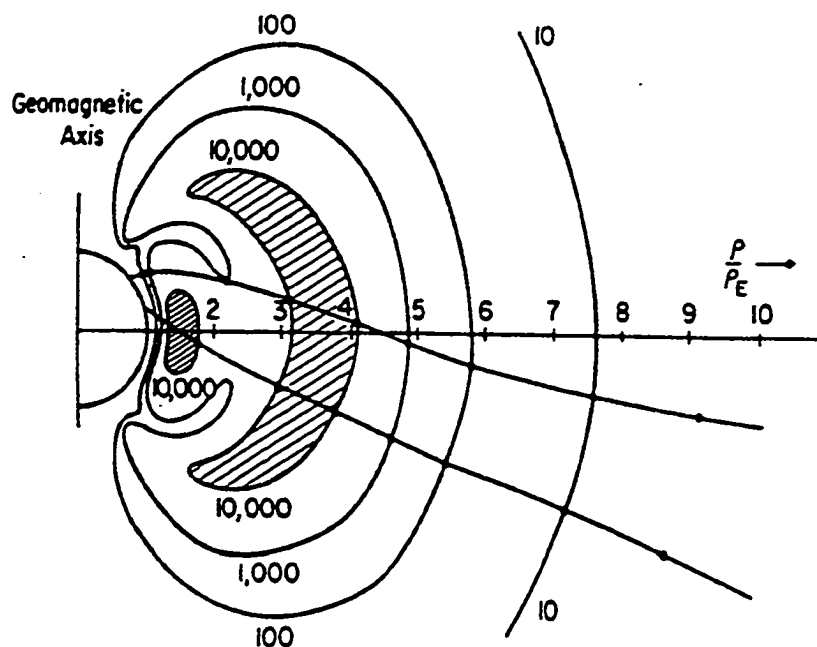


Figure 2.3 : Double radiation belt intensity contours based on Geiger counter data from Explorer IV and Pioneer III. [Van Allen, 1959].

The Pioneer III trajectory, going in and out through the heart of the inner and outer belts (shaded), is shown in dark lines. Accompanying the new figure of the by now double

radiation belt model, was the following note announcing the obsolescence of the single belt model described in the yet to be published (but already submitted) March issue of *JGR*:

In Fig. 8 of ref. 7 a speculative extension of the contours observed with Satellite ϵ [*Explorer IV*] was presented. The diagram given therein was one of two types which we had sketched as plausible extensions of the observed contours. The other one of the two, particularly advocated by C.E. McIlwain of this laboratory, regarded the high latitude, tongue-like contours as the tips of an outer, banana-shaped region (in meridian cross section). This view implied a second maximum in intensity as one passes outwards from the Earth in the plane of the geomagnetic equator. The new Pioneer III observations show that this second diagram is indeed more nearly true than the one previously published. [*Van Allen and Frank, 1959*]

A later issue of *JGR* [*Van Allen, 1959*] republished the figure depicting the two zone structure, and provided more extensive results from Explorer IV and Pioneer III, as well as from Pioneer IV which was launched on 3 March 1959. These new results helped to confirm the existence of the outer radiation belt in addition to the earlier discovered inner belt.

Whereas the inner zone fluxes observed by Pioneer IV were only a factor of 2-3 higher than those observed 15 months earlier by Pioneer III, the outer zone fluxes were up to two orders of magnitude higher. Thus, it was recognized that the inner belt is significantly more stable than the outer belt. It was also clear that the composition and energy spectra of the two belts are significantly different. The inner zone was believed to be comprised of mainly ~ 100 MeV protons and to a lesser degree, < 1 MeV electrons. The outer zone was erroneously thought to be largely populated by the < 100 keV

electrons related to the auroral phenomena observed throughout the earlier rocket programs.

There is very little doubt that the great outer zone and the rich variety of associated geophysical effects, including auroras, airglow, atmospheric heating, and geomagnetic storms, are directly attributable to solar gas injected into temporarily trapped orbits in the geomagnetic field. The mechanism for the acceleration of the particles therein to the observed energies constitutes a major unsettled problem. [*Van Allen*, 1959]

Today, almost four decades later, we know a great deal more about the composition and dynamics of the inner and outer Van Allen radiation belts. We now realize that the outer belt includes a population of > 1 MeV electrons, and yet the acceleration mechanism responsible for the presence of these relativistic electrons at geosynchronous altitude remains a 'major unsettled problem'.

CHAPTER 3

THE SOLAR - MAGNETOSPHERE SYSTEM

Although the radiation belt outer zone electrons are confined to a region within $10 R_E$ of the Earth, their dynamics are intimately tied to a much larger system including the Sun and its extended solar plasma and magnetic field which pervade interplanetary space. The purpose of this chapter is to provide a broad overview of this system and to introduce some of its key features which play a role in radiation belt dynamics. The material presented here is general information which can be found in many texts on space science and magnetospheric physics [*Lyons and Williams*, 1984; *Parks*, 1991; *Kivelson and Russell*, 1995].

The Sun is a continuous source of fully ionized electrically neutral plasma which continuously expands outward forming a rarefied extension of the solar corona known as the solar wind. The solar wind density (n_{sw}) and flow speed (V_{sw}) exhibit a wide dynamic range depending upon solar activity, which varies on both a short term (hourly) and long term (11 year cycle) time scale. In the vicinity of the Earth, n_{sw} typically ranges from 3 to 20 cm^{-3} ; and V_{sw} , from 300 to 800 km/s [*Parks*, 1991]. The upper limit of these typical ranges are often exceeded during relatively infrequent, but very large disturbances.

The Sun is a magnetized body, and the highly conducting solar wind carries the solar magnetic field lines (with one end remaining anchored in the Sun) with it as it flows out into interplanetary space, primarily along the ecliptic plane. The interplanetary magnetic field (IMF) magnitude at 1 AU ranges from 1 to 30 nT [Parks, 1991]. Because the Sun rotates with a 27 day period, the solar magnetic field lines form an interplanetary spiral sector structure as they expand radially outward with the solar wind.

The Earth is also a magnetized body, with a magnetic field generated by its core dynamo, and may be approximated by a dipole moment ($\sim .304 \text{ G R}_E^3$) tilted $\sim 11^\circ$ to the Earth's spin axis. If interplanetary space were a vacuum, the Earth's magnetic field would remain dipolar at large distances (falling off at a rate of r^{-3}) and 'near-Earth space' would be an axially symmetric, static, and rather boring environment. However, the Earth is embedded within the solar wind, and the continuous flow of magnetized solar plasma interacts with the Earth's dipole magnetic field in such a way as to confine it to a magnetic cavity enveloping the Earth known as the magnetosphere. The outer boundary of the magnetosphere, marked by the transition between the interplanetary magnetic and geomagnetic field, is referred to as the magnetopause. As the supersonic solar wind flow is interrupted by the presence of the Earth, a collisionless bow shock is formed upstream of the magnetopause. At this boundary, the solar wind is transformed to a thermalized subsonic plasma (magnetosheath) which flows by the magnetosphere before merging with the supersonic flow beyond the reaches of the magnetosphere. This flow of the shocked solar wind around the magnetopause boundary is represented schematically in Figure 3.1. Also shown in Figure 3.1 are various regions characterized by their particle

population. Found in the inner most region ($1 R_E < r < \sim 5 R_E$) on closed magnetic field lines is the plasmasphere which consists of a cold plasma (≤ 1 eV electrons and ions) that corotates with the Earth. Also found on closed magnetic field lines are the outer radiation belt electrons (0.1-10 MeV) and ring current (10-100 keV ions and electrons) which drift around the Earth in the region of $\sim 3.5 R_E < r < \sim 7 R_E$, overlapping and coexisting with the plasmasphere. Filling the extended nightside region of stretched magnetic field lines is the plasma sheet population of 1-10 keV particles which is responsible for the large scale magnetotail current that supports the tail's magnetic field topology.

In addition to the Earth's relatively constant internal field, the geomagnetic field has a highly variable external field component as a result of various magnetospheric current systems driven by the solar wind-magnetosphere coupling. The three major large scale magnetospheric current systems are the Chapman-Ferraro magnetopause surface currents, the ring current, and the magnetotail current. As discussed in Chapter 11, these variable currents lead to a time dependent external magnetic field which may be parameterized by the magnetic activity index $K_p(t)$ [Tsyganenko, 1989].

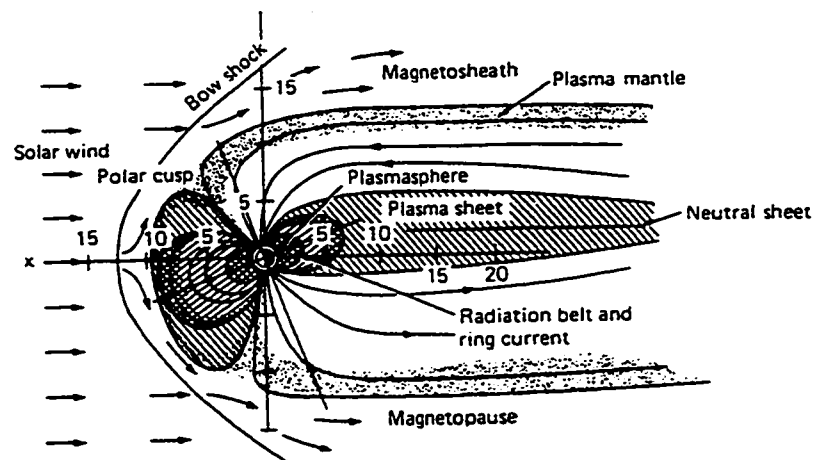


Figure 3.1 : Schematic of magnetospheric boundaries and regions [Lyons and Williams, 1984].

The approximate size and shape of the Earth's magnetosphere can be derived by equating the solar wind dynamic pressure ($p_{sw}=0.5 n_{sw}MV_{sw}^2$, M =ion mass) and the geomagnetic field energy density ($B^2/8\pi$). This analysis leads to a general agreement with observations showing a distorted dipole compressed on the dayside and stretched anti-sunward on the nightside by the solar wind flow [Ness, *et al.*, 1964]. Assuming that the solar wind impinges upon the magnetopause along the normal to the dayside surface, this pressure balance leads to the relation : $n_{sw}M V_{sw}^2 = B^2/4\pi$, where B is the magnetic field magnitude at the magnetopause. For a dipole field, with $B=B_0/r^3$ on the magnetic equator, this relation reduces to: $r = \left(\frac{B_0^2}{4\pi M} \right)^{\frac{1}{6}} (n_{sw} V_{sw}^2)^{-\frac{1}{6}}$. Because the dipole is only an approximation to the real geomagnetic field, a better fit to the dayside magnetopause stand-off distance (R_s) can be established by empirically determining the constant in front of the solar wind pressure term. A consensus was reached at the second Coordinated Data Analysis Workshop (CDAW 2) that the best overall agreement is found by setting the constant equal to 98, leading to the expression for approximating the stand-off distance [Olson and Pfitzer, 1982]:

$$R_s = 98 \cdot (n_{sw} V_{sw}^2)^{-1/6} \quad (2.1)$$

R_s estimates the equatorial radial distance between the Earth and the dayside magnetopause. With n_{sw} in ions/cm³ and V_{sw} in km/s, R_s is given in earth radii (R_E). The stand-off distance, and magnetopause boundary in general, is driven in and out by the fluctuating solar wind dynamic pressure. A stand-off distance representative of low solar wind pressure may be determined assuming a period of low solar wind density ($n_{sw} = 5$

cm^{-3}) and low solar wind speed ($V_{\text{sw}}=420 \text{ km/s}$), with a resultant stand-off distance of $R_s = 10 R_E$. In contrast to this 'relaxed' magnetosphere, there are occasional periods of relatively high solar wind pressure (i.e., associated with a solar wind shock) with, for an example, a relatively high solar wind density ($n_{\text{sw}}=30 \text{ cm}^{-3}$) and solar wind speed ($V_{\text{sw}}=625 \text{ km/s}$). Under such active conditions, the dayside magnetopause may be suddenly compressed to a distance of $R_s=6.5 R_E$, resulting in a sudden impulse (SI) ground signature in the global magnetic field. If a magnetic storm (a global magnetospheric disturbance to be more fully discussed in Chapter 5) follows this impulse, the perturbation is referred to as a storm sudden commencement (SSC). These magnetic perturbations (both small continuous fluctuations as well as larger less frequent ones) play a major role in radial diffusion, as shall be discussed in Chapter 7.

In addition to the Earth's magnetic field, there is a large scale magnetospheric electric field which arises from two sources - the solar wind and the rotation of the Earth. In the model of an open magnetosphere [Dungey, 1961], the condition of a southward directed interplanetary magnetic field (IMF) give rise to a class of 'open' magnetic field lines which have one end anchored in the magnetic polar cap region of the Earth and the other end connected to the IMF. The solar wind flowing across these open field lines lead to an electric field $\mathbf{E}_{\text{IMF}} = -\mathbf{V}_{\text{sw}} \times \mathbf{B}_{\text{IMF}}$ which is mapped down to the ionosphere resulting in a cross polar cap potential. Because of the topology of the Earth's open and closed field lines, the \mathbf{E}_{IMF} results in differential charging between the dawn and dusk side of the closed magnetosphere. The end result is a large scale dawn-to-dusk convection electric field, \mathbf{E}_C , imposed across the magnetosphere which convects

magnetospheric plasma sunward [Lyons and Williams, 1984]. The leftmost panel of Figure 3.2 [Lyons and Williams, 1984] shows the equipotentials of a uniform E_C pointing in the dawn-to-dusk direction. The role which the fluctuations of this convection electric field plays in driving radial diffusion will be discussed in Chapter 7. Besides the E_C , there is a second component to the magnetosphere's electric field. The corotation electric field E_R is the consequence of the corotation of the plasmasphere with the Earth [Lyons and Williams, 1984]. The middle panel of Figure 3.2 shows the equipotentials of E_R which encircle the Earth, producing a radially inward electric field. The sum of these two electric fields is shown in the rightmost panel, and leads to an E which is responsible for the ring current to be discussed in Chapter 5.

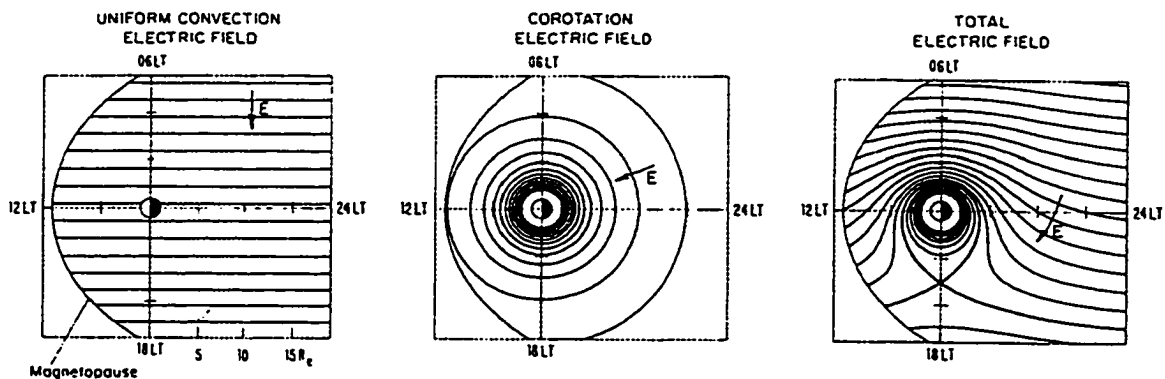


Figure 3.2 : Convection plus corotation electric fields [Lyons and Williams, 1984].

CHAPTER 4

THEORETICAL BACKGROUND

4.0 Introduction

At the time of the Van Allen radiation belt discovery, most of the mathematical tools for analyzing charged particle motion in the Earth's magnetic field were available.

Stormer [1955] explored test particle motion in a dipole field using the Lorentz force equation in his studies of cosmic ray trajectories. *Alfven* [1950] developed the very fruitful guiding center approximation which built upon the three fundamental periodic motions of charged particles in a magnetic field. *Rosenbluth and Longmire* [1957] recognized the significance of casting the guiding center drift motions into the framework of action-angle variables and adiabatic invariants. These fundamental theoretical developments are the backbone for the description of radiation belt particle dynamics, and they will be briefly discussed below.

4.1 Test Particle Motion

Charged particles moving in an electric (**E**) and magnetic (**B**) field with momentum (**p**) obey the Lorentz force equation (q =charge, v =velocity, c =speed of light):

$$\frac{d\vec{p}}{dt} = q[\vec{E} + \vec{v} \times \vec{B}] \quad (4.1)$$

When one deals with an entire ensemble of charged particles, including both ions and electrons, there are individual as well as collective modes of motion. The differential motion of ions and electrons can dramatically alter the initial electric fields (through charge separation) and magnetic fields (through currents). Solving the Lorentz force equation (Equation 4.1) in a fully self-consistent manner, whereby the motion of the particles alter the fields which in turn alter the particle trajectories, is an extremely difficult task. However, in the case of radiation belt particles, which constitute the high energy tail of the magnetospheric particle distribution, it is assumed that these complexities may be ignored and that the study of particle motion may be approximated in terms of individual test particle trajectories in external fields.

Theoretical analysis of radiation belt particles often assumes the most idealized form of the geomagnetic field, a static dipole field. The earth's internal magnetic field may be idealized by a magnetic dipole with a magnetic moment of $k_o=0.311 \text{ G}\cdot\text{R}_E^3$. Much of radiation belt theory begins with this approximation because it greatly simplifies the problem while maintaining many of the important features that a more realistic magnetosphere would yield. The dipole field may be represented in spherical coordinates, using latitude (λ) for the polar angle:

$$B_r = -\frac{2k_o}{r^3} \sin \lambda \quad ; \quad B_\lambda = \frac{k_o}{r^3} \cos \lambda \quad ; \quad B_\phi = 0 \quad (4.2)$$

To model the fundamental modes of particle motion, one also neglects the electric field and solves for the simplified Lorentz equation $dv/dt = (q/(m\gamma))(v \times B)$. An analytic solution to this equation of motion of charged particles in a dipole magnetic field has never been found, and must be solved numerically.

The velocity of a charged particle in a magnetic field may be specified by its speed and its pitch angle, defined as the angle (α) between the instantaneous particle velocity and the magnetic field vector [$\alpha = \text{SIN}^{-1}(v_{\perp} / v)$]. Charged particles with a velocity component perpendicular to the field ($\alpha \neq 0^\circ$) moving in a constant uniform magnetic field will follow a circular trajectory (gyration) about the field line in a plane perpendicular to that field line. Those particles with a velocity component parallel to the magnetic field line ($\alpha \neq 90^\circ$) will trace out a spiral along the field line. In a nonuniform magnetic field where the magnitude varies in the direction of the field and where the field lines converge, charged particles spiraling towards a region of increasing field strength will experience a mirroring force

$$\vec{F}_m = -\mu \frac{\partial B}{\partial s} \vec{b}, \text{ where } \mu = \frac{p^2 \sin^2 \alpha}{2mB}, \text{ which will cause them to decelerate. The point along}$$

the field line at which a particle reaches zero velocity and reverses its direction (i.e., 'mirrors') is referred to as its mirror point. Particles moving along dipole field lines (which converge at both magnetic poles) will bounce back and forth between mirror points in the northern and southern hemispheres, passing through a minimum magnetic intensity at the equator. The 'loss cone' angle (α_{LC}) defines a pitch angle below which a particle's mirror point falls below ~ 100 km altitude, and consequently leads to the electron's absorption by the atmosphere, and 'precipitation' from the magnetosphere. With the assumption that a particle's magnetic moment μ is conserved along its bounce motion [Roederer, 1970], the α_{LC} may be determined by equating a particle's $\mu(\alpha, B)$ at an arbitrary point along a field line with that at its mirror point, taken to be at the top of the atmosphere (~ 100 km). The result (where B_{atm} is B at the top of the atmosphere) is:

$$\alpha_{LC} = \sin^{-1} \sqrt{\frac{B}{B_{atm}}} \quad (4.3)$$

Particles traveling in the dipole-like field of the magnetosphere also experience a force due to the radial gradient in B plus a centrifugal force associated with the curved path it follows along a field line. Combined, these forces result in an overall eastward (westward) azimuthal gradient-curvature drift around the earth for electrons (ions). Radiation belt particles thus exhibit three simultaneous quasi-periodic motions as illustrated in Figure 4.1: (1) gyro-motion about the Earth's magnetic field lines, (2) bounce motion between conjugate northern and southern hemisphere mirror points, and (3) azimuthal drift motion around the Earth.

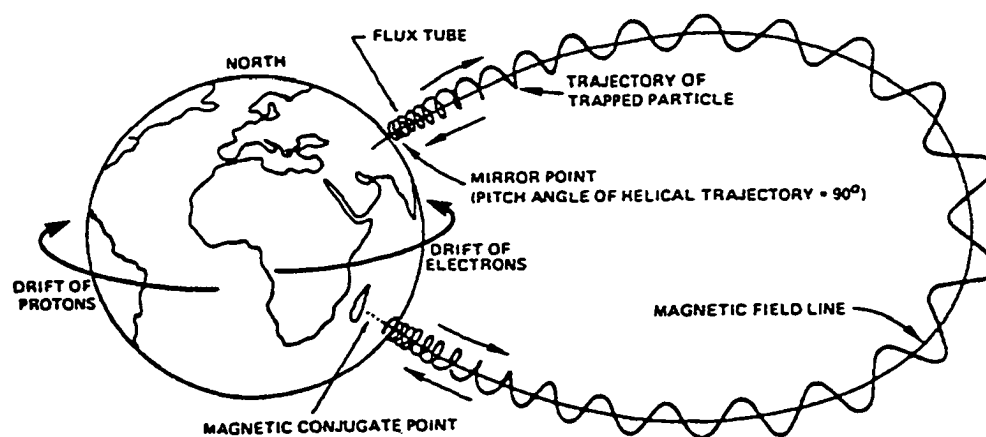


Figure 4.1 : The fundamental periodicities of radiation belt particles [Spjeldvik and Rothwell, 1985].

4.2 Guiding Center Approximation

The next level of simplification beyond the 'test particle' approach is the 'guiding center' approximation. Assuming that the magnetic field does not vary significantly over the space or time scale of a full gyration, there exists a moving frame of reference in which an

observer would see a test particle executing circular motion in the plane perpendicular to the magnetic field. In such a frame, referred to as the guiding center system, the instantaneous center of gyration is the guiding center (R_{gc}) and the radius of the circular gyration is the gyroradius (Larmour radius, R_L). The position of a particle may therefore be defined in terms of its guiding center vector plus its gyroradius vector ($r = R_{gc} + R_L$).

The description of magnetospheric particle motion is greatly simplified within the guiding center system where the gyromotion is averaged out, and one refers to the bounce motion and azimuthal drift motion of the particle's guiding center. In a constant but non-uniform magnetic field, the first order guiding center azimuthal drifts due to the magnetic field gradient (v_{gd}) and magnetic field line curvature (v_{cd}) are given as [Roederer, 1970] :

$$\vec{v}_{gd} = \frac{c p_{\perp}^2}{2 m_o q \gamma B^3} (\vec{B} \times \nabla_{\perp} B) = \frac{\mu c}{q \gamma} \frac{(\vec{B} \times \nabla_{\perp} B)}{B^2} \quad (4.4)$$

$$\vec{v}_{cd} = \frac{c p_{\perp}^2}{m_o q \gamma B^3} (\vec{B} \times \nabla_{\perp} B) \quad (4.5)$$

Figure 4.2 illustrates the radial and energy dependence of the gyrofrequency and the guiding center bounce and drift frequency for an electron ($\alpha_o=45^\circ$) in a dipole field. From the top to bottom panel, the electron gyro, bounce, and drift frequencies are plotted versus L for a given energy (dotted line, 0.3 MeV; dotted-dashed line, 0.8 MeV; and dashed line, 1.6 MeV). The parameter L labels the set of dipole field lines which cross the magnetic equator at a radial distance of $r = LR_E$, where an Earth radius $R_E=6371$ km. These curves are drawn using analytic expressions (approximate for bounce and drift) taken from *Schulz and Lanzerotti* [1974].

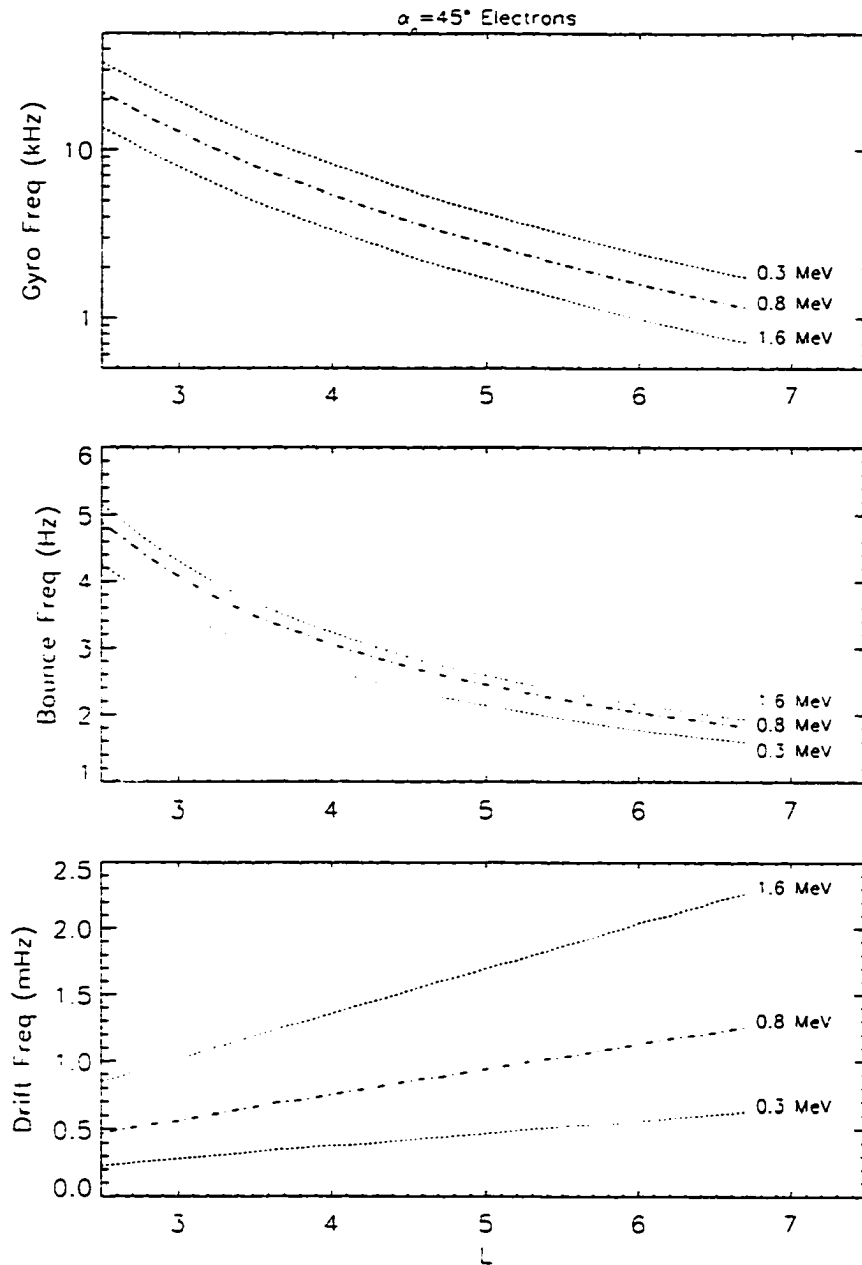


Figure 4.2 : L dependence of gyro, bounce, and drift frequencies for 0.3, 0.8, and 1.6 MeV electrons.

The three fundamental periodic motions may be treated independently since the frequencies for a given particle are separated by roughly three orders of magnitude, with $f_{\text{gyro}} \gg f_{\text{bounce}} \gg f_{\text{drift}}$. For example, a 1.6 MeV electron with an equatorial pitch angle $\alpha_0 = 45^\circ$

which crosses the magnetic equator at a radius of $4 R_E$ will experience a gyro, bounce, and drift frequency of approximately 10 kHz, 4 Hz, and 15 mHz, respectively.

For an existing electric field, there is also a zero order guiding center drift, the **ExB** drift (\bar{v}_{ed}).

$$\bar{v}_{ed} = c \frac{\bar{E} \times \bar{B}}{B^2} \quad (4.6)$$

It is significant that whereas the gradient (curvature) drifts are proportional to the particle's charge and perpendicular (parallel) energy, the **ExB** drift is independent of energy and charge. This difference permits a delineation of particle populations by their different trajectories.

4.3 Equatorial Drifts

The magnetosphere is home to a wide spectrum of particle populations. Relativistic electrons (> 0.1 MeV) coexist with both cold (~ 1 eV) and hot (≤ 100 keV) plasma (ring current) throughout various portions of the magnetosphere. The cold plasma follows the equipotential contours of the magnetosphere's global DC electric field. The hot plasma is also affected by the magnetosphere's electric fields, but because it is also affected by magnetic field gradient and curvature drifts, the hot plasma's drift path is perturbed from the equipotential contours which the cold plasma follows. The relativistic electrons are sufficiently energetic so that the magnetosphere's convection electric field is negligible in affecting their drift paths, and may therefore be ignored for the most part. Unperturbed equatorial particles with zero parallel (to field line) momentum (90° pitch angle) will remain in the equatorial plane where the magnetic field is at a minimum, and will gradient drift along

paths of constant magnetic field intensity contours. Figure 4.3 is an empirical model of equatorial magnetic field contours under quiet magnetic conditions.

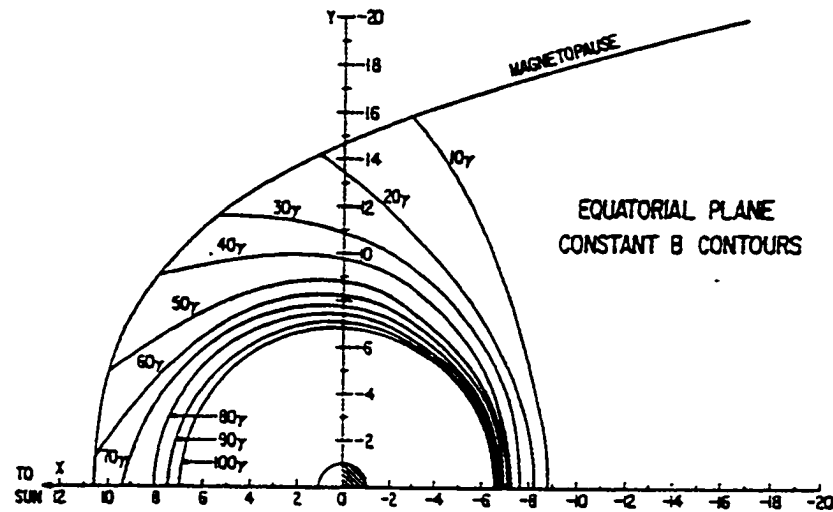


Figure 4.3 : Equatorial magnetic field contours [Fairfield, 1968].

Evident from the figure is the asymmetry in the geomagnetic field, with steeper gradients on the nightside than on the dayside. Evident also, is that contours of less than ~ 65 nT intersect the magnetopause, and do not form closed contours. Only contours $> \sim 65$ nT will support a complete drift orbit; particles drifting on contours outside this are only 'quasi-trapped', and will eventually interact with and be lost through, or scattered by, the magnetopause. Also, because of the steeper gradients on the night side, electrons drift faster there than on the dayside. Consequently, radiation belt electrons spend disproportionately more time on the dayside than the nightside.

4.4 Adiabatic Invariants

There is a well developed description of particle motion in the radiation belts based on the quasi-periodicities and their hierarchy of well separated characteristic frequencies :

$f_{\text{gyro}} \gg f_{\text{bounce}} \gg f_{\text{drift}}$. Within the framework of classical Hamiltonian mechanics theory, each nearly cyclic motion is described by a canonical angular coordinate (the gyro, bounce, and drift phase angle), and its corresponding canonical angular momentum (Hamilton-Jacobi action variable, J_i).

$$J_i \equiv \oint_i \left[\vec{p} + \frac{q}{c} \vec{A} \right] \cdot d\vec{l} \quad (4.7)$$

Here, \vec{p} is the particle momentum, \vec{A} is the electric vector potential, q is the charge, and c is the speed of light, and the closed path integral is about the gyro, bounce, or azimuthal drift path. The contour integral is specified by the near cyclic trajectory of each of the periodic motions. If the magnetic field ($\vec{B} = \nabla \times \vec{A}$) and/or electric field ($\vec{E} = -\partial \vec{A} / \partial t$) varies by only a small amount during the time and/or space interval of the specified periodic orbit of the particle, then the action-angle variable J_i for that specific periodicity is an approximately conserved quantity (adiabatic invariant). Integration along the gyro motion yields the first action angle variable, J_1 .

$$J_1 = \oint_1 p_{\perp} dl + \frac{q}{c} \oint_1 \vec{B} \cdot d\vec{S} = \frac{\pi p_{\perp}^2 c}{B|q|} \quad (4.8)$$

Convention defines the first adiabatic invariant as a quantity proportional to J_1 , in this case

given as the relativistic magnetic moment $\mu = \frac{p_{\perp}^2}{2 m_o B}$. Integration along the bounce motion

yields the second action angle variable J_2 , which also specifies the second adiabatic invariant J .

$$J_2 = \oint_2 p_{\parallel} ds = 2p \int_{s_{m2}}^{s_{m1}} \left[1 - \frac{B(s)}{B_m} \right]^{1/2} ds = J = 2pI \quad (4.9)$$

Integration along the azimuthal drift motion yields the third action angle variable, J_3 :

$$J_3 \approx \frac{q}{c} \oint_3 \vec{A} \cdot d\vec{l} = \frac{q}{c} \Phi \quad (4.10)$$

Convention defines the third adiabatic invariant (to within constants) as Φ , the magnetic flux through the drift orbit, $\Phi = \oint_3 \vec{B} \cdot d\vec{S}$.

Assuming that the forces acting on a particle vary on a space and time scale much larger than the individual cyclic motions, then the three adiabatic invariants associated with the particle are approximately conserved. Exact conservation would demand that there were no spatial or temporal variation in the fields, thus leading to exactly periodic orbits in the sense of perfect closure upon themselves.

4.5 The 'L' Parameter

Figure 4.4 shows an arbitrary point (r, λ) on a magnetic dipole field line. The radial distance at which that field line crosses the equator is r_0 . The dipole moment, given as k_0 , points south. The dipole field line equation is given by:

$$r = r_0 \cos^2 \lambda . \quad (4.11)$$

Introducing the dimensionless parameter $L \equiv r_0 / R_E$, where $R_E = 1$ Earth radius = 6371 km, allows one to write:

$$L = (r / R_E) \cos^2 \lambda . \quad (4.12)$$

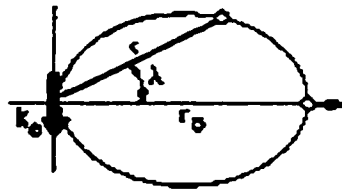


Figure 4.4: Dipole field line coordinates. [Roederer, 1970]

Thus all points along a given field line may be specified by the same L value. A particle undergoing the three period motions in a dipole field, conserving its three adiabatic invariants, will complete an azimuthal drift on the same drift shell - the set of dipole field lines with the same L value. With the dipole magnetic field defined by Equation 4.2, the third invariant in a dipole field is easily found to be $\Phi = -2\pi B_0/r$. In terms of the L parameter, the third invariant for a dipole is given as

$$\Phi = -2\pi k_0 R_E / L . \quad (4.13)$$

Of course, the real geomagnetic field is not a simple dipole, and the task of determining the third invariant for a realistic geomagnetic field is computationally very expensive (particularly decades ago before cheap high speed computers were available!). A more feasible approach was developed by *McIlwain* [1961]. *McIlwain* reasoned that a particle's drift shell could be uniquely specified by the particle's mirror point field B_m , and its bounce integral $I = J/2p$ (from Equation 4.9). Since a particle drift shell was more easily visualized by the parameter L (as in the dipole case) than by the bounce integral I , *McIlwain* developed a functional relation which defined L in terms of I and B_m :

$$L^3 = \frac{k_0}{B_m} F\left(\frac{I^3 B_m}{k_0}\right) \quad (4.14)$$

The function F itself is defined in terms of a dipole field, in that it describes how the relation between I and B_m vary along a dipole field line. However, the function's parameters I and B_m may be determined from a realistic geomagnetic field. The function must be solved for numerically, and one often uses look-up tables to do so. L calculated in this fashion is commonly referred to as the 'McIlwain L parameter' L_M . Computationally, L_M involves only one field line tracing to calculate I and so is very 'cheap' to calculate compared to that of the true magnetic flux invariant.

Although the McIlwain L parameter was originally developed for analyzing the inner zone for $L \leq 3$ where the geomagnetic field is very dipolar, it is almost universally used throughout magnetospheric research for L ranges way beyond that for which it was developed. This is particularly of concern for research in the outer belt where the field lines become very dipolar under active conditions, and L_M ceases to be an invariant. For this reason, *Roederer* [1970] introduced the generalized L parameter, $L^* = -2\pi k_J / (\Phi R_E)$, where Φ is the third invariant calculated with a realistic geomagnetic field. This L^* is used to order the electron data throughout this thesis, and its computation is discussed in Chapter 12.

4.6 Kinetic Theory

The descriptions of particle motion in the preceding sections have all been in terms of individual particles. The theoretical treatment of large collections of particles, where the dynamics of the individual particle are considered, is encompassed within plasma kinetic theory. This treatment describes the evolution of the single-particle phase-space density (distribution) function, $f(\mathbf{r}, \mathbf{v}; t)$ within six-dimensional (\mathbf{r}, \mathbf{v}) phase space. The number of

particles (of a single species) within a 3-D differential volume d^3r centered at position r and traveling within a differential range of velocity d^3v centered about velocity v is given by $f(r, v; t) d^3r d^3v$. Liouville's Theorem states that the particle distribution function remains constant along any dynamical path in phase space [Schulz and Lanzerotti, 1974].

Unfortunately, particle distribution functions are not experimentally determined. Particle detectors typically provide information about the number of particles within a finite energy band (dE), which pass within a finite solid angle ($d\Omega$), through a finite area perpendicular to the particle velocity, and over a finite time interval. This quantity is referred to as the unidirectional differential number flux, $j(E, \alpha)$, and is parameterized by an energy (E) and pitch angle (α) in units of $(\text{cm}^2 \text{ s sr keV})^{-1}$. This quantity may be transformed to phase-space density via the relation $f = j/p^2$

Variations in particle flux are referred to as adiabatic if all three adiabatic invariants are approximately conserved. Large variations in the outer zone electron fluxes are well documented, and it is important to be able to identify and separate out adiabatic versus non-adiabatic effects. Large enhancements may be due to the injection of new populations into a region, and abrupt depletions may be due to enhanced wave-particle interactions which scatter the particles into their loss-cone, thus precipitating them into the atmosphere and permanently removing them from the radiation belts. However, it could also be the case that with a slowly varying magnetic field, a portion of phase space is merely being adiabatically redistributed - that is the particle's energy and pitch angle are gradually being changed from one part of the spectrum to another part in such a prescribed way that their adiabatic invariants are conserved. A study using the SCATHA satellite data [Bass, *et al*, 1989] found

that adiabatic responses of the trapped particle distribution could account for a factor of ten in variation of observed fluxes. A detailed discussion of purely adiabatic variations is the topic of Chapter 13.

When abrupt forces arise due to electric or magnetic fields varying rapidly relative to the canonical periodicities, one or more of the adiabatic invariants may be 'broken' or 'violated' (i.e., no longer conserved) and particles with different canonical phase angles respond differently. In such cases, the random perturbations lead to diffusion with respect to one or more of the adiabatic invariants. This diffusion is discussed in depth in Chapter 7 and the process of radial diffusion is modeled in Chapter 14.

CHAPTER 5

GENERIC MAGNETIC STORM PHENOMENOLOGY

A magnetic storm is characterized by the global magnetic disturbance caused by an enhanced ring current. The Dst index, a measure of the ring current strength (Chapter 9.5), provides the defining signature of a magnetic storm. Although no two magnetic storms are exactly alike, there is a sequence of events which they generally do share as a common denominator. This sequence of events may be generalized into three phases which form the classic signature of a magnetic storm. These are the initial, main, and recovery phase. The phenomenology and the associated physics of these phases follow.

A prerequisite for a magnetic storm is a prolonged period of the enhanced dawn-to-dusk convection electric field E_c , sustained by a negative IMF B_z [Kivelson and Russell, 1995]. This convection electric field drives electrons and ions earthward to $L=2.5-4.0$ via the $E \times B$ drift [Lyons and Williams, 1984]. The relative strength of the corotation electric field to the convection electric field (see Figure 3.2) increases moving to lower L , where the ions (electrons) begin to follow westward (eastward) azimuthal drifts around the Earth to form the ring current. The maximum ring current intensity is found around $L \sim 3.6$, where the dominant contribution to energy density comes from ~ 85 keV protons [Lyons and Williams, 1984]. As the ring current grows, the geomagnetic field earthward of the ring current becomes depressed, and Dst decreases. This period of enhanced convection electric field is referred to as the main phase and may last from ~ 3

hours [*Lyons and Schulz, 1989*] to as long as a day [*Kivelson and Russell, 1995*]. The onset of the main phase is referred to as the storm sudden commencement (SSC).

Magnetic storms are often preceded by the arrival of a solar wind pressure disturbance which enhances the magnetopause currents and compresses the Earth's magnetic field [*Kivelson and Russell, 1995*]. This compression results in a positive perturbation in the Earth's surface field which is seen as a positive rise in the Dst index. Since the solar wind dynamic pressure is independent of IMF Bz, there may often be a time lag between the compressive phase and the onset of the main phase (when IMF Bz turns negative). This period is known as the initial phase, and depending on the time lag between the solar wind pressure disturbance and the southward turning of IMF Bz, it may last from 0 to >25 hours [*Kivelson and Russell, 1995*].

When IMF Bz turns northward, essentially turning off the convection electric field and a dominant source of ring current particles, the ring current begins to decay and the decline in Dst is reversed. This period when the magnetic field is being restored to its pre-storm configuration is the recovery phase, and can last for on the order of a week.

It is important to distinguish between ring current particle injection which occurs during the main phase by definition, and the injection of more energetic radiation belt electrons (> 100 keV) which are not energetically significant to the ring current. The injection of radiation belt electrons into the ring current region may occur at the end of the main phase or during the recovery phase of a storm, as is the case for the storm to be discussed next.

CHAPTER 6

OVERVIEW OF ELECTRON RADIATION BELT RESEARCH

6.0 Introduction

Immediately following the discovery of the radiation belts, scientists began to hypothesize about possible particle sources, losses, and acceleration mechanisms. To appreciate early radiation belt research, it is important to keep in mind that this was space research in its infancy. All knowledge about space acquired up until this point was from ground measurements or from very low altitude rockets. In the minds of many researchers, solar-terrestrial coupling consisted of the occasional solar flare which lead to a short term wave of solar particles buffeting the Earth. This phenomenon lead Chapman and Ferraro to postulate the transient formation of magnetopause boundary currents. The magnetic storm, observed by global depressions of the Earth's magnetic field, was presumed to result from such solar flare driven perturbations. It wasn't until the late 1950's and early 1960's that the picture of a continuously blowing solar wind dynamically coupled to a permanently formed magnetosphere was developed .

6.1 False Starts

Early on, it was realized that the inner and outer radiation zones were very different in terms of their dominant species, spectral features, and stability. This led

some to believe that the primary source and loss mechanisms were also different [Rothwell and McIlwain, 1960]. Cosmic ray albedo neutron decay (CRAND) was shown to be a significant source for the inner zone energetic protons. It was thus suspected for a while that beta decay of neutrons or mesons may be a significant source for the outer zone electrons [Dessler and Karplus, 1960; Hess, 1960]. This hypothesis, however, had a relatively short lifetime since it was shown that the theoretical spectrum from such a source was dramatically different from that observed [Kellogg, 1960; Walt and MacDonald, 1961]. It was also initially speculated that a source for the outer zone electrons could be direct injection of solar wind plasma. This early hypothesis was also dismissed [Dessler and Karplus, 1960; Arnoldy, et al., 1960], and re-examined 37 years later by Li, et al. [1997a] who reached the same conclusion that the phase space density of the solar wind was not sufficient to act as the primary source for the outer zone electrons.

6.2 Early Observations of Magnetic Storm Effects

The tremendous range in flux intensity observed in the outer zone electrons is particularly associated with magnetic storms. Early observations of the response of the outer zone electrons to a magnetic storm [Rothwell and McIlwain, 1960; Arnoldy, et al., 1960] led to the classic magnetic storm signature of a sharp electron flux decrease following the SSC, with a gradual recovery of fluxes to at least, and sometimes well above, pre-storm levels. Arnoldy, et al. [1960] analyzed Explorer VI data throughout the 16 August 1959 magnetic storm, and related the flux variations to the specific storm

phases as defined by the Dst index. They found that the main outer zone peak, centered at a radius of $2.2 \cdot 10^4$ km ($3.45 R_E$), dropped from around 10 pulses/s during the main phase, to 2 pulses/s during early recovery phase, and then climbed to 17 pulses/s during the late recovery phase. Reportedly, the primary population being observed in the outer zone were auroral electrons (~ 10 s keV).

These early observations were made with the simplest radiation detection instruments which did not discriminate between directly penetrating multi MeV electrons, protons, or bremsstrahlung produced in the shielding by low energy (~ 20 keV) electrons. The general consensus was that the outer zone was dominated by electrons of auroral energies and the Geiger counters were primarily responding to bremsstrahlung. This flawed assumption was corrected after thorough calibration tests and analysis of Explorer 12 data revealed that: "the response of lightly shielded (~ 1 g/cm²) detectors is largely due to direct penetration of the primary electrons, and our 1959 assumptions for the tentative interpretation of Pioneer 3 and 4 observations in the outer zone are seen to be invalid." [O'Brien, *et al.*, 1962].

It wasn't until more sophisticated instrumentation was flown that the response of outer zone electrons to magnetic storms was clearly established with unambiguously identified electron spectra. Using Explorer XII data, Freeman [1964] showed that the low energy component (50-100 keV) and high energy component (>1.5 MeV) of the outer zone electron population respond in fundamentally different ways throughout a magnetic storm. During the main phase, the low energy component increases in intensity while the high energy component decreases. During the recovery phase, the reverse

occurs. Freeman reported that the time variations in the flux of the low energy component were correlated with K_p , but those for the high energy component were anti-correlated.

6.3 Adiabatic Variations

The concepts of adiabatic invariants was well established at the time of the radiation belts discovery, and they became a natural foundation for the subsequent theoretical work on radiation belt dynamics. The following section discusses the variations in the outer zone electrons which may be attributed solely to gradual variations in the Earth's magnetic field which allows all three adiabatic invariants to remain conserved.

In their analysis of the 16 August 1959 magnetic storm using Explorer VI data *Arnoldy, et al.* [1960] noted that after the main phase 'dumping' of particles, the following recovery of electron fluxes to beyond pre-storm levels was coincident with the recovery of the storm time depressed magnetic field as indicated by increasing Dst. Although they pointed out the potential significance of this relationship, they did not postulate any explanation for it.

Realizing that the radiation belt electrons are trapped on magnetic field lines which become distorted during magnetic storms, *Dessler and Karplus* [1960] proposed that these distortions in the Earth's magnetic field could be responsible for the observed variations in storm time electron fluxes. However, *Rosen and Farley* [1961] concluded after analyzing Explorer VI data, that the reversible betatron acceleration of electrons

associated with the magnetic storm modulated geomagnetic field could not fully account for the flux variations observed. Some other irreversible process had to be acting as well.

With this in mind, *Dessler and Karplus* [1961] sought to quantify the adiabatic effect of the storm time betatron acceleration on radiation belt particles. They assumed a model storm diamagnetic ring current which acted as a perturbation to the quiet time dipole field, and depressed the magnetic field around $4 R_E$. Assuming the conservation of all three invariants, they determined the variation in the particle energies with the introduction of a storm time ring current. They found that for a 90 nT main phase storm, a particle initially on a drift shell positioned around $4 R_E$ would have its drift shell displaced outward to $4.5 R_E$, so as to conserve the amount of magnetic flux within its drift shell (third invariant). Assuming conservation of its first invariant, it would consequently lose about half its energy as it moved into a region of diminished magnetic field strength, resulting in a decrease in count rate for a detector counting electrons at a fixed energy.

McIlwain [1966] did a more extensive analysis of this adiabatic effect over a long period including several storm periods. He concluded that any non-adiabatic effects are approximately of second order relative to the reversible adiabatic 'betatron' effect, and that in order to study these non-adiabatic effects it was crucial to accurately subtract off the adiabatic effects. However, to do so would require an accurate magnetic field model which is sensitive to the variations in the magnetospheric currents, of which the ring

current is particularly important because of its coincidence with the particle population being observed.

The most recent examination of this adiabatic effect is *Kim and Chan [1997]*. Using the Hilmer-Voigt [*Hilmer and Voigt, 1995*] and the Ding-Toffoletto-Hill [*Ding, et al., 1995*] magnetic field models (both involve realistic external fields driven by Dst), these authors modeled the adiabatic variations at geosynchronous orbit during a storm of a magnitude comparable to the one studied in this thesis ($Dst_{min} \sim -125$ nT). They found that near the end of the main phase ($Dst \sim -100$), the 1 MeV electron flux dropped by a factor of 55 from pre-SSC levels ($Dst \sim -15$ nT). They also concluded that because the observed loss was greater than the theoretical adiabatic loss throughout the main phase that the dominant loss mechanism was non-adiabatic. The authors also noted that this type of analysis of adiabatic flux variations is applicable primarily throughout the main phase of a storm when the quiet time population within geosynchronous is expanding outward to geosynchronous, but should be used cautiously during the recovery phase when newly injected storm time populations are being brought into geosynchronous.

6.4 Non-Adiabatic Processes / Diffusive

When a distribution of radiation belt electrons is perturbed by a force acting on a temporal scale comparable to one of its fundamental periodicities (τ_i) then its evolution may be modeled by a special form of the Fokker-Planck equation as a 'diffusion' in the corresponding adiabatic invariant (J_i). This diffusion equation governs the time evolution of the distribution as the result of a random walk, in small steps of ΔJ_i , through a phase

space defined by the three adiabatic invariants. This form of 'diffusion' provides the fundamental framework for radiation belt physics, and the following chapter is devoted to its historical development and current status.

6.5 Non-Adiabatic Processes / Impulsive

There are many observed variations, both increases and decreases, which happen on time scales too fast to be accommodated within the framework of diffusion theory. The Fokker-Planck diffusion equation is derived for, and is suitable to modeling the effects of, electric and magnetic field disturbances which are small in comparison to the zeroth order magnetospheric fields. In discussing the behavior of an electron within the context of radial diffusion, it is assumed that an electron drifting around the Earth along its drift shell may be displaced inwards or outwards from its initial L by some small ΔL within a drift period due to the random action of localized fluctuating magnetospheric fields. In contrast, for example, there are times when a globally coherent electric field may be impressed across the magnetosphere as the result of a rapid global reconfiguration of the geomagnetic field. In this case, an electron may experience a relatively large displacement within a single drift period. This sudden radial transport, or injection, would not be strictly amenable to the perturbative techniques of radial diffusion theory.

The most widely recognized case of an injection to low L in recent years is that of the March 1991 event when ~ 20 MeV electrons were rapidly injected to $L \sim 2.5$ by the globally coherent induced electric field associated with the dayside compression by

an unusually large solar wind shock [*Mullen and Gussenhoven*, 1991; *Blake, et al.*, 1992; *Li, et al.*, 1993].

In addition to the sudden inner transport described above, there is the well known phenomenon of rapid flux 'dropouts', most frequently observed immediately following a SSC. Such drop-outs may be partially attributed to 'magnetopause shadowing' [*West*, 1979], a phenomenon where electrons on closed drift paths become intercepted by an inwardly displaced magnetopause (to within geosynchronous orbit in extreme cases) during the compression of the dayside magnetopause. A portion of these electrons may scatter through the magnetopause and be lost from the magnetosphere.

6.6 High Speed Solar Wind Streams

The response of the outer zone electron population to high speed solar wind streams which has long been, and remains today, of great interest. It has long been recognized that the high speed solar wind stream structure observed near Earth is correlated with enhancements in the outer zone electrons [*Williams and Smith*, 1965; *Williams*, 1966]. These authors, using data taken near solar minimum, observed a 27-day periodicity in the outer zone electron flux intensities. They also found that the greatest variations in electron flux intensity were associated with the passage of interplanetary magnetic field sector boundaries.

The launch of the first geosynchronous satellite (ATS 1) led to numerous correlative studies between MeV electrons and interplanetary conditions. *Paulikas, et al.* [1968] examined the issue using data from near solar maximum and did not find any

strong correlations. However, *Paulikas and Blake* [1976] re-examined the issue using data near solar minimum and found evidence to support *Williams* [1966] earlier work. The interval near solar maximum, with its stronger magnetic activity, obscured the periodic solar stream structures clearly evident during the magnetically quiet times near solar minimum. *Paulikas and Blake* [1979] performed correlations between daily averages of MeV electron flux and various solar wind parameters, and found the strongest correlation with solar wind speed. The 27-day periodicity in MeV electrons at geosynchronous, particularly approaching solar minimum, is well established [*Baker, et al.*, 1986].

More recent work has been devoted to trying to understand the actual mechanism by which high speed solar wind streams may lead to the enhancements of multi-MeV electrons in the outer zone. *Li, et al.* [1997a] examine the question of whether entry of low energy solar wind electrons (20 keV) into the magnetosphere could explain the increases of ~MeV electrons at geosynchronous correlated with high speed streams. They reasoned that a 20 keV electron, if transported from the solar wind in to geosynchronous orbit while conserving its first invariant, would betatron accelerate to 0.7 MeV. However, the phase space density of 20 keV solar wind electrons was found to be an insufficient source for populating geosynchronous altitude with 0.7 MeV electrons. Thus, they argued, that since the solar wind streams correlated with the geosynchronous MeV electron population, there must be some internal acceleration process which correlates with the streams, and indirectly links the high speed streams to the MeV electron enhancements.

There have been other studies examining the electron response to high speed solar wind streams [Li, *et al.*, 1997a; Hilmer, *et al.*, 1996]. Li, *et al.* [1997a] provide a detailed multi-satellite account of the November 1993 storm. They discuss in a very general way the various standard mechanisms which presumably contribute to the electron dynamics (betatron acceleration, radial diffusion, precipitation, magnetopause leakage). Hilmer, *et al.* [1996] examine 15 events interpreted as high speed solar wind streams impacting the magnetosphere. They analyze plots of solar wind data and electron phase space density derived from GPS and LANL satellite fluxes, and conclude that in nearly all high speed solar wind stream events studied, that enhanced fluxes at L=4.2 (GPS satellite) will follow enhancements observed at geosynchronous (LANL satellite) assuming that there is a positive gradient in phase space density and that there is sustained magnetic activity ($K_p \geq 3$) for 2 to 3 days following the solar wind pressure pulse associated with the stream. The implication here is that associated with the increased magnetic activity are enhanced DC electric fields and/or field fluctuations required to transport the geosynchronous electrons inwards to lower L.

CHAPTER 7

RADIATION BELT DIFFUSION

7.0 Introduction

When radiation belt particles are perturbed by forces acting on temporal (or spatial) scales comparable to at least one of their fundamental periodicities, their evolution may be modeled as a 'diffusion' in the corresponding adiabatic invariant. The theoretical treatment of this 'diffusion' comprises the fundamental framework for understanding radiation belt physics. Research in this field has largely proceeded under the assumption that the dynamics may be viewed as comprised of the two idealized independent modes of radial and pitch angle diffusion. In radial diffusion, the third invariant is violated while the first two are conserved. In pitch angle diffusion, the first and/or second invariant are violated while the third is conserved. This chapter highlights the historical developments which have lead to the current paradigm of radiation belt electron diffusion. The first two sections will cover the conceptual foundations for radial and pitch angle diffusion, respectively. The third section will discuss how these two modes of diffusion are simultaneously modeled. The fourth section compares a number of semi-empirically derived radial diffusion coefficients, some of which will be used in modeling for this thesis. Because of the extensive coverage given here, the final section will summarize the key points.

7.1 Radial Diffusion

The framework for analyzing the three fundamental periodicities of motion for a test particle in a magnetic field in terms of adiabatic invariants was in place by the time of the discovery of the radiation belts [*Rosenbluth and Longmire, 1957*]. However, the question of how a distribution of radiation belt electrons would evolve when subjected to a random perturbation of these invariants had not been studied. The perturbation of the third invariant, or radial diffusion, was the first mode of diffusion to be studied.

In a qualitative discussion, *Gold* [1959] suggested that radiation belt enhancements occur following a solar eruption, during the ensuing magnetic storm, when the solar particles migrate into the outer reaches of the belts ($\sim 5 R_e$) through relatively small scale irregularities in the geomagnetic field which extend out into the interplanetary magnetic field. At this time, it was not yet recognized that the solar wind existed as an omnipresent source of solar plasma interacting and shaping the magnetosphere. Once injected, *Gold* suggested (incorrectly) that the static non-dipolar components of the geomagnetic field would be sufficient to lead to radial diffusion. He also recognized (correctly) that externally driven magnetic variations would lead to greater radial diffusion with increasing altitude. *Gold* emphasized that diffusion would proceed in both radial directions, with outward diffusion leading to a loss through the outer boundary, and inward diffusion leading to absorption by the atmosphere. However, *Gold* made no reference to inward radial diffusion at constant first invariant as a mechanism for energizing the particle population.

Kellogg [1959] avoided the difficult issue of identifying the source at the outer boundary (at $\sim 5-7 R_E$) and focused on the mechanism which could redistribute and accelerate the newly injected population. He proposed that fluctuating electric fields (with zero time average) acting on longitudinally drifting particles would lead to radial diffusion. With the assumption that the particles diffuse at a constant first invariant, he concluded that the particles would realize a net energy gain only if they were drifting in an azimuthally asymmetric, and not a symmetric, magnetic field. It was later shown that the magnetic field need not be asymmetric to result in a net acceleration by inward radial diffusion at constant first invariant [*Falthammer*, 1965]. *Kellogg* reasoned that the rate of radial diffusion would increase with altitude, and therefore, would lead to an inward motion of the flux peak. Although he did not introduce a transport equation to model the time dependence of the flux profiles, he did provide a rough estimate of a diffusion rate. Two sources of electric field suggested were the flute instability (which was never shown to be a feasible source) and electromagnetic variations caused by magnetic storm activity.

The problem of modeling the diffusive transport of the radiation belt particle population involved identifying the proper form of both the transport equation as well as the diffusion coefficients embedded in the equation. The early attempts at modeling the time dependent and steady state solution of the radiation belts [*Parker*, 1960; *Herlofson*, 1960] began with the well known diffusion equation as derived from Fick's Law. Fick's Law states that the number of particles passing through a unit area normal to the direction of flow per unit time (current density, j) is linearly proportional to minus the

gradient of the particle density (ρ). In the most general form, the proportionality (diffusion) coefficient D may be a function of the coordinates. Combined with the continuity equation, Fick's Law leads to the general diffusion equation:

$$\frac{\partial \rho}{\partial t} = -\nabla \cdot \vec{j} = -\nabla \cdot (D \nabla \rho) \quad (7.1)$$

Parker [1960] used the above diffusion equation for the first in-depth analysis of radiation belt particle radial diffusion. Parker recognized that there were a large variety of geomagnetic disturbances which could significantly contribute to radial diffusion. These included localized large amplitude geomagnetic fluctuations, global sudden impulses (not associated with storms), and global storm sudden commencements (SSC). To simplify the analysis, Parker chose to define the diffusion coefficient (D) in terms of a specific form of magnetic storm perturbation [*Chapman and Ferraro*, 1931]. The Chapman-Ferraro SSC model assumes an abrupt (on a time scale short compared to the drift period of the particles of interest) initial phase of a magnetic storm in which a transient solar plasma perturbation (the solar wind had not been postulated at the time) impacts the dayside magnetosphere resulting in an asymmetric compression of the idealized (dipolar) geomagnetic field. This initial compression is followed by a more gradual, azimuthally symmetric, relaxation of the field back to its dipole configuration. The abrupt asymmetric perturbation breaks the third invariant of the particles, with the individually drifting particles radially displaced by varying amounts depending on their longitudinal drift phase. Parker analyzed the effects of a magnetic storm compression on radiation belt particles by assuming an initial distribution of equatorially mirroring particles gradient (∇B) drifting in longitude along a constant B contour at constant

radius in an undisturbed dipole field. The compression is treated as a small asymmetric perturbation which displaces the initial distribution of particles a different radial amount as a function of longitude, on a time scale which is short compared to the drift period of particles of interest. The initially singular (in radius) distribution is therefore spread out into a broader radial band. Since the first invariant is conserved (the second invariant is zero for equatorially mirroring particles), those particles which are displaced to smaller (larger) radius drift paths on contours of greater (lesser) B magnitude gain (lose) energy. Based on this analysis, and an estimate of the frequency of magnetic storms, Parker estimated that a particle initially positioned at a radius of around 3.5 Re would take ~ 5 years to diffuse inwards about 1 Re. To evaluate the time dependence of an initial population of particles responding to a sequence of storm compressions, Parker introduced the following diffusion equation (which is in the form of Equation 7.1 in cylindrical coordinates), where $2\pi r \phi(r, n)$ is the number of particles in dr following a number of storms (n).

$$\frac{\partial \phi}{\partial n} \equiv \frac{1}{r} \frac{\partial}{\partial r} \left(D(r) r \frac{\partial \phi}{\partial r} \right) \quad (7.2)$$

It should be emphasized at this point, that in this analysis (and all others assuming a dipole field), there is a very simple relation between the third invariant and the radial coordinate r because the geomagnetic field is idealized as an azimuthally symmetric dipole field (Chapter 4.5). Perturbing (or 'breaking') a particle's third invariant Φ by an incremental amount $\Delta\Phi$ may be equivalently expressed in terms of a perturbation of the particle's guiding center radius r by an amount Δr . It is because of this relationship that

diffusion with respect to the third invariant can be treated with a diffusion equation and coefficient given in terms of the particle's radius r .

Parker eased the constraint of strictly equatorially mirroring electrons to include those mirroring 'very close' to the equator, enabling him to rewrite the above equation in terms of a volume electron density function $\Psi(r,n)$. He then solved a generalized form of this "time" dependent equation and analyzed the evolution of an initial distribution, showing that the flux peak diminishes in intensity as it travels inwards as a traveling wave. He also solved for the steady state solution and used the results to predict the radial profile of observed count rates. Parker predicted count rates that fell off as $\sim r^{-12}$ to r^{-16} and which were claimed to be in agreement with the large radial variations observed for $r > 4 R_e$.

The study by *Davis and Chang* [1962] was the first to formulate the problem of radial diffusion using the Fokker-Planck equation. The Fokker-Planck equation is of fundamental importance to statistical and plasma kinetic theory [*Ichimaru*, 1973], as well as to radiation belt diffusion theory. It describes the evolution of a one particle phase space distribution function, $f(x,t)$, which varies slowly in time due to large numbers of random perturbations of the phase space coordinates x . The Fokker-Planck equation can be used to describe any general phenomenon that approximates a Markoff process - a process for which temporal variations in $f(x,t)$ depends only upon the instantaneous state of the system described by $f(x,t)$, and not on any of the details of how the system arrived at that state. The Fokker-Planck equation (to second order in Δx) has the following general form:

$$\frac{\partial f}{\partial t} = - \sum_k \frac{\partial}{\partial x^k} (D_k f) + \sum_{k,l} \frac{\partial^2}{\partial x^k \partial x^l} (D_{kl} f) \quad (7.3)$$

where $\mathbf{x} = (x^1, x^2, \dots)$ are the phase space coordinates and $f=f(\mathbf{x},t)$ is the phase space distribution function. D_k and D_{kl} are the Fokker-Planck coefficients defined below as the expectation values per unit time of the mean displacement and mean square displacement, respectively, of the phase space coordinates. $\Psi(\mathbf{x},\Delta\mathbf{x})$ is the probability that the coordinate \mathbf{x} will change by an amount $\Delta\mathbf{x}$ in a time interval Δt .

$$D_k = \frac{1}{\Delta t} \int \dots \int \Delta x^k \Psi(\mathbf{x}, \Delta\mathbf{x}) d\Delta x^1 \dots d\Delta x^n \equiv \langle \Delta x^k \rangle \quad (7.4a)$$

$$D_{kl} = \frac{1}{2\Delta t} \int \dots \int \Delta x^k \Delta x^l \Psi(\mathbf{x}, \Delta\mathbf{x}) d\Delta x^1 \dots d\Delta x^n \equiv \frac{1}{2} \langle \Delta x^k \Delta x^l \rangle \quad (7.4b)$$

Davis and Chang [1962] assumed a Chapman and Ferraro model of a storm sudden commencement [*Chapman and Ferraro*, 1931], as did *Parker* [1960], but broke new ground by using a Fokker-Planck formulation to model the radial diffusion. In analyzing the evolution of an injected particle population, they assumed the conservation of the first and second ($J=0$) adiabatic invariant. The third invariant was broken by the magnetic storm compression which occurred on the time scale of the particle drift period. The form of the Fokker-Planck equation used by these authors was the following:

$$\frac{\partial \phi(r,n)}{\partial n} = - \frac{\partial}{\partial r} [D_1 \phi] + \frac{\partial^2}{\partial r^2} [D_2 \phi] \quad (7.5)$$

where $\varphi(r, n) dr$ is equal to the number of particles (guiding centers) in dr at equatorial radius r following n storms. $D_1 \equiv \langle \Delta r \rangle$ and $D_2 \equiv \langle (\Delta r)^2 \rangle / 2$ are the guiding center's mean radial displacement and mean radial displacement squared per storm. Davis and Chang point out that Parker's expression for $\langle \Delta r \rangle$ needed to be carried out to higher order to obtain the proper non-vanishing Fokker-Planck diffusion coefficient. Because of the non-vanishing D_1 , Davis and Chang's steady state solution differs greatly from Parker's, leading to much higher fluxes at small radii. Davis and Chang realized that this diffusive process would be most significant for particle energies on the order of .1-10 MeV, and that the existing thermal plasma would not be affected.

Modeling radial diffusion in the radiation belts began with a simple diffusion equation with a single diffusion coefficient [Parker, 1960], and was soon followed by a Fokker-Planck equation with the two transport coefficients D_1 and D_2 [Davis and Chang, 1962; Nakada and Mead, 1964]. The determination of the mean displacement $\langle \Delta r \rangle$ is found to be quite intractable for all but the simplest perturbation models, but neglecting it makes considerable difference in the solution to the diffusion equation [Davis and Chang, 1962].

Fortunately, Dungey [1964] and Falthammar [1966] derived a relationship between $\langle \Delta r \rangle$ and $\langle (\Delta r)^2 \rangle$ which allowed the diffusion equation to be written in terms of only the more simply derived $\langle (\Delta r)^2 \rangle$ coefficient. Falthammar [1966] derived the following explicit relationship between the two Fokker Planck coefficients:

$$D_1 = r^2 \frac{\partial}{\partial r} \left(\frac{D_2}{r^2} \right) ; \text{ where } D_1 \equiv \langle \Delta r \rangle \text{ and } D_2 \equiv \langle (\Delta r)^2 \rangle / 2 . \quad (7.6)$$

With this relationship, the two term, one dimensional Fokker-Planck equation for radial diffusion of equatorial mirroring particles in a dipolar magnetic field reduces to:

$$\frac{\partial f}{\partial t} = r^2 \frac{\partial}{\partial r} \left[\frac{D_2}{r^2} \frac{\partial f}{\partial r} \right] \quad (7.7)$$

Up until this point, diffusion coefficients had been derived from the limited type of magnetic disturbance associated with SSCs. Since the time scale between magnetic storms can be months, radial diffusion was envisioned as a process which involved months to years to lead to any significant redistribution and energization of radiation belt particles. *Falthammer* [1965] made the important step of establishing the theoretical form of the diffusion coefficient in terms of the power spectra (non specific) of both electrostatic and electromagnetic field fluctuations.

His analysis begins with the guiding center drift equation for equatorially mirroring particles:

$$\bar{u}_\perp = -\frac{\bar{B}}{eB^2} \times (e\bar{E} - \mu \nabla B) \quad (7.8)$$

where \mathbf{E} is the disturbance electric field and \mathbf{B} is equal to the unperturbed magnetic dipole \mathbf{B}_0 plus the disturbance magnetic field \mathbf{b} . To first order in the disturbance fields (\mathbf{E} and \mathbf{b}), the guiding center equation of motion in the radial direction is:

$$\frac{dr}{dt} = \left(-\frac{E_\varphi(r_o, \varphi, t)}{B_o} + \frac{\Omega_o r_o}{3B_o} \frac{\partial b(r_o, \varphi, t)}{\partial \varphi} \right)_{\varphi = \Omega_o t + \alpha} \quad (7.9)$$

where Ω is the azimuthal (φ) drift frequency, and the quantities subscripted with "o" are evaluated in the unperturbed dipole field. After assuming general series forms for the

perturbation fields, and performing the proper time averaging integrals, and so forth, the coefficients $\langle \Delta r \rangle$ and $\langle (\Delta r)^2 \rangle$ may be found.

For electrostatic perturbations represented by a Fourier expansion in the azimuthal angle φ of E_φ the mean displacement $\langle \Delta r \rangle$ is shown, after an involved derivation, to vanish. The mean square displacement $\langle (\Delta r)^2 \rangle$ after a much simpler derivation, leads to a non-vanishing result. These results are given below [Falthammar, 1965]:

$$\langle \Delta r \rangle = 0 \quad ; \quad \langle (\Delta r)^2 \rangle = \frac{1}{4B_d^2(r)} \sum_{n=1}^N G_n(r, n\Omega(\mu, r)) \quad (7.10a)$$

where,

$$G_n(r, n\Omega(\mu, r)) = 4 \int_0^\infty \tilde{E}_{\varphi n}(r_o, t) \tilde{E}_{\varphi n}(r_o, t + \tau) \cos(\omega\tau) d\tau \quad (7.10b)$$

The coefficient $\langle (\Delta r)^2 \rangle \equiv 2D_{rr}$ is related to the sum over all the harmonics of the spectral power density $G_n(n\Omega)$ of the electrostatic field fluctuations, $\tilde{E}_{\varphi n} \equiv E_{\varphi n} - \langle E_{\varphi n} \rangle$, evaluated at the same harmonic drift frequency of the diffusing particle. For the dipole field in the equatorial plane ($r/R_E=L$), the diffusion coefficient may be expressed as

$$D_{LL}^E = \frac{L^6}{8B_o^2} \sum_{n=1}^N G_n(L, n\Omega(\mu, L)) \quad (7.11)$$

Thus, the only μ (energy) dependence in D_{LL}^E is through the dependence of G_n on the particle's drift frequency which is a function of μ and $L(r)$. This form of D_{LL}^E is quite general in that the form of the spectral power series is not specified. Examples of D_{LL}^E for specific spectra are presented in Chapter 7.4.

Following the same formalism as for the determination of the electrostatic coefficients, *Falthammar* [1965] determined the mean and mean square displacements from the magnetic field perturbations associated with inductive electric field fluctuations. The perturbing magnetic field (\mathbf{b}) was decomposed into an azimuthally symmetric (S) and asymmetric (A) component, and was constructed to be curl free. This extended the previous work on magnetic disturbances which dealt with a very specialized type of disturbance (sudden commencements.) The final result for the mean and mean square displacement is:

$$\langle \Delta r \rangle = 0 \quad ; \quad \langle (\Delta r)^2 \rangle = \frac{1}{4} \left(\frac{5}{7} \right)^2 \frac{r^4 \Omega^2(\mu, r)}{B_d^2(r)} H_1(\Omega(\mu, r)) \quad (7.12a)$$

where,

$$H_1(\Omega(\mu, r)) = 4 \int_0^\infty \tilde{A}(t) \tilde{A}(t + \tau) \cos(\omega\tau) d\tau \quad (7.12b)$$

The coefficient $\langle (\Delta r)^2 \rangle \cong 2D_{r,r}$ is related to the spectral power density $H_1(\Omega)$ of the asymmetric component of the perturbation magnetic field at the particle azimuthal drift frequency. For the dipole field in the equatorial plane ($r/R_E=L$), the radial diffusion coefficient may be expressed as:

$$D_{LL}^M = \frac{1}{8} \left(\frac{5}{7} \right)^2 \frac{L^{10} \Omega^2(\mu, L)}{B_o^2} H_1(\Omega(\mu, L)) \quad (7.13)$$

This form of D_{LL}^M is quite general in that the form of the spectral power function is not specified. *Falthammar* [1966] analyzed D_{LL}^M for two limiting cases of the magnetic fluctuation spectrum H . He found that for a spectrum consisting of magnetic pulses with

a short rise time and very long duration relative to the particle azimuthal drift period (as is the case for the modeled SSCs), that H_1 varies as Ω^{-2} and therefore cancels out all μ (energy) dependence of D_{LL}^M . However, a spectrum with both a short rise time *and* of short duration leads to a coefficient dependent on μ (energy) and with the same L dependence as D_{LL}^E , $D_{LL}^M \sim \mu^2 L^6$. Examples of D_{LL}^M for specific fluctuation spectra are presented in Chapter 7.4.

7.2 Pitch Angle Diffusion

Considerable detail has been paid to the historical development of radial diffusion as a source of radiation belt particles. In any dynamic process where sources are involved, sinks are also necessary to maintain a dynamic equilibrium. It is recognized that Coulomb collisions in the atmosphere pitch angle scatter radiation belt electrons into their loss cone, causing them to precipitate from the magnetosphere [Walt, 1966]. Early work modeling this dynamic balance of sources and losses assumed atmospheric collisions to be the dominant scattering process [Walt and MacDonald, 1961], and this has been shown to be true for $L < 1.25$ [Walt and MacDonald, 1964]. However, an extreme discrepancy existed between observational data which suggested a decay time of ~ 5 days for outer zone electrons [Roberts, 1969] and theoretical estimates of a decay time of thousands of years due solely to atmospheric collisions [Schulz and Lanzerotti, 1974]. This discrepancy lead researchers to propose non-collisional processes, classified as wave-particle interactions (WPI), as the dominant scattering mechanism.

A detailed discussion on the theory of plasma waves is beyond the scope of this work, but the essential elements necessary for a rudimentary understanding of pitch angle diffusion of radiation belt electrons will be presented here. Two fundamental plasma frequencies of importance are the electron plasma frequency and the electron cyclotron frequency. The electron plasma frequency, $\omega_{pe} \equiv (n_e e^2 / m_e \epsilon_0)^{1/2}$, gives the natural frequency of electron plasma oscillations arising from charge-density (n_e) disturbances. The electron cyclotron frequency, $\Omega_{ce} \equiv |eB/m_e c|$, gives the frequency with which a cold plasma electron of mass m_e and charge e gyrates about the ambient magnetic field \mathbf{B} .

The plasma filled magnetosphere sustains many types of waves, from super high frequency (GHz) to ultra low frequency (Hz) electrostatic and electromagnetic waves. Some of the early work presented observational evidence for WPI-induced electron precipitation by electrostatic ion waves in the 0.4-15 kHz frequency range [*Scarf, et al., 1965; Paulikas, et al., 1966; Koons, et al., 1972*]. Others suggested that electromagnetic ion-cyclotron waves produced by ring current protons could lead to significant storm time relativistic electron precipitation [*Thorne and Kennel, 1971; Vampola, 1971*]. However, the main focus of research on radiation belt electron WPI has been on waves commonly referred to as whistlers, and these shall be discussed next.

The following discussion on whistlers and WPI is quite general and is covered in many magnetospheric texts [*Lyons and Williams, 1984; Kivelson and Russell, 1995*]. A whistler wave is an electromagnetic wave which may propagate at an arbitrary angle (θ) to \mathbf{B}_0 at a frequency ω , with $\omega < \Omega_{ce}$. It is a 'right-handed' wave which means that its \mathbf{E}

component rotates about \mathbf{B}_0 in the same sense as an electron (clockwise looking along the direction of \mathbf{B}_0), and is exactly circularly polarized for parallel propagation ($\theta=0^\circ$).

Lyons, et al. [1972] states that although lightning has been identified as a source of whistlers, the wave energy generated naturally within the magnetosphere dominates the wave spectrum. However, the significance that lightning generated whistlers plays in radiation belt dynamics is still unresolved [*Jasna, et al.*, 1990]. Regardless of its origins, whistlers have been observed to be continuously present throughout the plasmasphere at significant levels [*Thorne, et al.*, 1973].

Since both electrons and whistlers are right hand polarized, there is the opportunity for a cyclotron-resonant interaction between them. The resonance condition is given as

$$\omega - k_{\parallel}v_{\parallel} + N\Omega_{ce}/\gamma = 0 \quad (7.14)$$

where k_{\parallel} is the wave propagation vector parallel to \mathbf{B}_0 , v_{\parallel} is the electron parallel velocity, γ is the relativistic correction factor, and N is zero or integer (positive or negative). The wave frequency (ω) and propagation vector number (k) are related through the whistler dispersion relation. For $N=0$, the wave's parallel phase speed equals the electron's parallel speed and the wave interacts with the electron via Landau resonance. When the resonant condition (7.20) is satisfied for $N \neq 0$, the wave and electron are said to interact via cyclotron resonance and N labels the resonant harmonic frequency. For the case where $N < 0$ and $\omega < N\Omega_{ce}/\gamma$ ($\omega < \Omega_{ce}$ is true for whistlers by definition), the wave frequency must be Doppler shifted upward by $k_{\parallel}v_{\parallel}$ to equal $N\Omega_{ce}/\gamma$ in the electron's

reference frame. To do so requires that the wave and electron to be traveling along the magnetic field line in opposite directions ($k_{\parallel}v_{\parallel} < 0$).

When whistler waves and electrons resonantly interact, there is inevitably energy exchanged to some degree. However, *Kennel and Engelmann* [1966] showed that for conditions within the plasmasphere, where the cold plasma densities are high and the whistler wave frequency $\omega \ll \Omega_{ce}$, the whistler's electric field component is negligible compared to its magnetic field component. The simplest case of a parallel propagating whistler with its electric component neglected leaves only a perpendicular magnetic component to perturb the electron. The result is therefore to alter the electron's parallel momentum (scatter its pitch angle) while leaving its energy unchanged.

The relevance of this process for pitch angle scattering MeV electrons into the atmospheric loss cone, thus permanently removing them from the magnetosphere, was first suggested by *Dungey* [1963]. *Dungey* estimated the extent of pitch angle scattering from this proposed resonant interaction, and did so as a function of L. He concluded that whistler interaction with MeV electrons would be significant throughout the interval $2 < L < 4$, and could explain the decay of electrons in this region leading to the 'slot' between the inner and outer belts.

Since WPI is presumed to be a stochastic process in which a random background of wave fluctuations scatter an electron's pitch angle (α) by a small amount during any one resonant interaction, it may be described by a Fokker-Planck equation analogous to that discussed for the radial diffusion process [*Kennel and Petschek*, 1966]. As was the case for radial diffusion, the Fokker-Planck equation defines two coefficients, $\langle \Delta\alpha \rangle$ and

$\langle(\Delta\alpha)^2\rangle$. Kennel and Petschek argue that the original Fokker-Planck equation may be reduced to a simple form with a single diffusion coefficient, $D \equiv \langle(\Delta\alpha)^2\rangle / \Delta t$.

Roberts [1968] derived a crude expression for a pitch angle diffusion coefficient by assuming a purely parallel propagating whistler wave and ignoring its electric component. This leads to a simple form of the Lorentz equation giving the change in the electron's parallel momentum (and hence, pitch angle) in terms of the whistler magnetic component. After performing the appropriate integrations and considerations for a spectral distribution of waves with a peak value of 10^{-10} nT²/Hz at the resonant frequency, Roberts arrived at an 'order of magnitude' estimate of $D=10^{-6}$ sec⁻¹. With the approximation that the decay lifetime of an electron is the reciprocal of D , Roberts estimated a lifetime of about 10 days. As seen in Figure 7.1 [*Roberts*, 1968], this lifetime is in agreement with observations for >0.5 MeV electrons at $L>3$ which were obtained during the early 1960s.

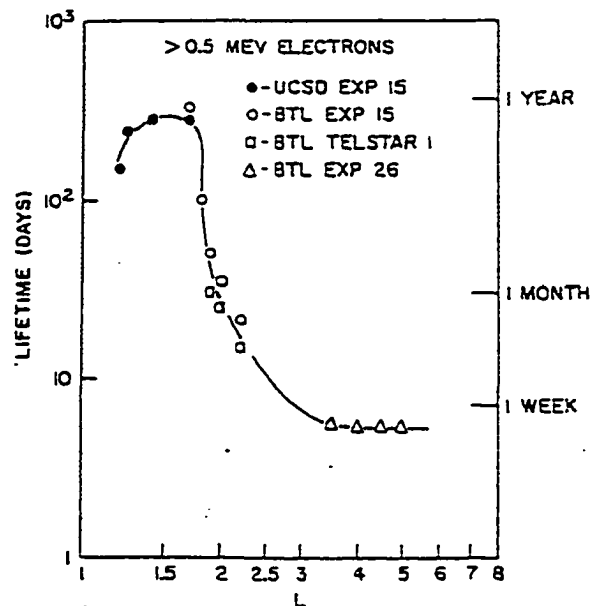


Figure 7.1 : Empirical electron lifetimes [*Roberts*, 1968].

Much of the early theoretical work on whistler-mode resonant interactions with electrons assumed for analytical simplicity that whistlers propagated parallel to the ambient magnetic field [*Kennel and Petcheck*, 1966; *Roberts*, 1968]. This restricted wave-particle interactions to the fundamental ($N = -1$) resonance only. However, whistlers have been observed to propagate within a wide band of wave-normal angles [*Thorne, et al.*, 1973].

Although there had been earlier suggestions that electron scattering by whistler waves could explain the slot formation [*Dungey*, 1963], it had not been rigorously shown how the observed wave power spectra could lead to the observed decay over the wide range of energies for which it is observed. *Lyons, et al.* [1972] found that the intensity of pitch-angle scattering required to explain the rate of electron precipitation in the slot region could be obtained for a wide of energies only if the electrons were allowed to diffuse at the Landau resonance plus all the cyclotron harmonic resonances throughout the electron bounce motion. This resonant diffusion could occur only if the plasmaspheric whistler waves were assumed to propagate obliquely to the ambient magnetic field.

As will be discussed in Chapter 7.3, the problem of modeling simultaneous radial and pitch-angle diffusion is a very difficult task, and a compromise which is usually followed is to reduce the problem of pitch-angle diffusion to a simple exponential loss rate represented by an electron decay lifetime, τ .

Lyons, et al. [1972] determined the lifetimes of electrons as a function of L , and energy (20-2000 keV) assuming both Landau and cyclotron resonances (at all

harmonics) with obliquely propagating whistlers. This procedure first involves determining the total pitch-angle coefficient (D_{xx}) as a function of electron energy and equatorial pitch-angle. In this notation, x is equal to the cosine of the equatorial pitch angle. The coefficient D_{xx} includes the effects of the Landau resonance and all cyclotron harmonic resonances, averaged over the electron's bounce motion. The coefficient D_{xx} satisfies the pitch angle diffusion equation (which assumes a dipole field) given as Equation 7.24 (Chapter 7.3). The electron lifetime τ is defined as:

$$\tau = -\left(\frac{1}{f} \frac{\partial f}{\partial t}\right)^{-1} \quad (7.15)$$

where $f(x,t)$ is the solution to Equation 7.24. To simplify the solution, the assumption is made that the time and pitch-angle dependence of $f(x,t)$ are separable, $f(x,t) = F(t)g(x)$. This assumption is somewhat justified by the work by *Roberts* [1969] who showed that a transient distribution with an arbitrary pitch-angle profile (i.e., following an injection) will rapidly decay to a time independent pitch-angle profile $g(x)$ which will then exponentially decay in magnitude with some characteristic lifetime τ , $F(t) \sim \exp(-t/\tau)$.

An example of these lifetime results is provided in Figure 7.2(a,b) [*Lyons, et al.*, 1972]. The left panel shows the theoretical lifetimes (days) plotted versus L for a range of electron energies from 0.02 to 2.0 MeV. The derivation of these lifetimes assumed a whistler spectrum which peaked at 600 Hz with a width of 300 Hz and a peak amplitude of 35 pT. A cold plasma density radial profile of $n = (1000 \text{ cm}^{-3})(4/L)^4$ was assumed. Shown in the right panel are the theoretical lifetimes (days) plotted versus L for 0.5, 1.0, 1.5, and 2.0 MeV electrons compared with lifetimes inferred from observations following

a large injection event. The lifetime results from *Lyons, et al.*[1972] will be used in this thesis.

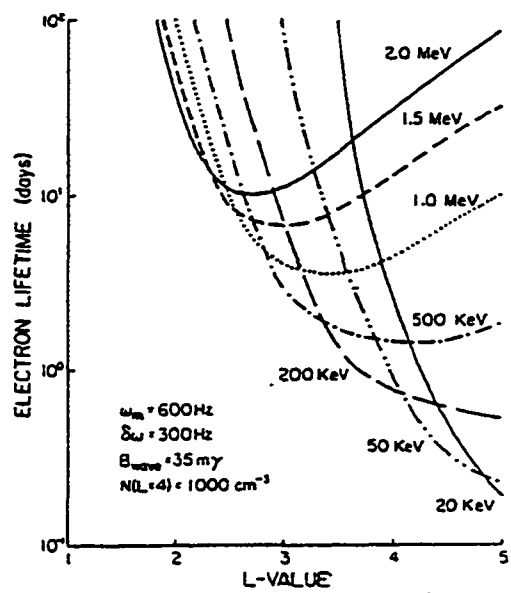


Figure 7.2a : Theoretical electron lifetimes [*Lyons, et al.*, 1972].

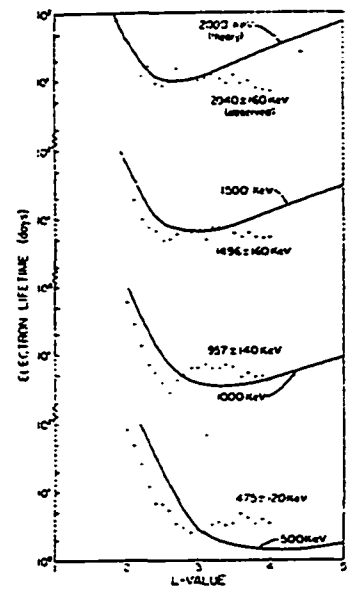


Figure 7.2b : Theoretical and empirical electron lifetimes [*Lyons, et al.*, 1972].

7.3 Multi-modal Diffusion

The simplifying result derived for the one dimensional (radial) Fokker-Planck equation which corresponds to the violation of the third invariant (Equation 7.7), was generalized to n-dimensions by *Haerendel* [1968] to handle the case in which more than one invariant is violated. For instance, one may have the situation of simultaneous pitch angle and radial diffusion where the second and third invariant are violated. For multi-modal diffusion, Haerendel shows that the general form of the diffusion equation for radiation-belt particles is:

$$\frac{\partial f(\bar{X}, t)}{\partial t} = \frac{1}{\mathfrak{I}} \sum_i \sum_j \frac{\partial}{\partial X_i} \left[\mathfrak{I} D_{X_i X_j} \frac{\partial f(\bar{X}, t)}{\partial X_j} \right] \tag{7.16a}$$

where,

$$D_{x_i, x_j} = \frac{\langle \Delta X_i, \Delta X_j \rangle}{2 \Delta t} ; \quad \mathfrak{J} \equiv \left| \frac{\partial(\mu, J, \Phi)}{\partial(X_1, X_2, X_3)} \right| . \quad (7.16b)$$

The distribution function $f(\mathbf{X}, t)$ is the phase-averaged particle distribution function. Equation 7.18 is represented in terms of any general, non-canonical, set of coordinates, \mathbf{X} . The Jacobian, \mathfrak{J} , handles the transformation between the canonical and non-canonical set of variables. If the three coordinates \mathbf{X} are the three adiabatic invariants, then the \mathfrak{J} equals a constant and cancels out of the Fokker-Planck equation.

Solving the full diffusion Equation 7.18 is not only computationally expensive and difficult, but is also unrealizable in a practical sense because of the lack of theoretical understanding of, and experimental evidence for, all of the diffusion processes represented by all the components of the diffusion tensor \mathbf{D} .

"The general problem, with all diffusion mechanisms acting together in an asymmetric field is multi-dimensional, with some of the diffusion mechanisms controlling more than one variable at the same time. It turns out to be impossible to find for this general case an appropriate set of variables each one of which is controlled independently by just one of the interaction mechanisms. ... Simplifications have to be introduced."
[Roederer, 1970, p125]

An assumption which is most often made, leading to significant simplification, is that the process leading to the violation of one adiabatic invariant is uncorrelated with the process responsible for the violation of another. This means that the cross-coefficients $D_{J_i J_j}$, with J_i not equal to J_j , are either zero or negligible. These leads to the simplification of Equation 7.18 to Equation 7.19 below (in terms of the adiabatic invariants) :

$$\frac{\partial f}{\partial t} = \sum_i \frac{\partial}{\partial J_i} \left[D_{J_i, J_i} \frac{\partial f}{\partial J_i} \right] \quad (7.17a)$$

where,

$$D_{J_i, J_i} = \frac{\langle (\Delta J_i)^2 \rangle}{2 \Delta t}, \quad J_i = \mu, J, \Phi. \quad (7.17b)$$

Most theoretical work to this date make the simplifying assumption that the dynamic processes of concern are described in terms of two independent modes of diffusion. One mode is radial diffusion which results from the violation of the third invariant. In this case, the variable J_3 is transformed to the variable L , resulting in the following equation (compares with Equation 7.7):

$$\frac{\partial f}{\partial t} = L^2 \frac{\partial}{\partial L} \left[D_{LL} L^{-2} \frac{\partial f}{\partial L} \right] \quad (7.18)$$

The second independent mode is pitch angle diffusion at constant energy which results when either or both of the first and second adiabatic invariants are violated. In this case, it is most practical to transform the variable J_1 to $x \equiv \cos \alpha_0$, the cosine of the equatorial pitch angle (with $y \equiv \sin \alpha_0$), resulting in the following equation, where T is a bounce averaged integral specific to the dipole field [*Schulz and Lanzerotti, 1974*].

$$\frac{\partial f}{\partial t} = \frac{y^3}{xT(y)} \frac{\partial}{\partial x} \left[\frac{xT(y)}{y^3} D_{xx} \frac{\partial f}{\partial x} \right] \quad (7.19)$$

The above two diffusion equations govern the idealized cases of pure radial (Equation 7.20) and pitch-angle (Equation 7.21) diffusion proceeding independently of one another. A more realistic scenario would involve the superposition of these two

diffusion processes. The equation governing this bimodal process is [Schulz and Lanzerotti, 1974].:

$$\frac{\partial f}{\partial t} = L^2 \frac{\partial}{\partial L} \left[\frac{D_{LL}}{L^2} \frac{\partial f}{\partial L} \right]_{M,J} + \frac{1}{x N_2(x)} \frac{\partial}{\partial x} \left[x N_2(x) D_x \frac{\partial f}{\partial x} \right]_{E,L} \quad (7.20)$$

The form of the diffusion equation most widely used to describe the outer zone electrons is a reduced form of the above. Assuming that the pitch angle diffusion process may be approximated as leading to an exponential decay expressed by a lifetime constant τ (see discussion immediately following Equation 7.17), the above equation may be reduced to the following form:

$$\frac{\partial f}{\partial t} = L^2 \frac{\partial}{\partial L} \left[D_{LL} L^{-2} \frac{\partial f}{\partial L} \right] - \frac{f}{\tau} \quad (7.21)$$

This is the 1-dimensional equation which has been (and still is) widely used in empirically modeling the radial diffusion process and its coefficients D_{LL} - a topic which is addressed in the following section. It will also be used in the analysis for this thesis (Chapter 14).

7.4 Radial Diffusion Coefficients (Semi-empirical)

Chapter 7.1 examined the theoretical form of the radial diffusion coefficient which arise from both potential (D_{LL}^E) and inductive (D_{LL}^M) fields which fluctuate at a frequency in resonance with a particle's drift frequency. The total radial diffusion coefficient is expressed as a sum of these two contributions, $D_{LL} = D_{LL}^E + D_{LL}^M$, where the superscripts refer to the component resulting from the electric (E) and the magnetic (M) fluctuations. The empirically derived coefficients fall into three categories: those derived from magnetic field data (D_{LL}^M), electric field data (D_{LL}^E), and particle data

(D_{LL}^P). Coefficients derived from particle data should include the diffusive effects from both electric and magnetic fluctuations, and thus in principle, $D_{LL}^P = D_{LL}$. The coefficients discussed in this section will be included on a composite plot at the end of the section for comparative purposes.

Historically, the most frequently cited observation in support of radial diffusion of the outer zone electrons is a data set from Explorer 14 involving a single omnidirectional, integral energy channel of >1.6 MeV electrons [Frank, et al., 1964; Frank, 1965]. It is the "systematic movement of the inner edge of the intensity profile from $L \approx 3.8$ to $L \approx 3.3$ " exhibited in Figure 7.3 [Frank, et al., 1964] which has become the 'classic' signature of radial diffusion. Shown are flux profiles (J_0 vs L) for a day

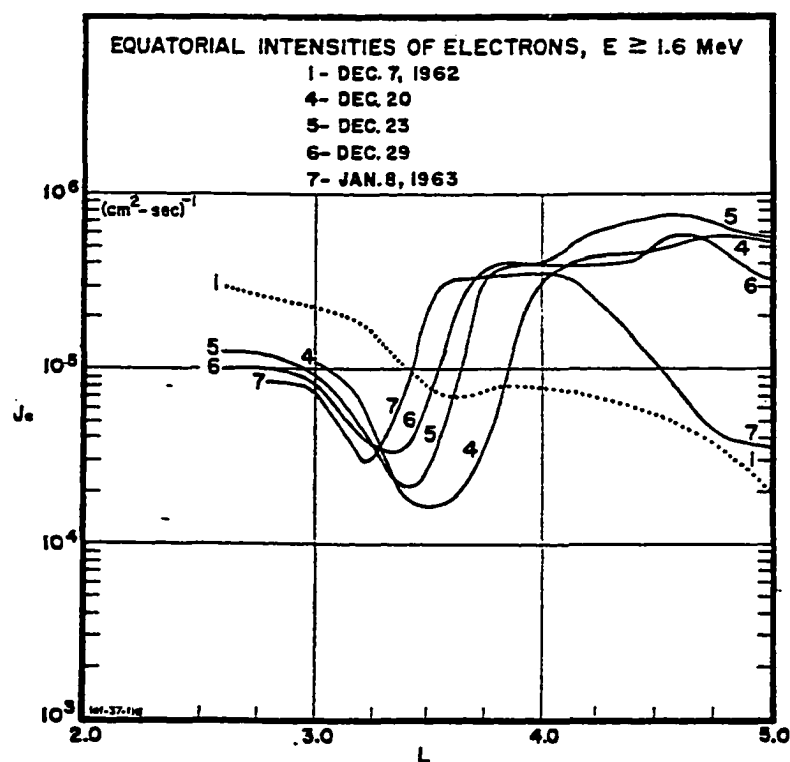


Figure 7.3 : Classic flux profile signature of radial diffusion [Frank, et al., 1964].

preceding the storm enhancements (curve 1, Dec 7) and four days following the storm (curves 4-7) showing the inward motion of the inner edge (with the steep positive gradient). This data set [Frank, 1965] was later used in the first determination of D_{LL}^P discussed later in this section.

After separately discussing the various derivations of D_{LL}^M , D_{LL}^E , and D_{LL}^P , a composite plot of the various determinations of D_{LL} will be made for comparison.

Derivations of D_{LL}^M

Nakada and Mead [1965] used a survey of the frequency and amplitude of storm sudden magnetic commencements (SSC) over a three year period beginning in 1958 to arrive at the following diffusion coefficient expression: $2D_{LL}^M = \langle(\Delta r)^2\rangle = 0.031 R_E^2 (r/b)^{10} R_E^2/\text{day}$, where b is the stand-off distance used in the Mead model. (Care must be taken when comparing diffusion coefficients; *Falthammar* [1966] shows that $\langle(\Delta r)^2\rangle = 2D_{LL}$, where D_{LL} is the more frequently quoted parameter.) *Nakada and Mead* derived this diffusion coefficient independent of particle species, and therefore has relevance to electrons despite the fact that their modeling focused on outer zone protons.

Starting from the general formalism introduced by *Falthammar* [1965] (i.e., Equation 7.15), *Schulz and Eviatar* [1969] developed an expression for D_{LL}^M assuming a Mead field model [*Mead*, 1964] specified by various parameters [magnetic activity dependent: standoff distance (b), series expansion coefficients (B_1, B_2); and constant dipole moment (B_0)]:

$$D_{LL}^M = 2\Omega_3^2 \left(\frac{5B_2}{21B_o B_1} \right)^2 L^{10} \left(\frac{a}{b} \right)^2 \beta_z \left(\frac{\Omega_3}{2\pi} \right) \quad (7.22)$$

β_z is the spectral density of field fluctuations (at drift frequency Ω_3) assumed to be azimuthally symmetric about, and parallel to, the z component of the main field.

Lanzerotti and Morgan [1973] calculated $D_o = L^{-10} D_{LL}^M$ from ground measurements of ULF magnetic field fluctuations near $L \sim 4$ at conjugate points in the two hemispheres. They began with the theoretical form of D_{LL}^M (Equation 7.24) developed by *Schulz and Eviator* [1969], with a quiet time stand-off distance ($b = 10 R_E$). Using a semi-empirical expression relating field fluctuations at $L \sim 4$ on the magnetic equator to those observed at $L \sim 4$ on the ground, they transformed Equation 7.24 to accommodate their measurements. They found that D_o depends on μ (or energy) and L through the relation $(L/\mu)^{(s-2)/2}$, where s is the logarithmic slope of ground based power law fluctuation spectrum. Only in the special case of $s=2$ is D_{LL}^M independent of energy. *Lanzerotti and Morgan* experimentally found that s typically varies between 1 and 3, so that D_o was often independent of energy, or was only slightly directly or inversely related to energy. By analyzing nearly three weeks of data, *Lanzerotti and Morgan* determined D_{LL}^M as a function of magnetic activity (using the daily average K index from a single station, Fredericksburg, $\equiv \langle KFR \rangle$). They determined D_{LL}^M separately for local daytime and nighttime sectors and found the daytime values to be somewhat larger than the nighttime values. By averaging the two, they obtained an azimuthal drift averaged value of D_{LL}^M . Figure 7.4 [*Lanzerotti and Morgan*, 1973] shows this averaged value of $D_o = L^{-10} D_{LL}^M$ for 750 MeV/G electrons plotted against $\langle KFR \rangle$. An estimated 'best fit' line

(not included in their original figure, but performed for this thesis) is superimposed over the data points, and is given as:

$$D_o = 10^{0.75 \langle K_{FR} \rangle - 10.2} \quad (\text{from } L=4) \quad (7.23)$$

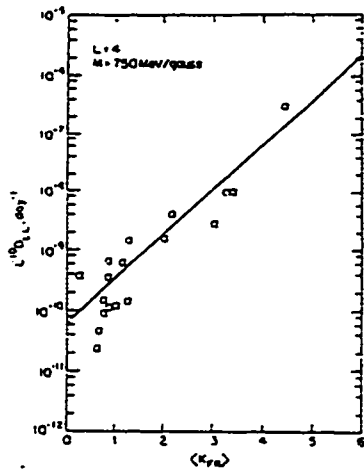


Figure 7.4 : Dependence of D_o^m on K_p ($L=4$) [Lanzerotti and Morgan, 1973].

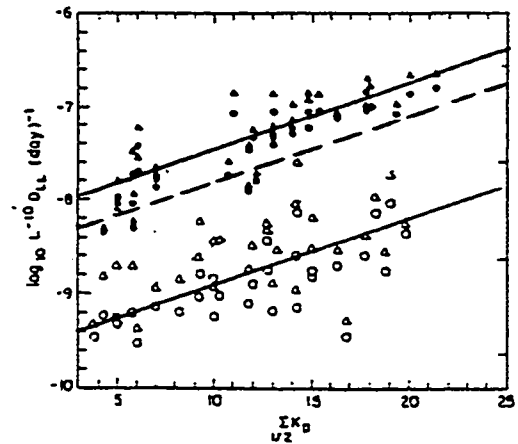


Figure 7.5 : Dependence of D_o^M on K_p ($L=6$). [Lanzerotti, et al., 1978].

Beginning with the same theoretical formalism as Lanzerotti and Morgan [1973], Lanzerotti, et al. [1978] calculated $D_o = L^{-10} D_{LL}^M$ from geosynchronous measurements. They determined D_o from data obtained from both the daytime and nighttime local time sectors as a function of the half-day sum of K_p ($\equiv SK_p$), and found the nighttime sector result ≥ 10 times larger than the daytime result. They seriously considered only the D_o derived from the daytime sector because the magnetic field model used in the derivation does not include the effects of significant substorm activity which inevitably influences the nighttime fluctuation power spectra. In Figure 7.5, both the daytime (unfilled symbols) and nighttime (filled symbols) values of $D_o = L^{-10} D_{LL}^M$ for 115 MeV/G (circles) and 500 MeV/G (triangles) electrons are plotted against SK_p . A least squares fit line for

the D_o determined from the daytime measurements (not included on the original figure, but presented analytically in the text) is given as:

$$D_o = 10^{0.07(\text{Skp})-9.6} \quad (7.24)$$

and is superimposed upon the data points (bottom solid line). It is interesting to note that later work [*Lanzerotti and Wolfe*, 1980] gives more credence to the nighttime determined $D_{LL}^M(L=6.6)$ which are comparable with the $D_{LL}^E(L=6)$ determined by *Holzworth and Mozer* [1979] from data taken on the same day and in the same local time (nighttime sector). Because of the significance later attributed to the nighttime determination of D_o , a 'best fit' line has been estimated for these data as well, and is included in Figure 7.5 (top solid line). For the sake of consistency with *Lanzerotti and Morgan* [1973], an average of the daytime and nighttime 'best fit' line was made and is included in Figure 7.5 (dashed line). The line is parallel to the original referenced line for the daytime derived D_o (Equation 7.24) and is given as

$$D_o = 10^{0.07(\text{Skp})-8.5} \quad (7.25)$$

Derivations of D_{LL}^E

Beginning from the general results of *Falthammar* [1965] (Equation 7.12), *Cornwall* [1968] derived a form of D_{LL}^E specific to substorm convection electric field fluctuation spectra. He assumed a pulse spectrum characterized by rapid rise times and exponential decays (with decay time T) and arrived at the following expression:

$$D_{LL}^E = \frac{1}{4} \left(\frac{cL^3 E_{rms}}{B_o} \right)^2 \left[\frac{T}{1 + (\omega_D T / 2)^2} \right] \quad (7.26a)$$

$$\omega_D = \left(\frac{3\mu c}{eL^2 R_E^2} \right) \left(1 + \frac{2\mu B}{E_o} \right)^{-1/2} \quad (7.26b)$$

where ω_D is the electron drift frequency, E_{rms} is the root mean square of the fluctuating electric field amplitude, B_o is the dipole moment 0.311 G, and E_o is the electron rest energy. This result of Cornwall will be used to determine D_{LL}^E for the diffusion modeling in this thesis.

The study by *Holzworth and Mozer* [1979] is the only work to date which evaluates D_{LL}^E directly from electric field measurements. They determined D_{LL}^E as a function of wave frequency (corresponding to particle resonant drift frequencies, ν) from simultaneous data sets taken at six balloon launch sites spaced in longitude at auroral latitudes (L~6). Since these were measurements of ionospheric electric fields, it was necessary to map the fields back to the equator to determine D_{LL}^E for equatorially mirroring electrons. A major assumption when mapping the fields back to the equator is that there are no significant field aligned potential drops or inductive electric fields. The quiet magnetic conditions throughout this balloon campaign helped mitigate any such problems with the mapping. Following the general formalism of *Falthammar* [1965] (Equation 7.12), the azimuthal components of these mapped fields were Fourier transformed in space and time, with the resulting power spectra used to determine D_{LL}^E . Holzworth and Mozer found for this magnetically quiet time period, at L~6, that:

$$D_{LL}^E(\nu) = 14.0 \nu^{-1.1} \text{ day}^{-1} \quad (7.27)$$

where ν is frequency in cycles/hr.

Derivations of D_{LL}^P

The data set published by *Frank, et al.* [1964] was used in the first semi-empirical derivation of a radial diffusion coefficients for the outer zone electrons [*Newkirk and Walt, 1968*]. *Newkirk and Walt* assumed radial diffusion at constant first and second invariant, and using the one-dimensional Fokker-Planck equation for radial diffusion (Equation 7.23), and a functional form of $D_{LL} = D_0 L^m$, determined the values of the diffusion coefficient D_0 for various values of m . They assumed a lifetime τ of 20 days independent of energy and of radius (for $r > 2.1 R_E$). In order to model the diffusion equation, the omnidirectional, integral energy channel had to be converted into a phase space density f at fixed first and second ($J=0$) invariant. Since $f(L)$ at fixed μ spans an energy range over an L interval, this conversion from a fixed integral energy channel involved significant assumptions about the energy spectra over this range of L . The initial μ dependence of f was specified by choosing an exponential spectrum to fit the data at $L=4$, and then forced the remaining spectra (as a function of L) to fit the distribution required by the conservation of the first two invariants. (This seems like 'fixing' the spectra to fit the theory, but with only one channel there were no other viable alternatives). With this specified initial f , and boundary conditions that f vanish at $L=1$ and $L=8$, and the specified functional form of D_{LL} , the Fokker-Planck equation was integrated by explicit, finite difference algorithms. The parameters for specifying D_{LL} were adjusted to yield the best fit to the data. The resulting form of diffusion coefficient was :

$$D_{LL} = 5 \cdot 10^{-9} L^{10} \text{ day}^{-1} . \quad (7.28)$$

As acknowledged by Newkirk and Walt, this analysis does not necessarily 'prove' radial diffusion, but simply shows that if the data is interpreted within the context of radial diffusion conserving the first two invariants, and all the assumptions made are valid, then the above quoted diffusion coefficients may be deduced from the data.

It is interesting that a later analysis [Lanzerotti, *et al.*, 1970] deduced a radial diffusion coefficient for the same storm period. Contrary to Newkirk and Walt's [NW] admission that their analysis did not constitute a 'proof' of radial diffusion and need not rule out other possible scenarios, Lanzerotti, *et al.* [LMS] state that the results of NW allow one to "positively state that the data indicated a diffusive, rather than a convective, inward movement." The study by LMS was based upon two omnidirectional, integral energy electron channels (>0.5 and >1.9 MeV) from a different satellite than that of NW. This was an advantage over NW's work in that assumptions about the spectral dependence was partially avoided (LMS used both an exponential and a power law fit to their two energy channels). That this is of great significance is highlighted by the observation made in LMS that the >0.5 MeV electron flux showed no evidence of radial diffusion (no inward-moving leading edge) contrary to that of the >1.9 MeV electron flux. This can be seen in Figure 7.6 [Lanzerotti, *et al.*, 1970] where the >0.5 MeV flux channel is plotted in the left and the >1.9 MeV flux channel in the right panel. The five flux profiles shown are for the same days as shown in Figure 7.3. By assuming the specific spectral dependence that they did, NW automatically built into their solution a >0.5 MeV electron population exhibiting the same 'radial diffusive' properties as the >1.6 MeV electrons. LMS emphasize the importance of reconciling the two disparate

temporal profiles of the >0.5 and >1.9 MeV electrons, although this was not attempted in their work. LMS assumed the same functional dependence of the radial diffusion coefficient as NW, but placed no restriction on the radial dependence of the decay constant. For their final result, LMS made the assumption that $D_{LL}=D_0 L^{10}$, and found that D_0 ranged from $1.4 \cdot 10^{-9}$ to $4 \cdot 10^{-9}$ day $^{-1}$ for 300 to 1000 MeV/G electrons, respectively. For 550 MeV/G electrons:

$$D_{LL}^P = 8.0 \cdot 10^{-10} L^{10} \text{ day}^{-1} \quad (7.29)$$

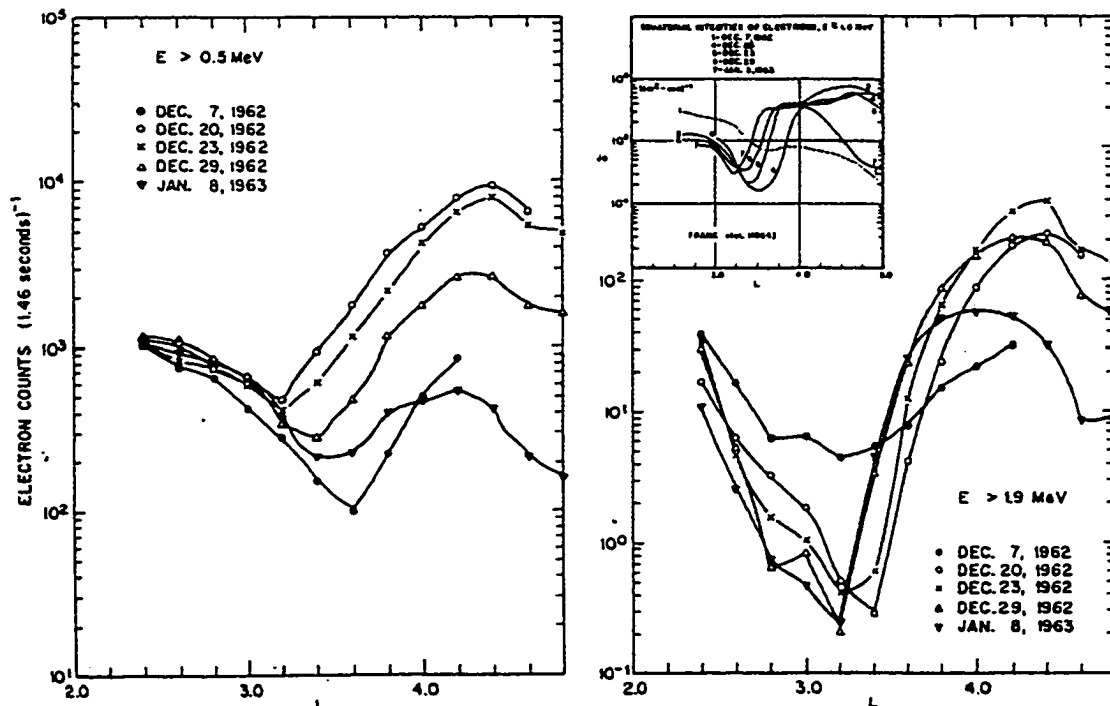


Figure 7.6 : Flux profiles (>0.5 MeV, left; >1.9 MeV, right) used to infer D_{LL} [Lanzerotti, et al., 1970].

The great uncertainties in deducing D_{LL}^P in such studies arise not only from the assumptions made and methods of solutions, but also in the particle measurements themselves. LMS points out the tremendous discrepancy in the measurements made

from the two different (but near equatorial) satellites, measuring essentially the same electrons, for the same time period. Although the data used in both studies (> 1.6 MeV for NW; > 1.9 MeV for LMS) show that the electron fluxes have a minimum at $L \sim 3.4$ and a maximum at $L \sim 4.4$, the data used by LMS show a ratio of $j(L=4.4) / j(L=3.4)$ to be a factor of ~ 100 times greater than that for the data which NW use (see Figure 7.6).

The most recent determination of a radial diffusion coefficient [Selesnick, *et al.*, 1997] was made by analyzing a ~ 3 month period when the magnetosphere was relatively quiet. The standard diffusion equation (Equation 7.23) was used, with the following functional forms of D_{LL} and τ assumed: $D_{LL} = D_0(L/4)^n$; $\tau^{-1} = \tau_0^{-1}(L/4)^m$. The boundary conditions were chosen such that $f=0$ at $L=1$ and $L=8$. The L used was the Roederer generalized L^* , calculated with the Tsyganenko-89 ($Kp=2$) magnetic field model. The time dependent diffusion equation was used to propagate the initial distribution forward in time, and the four parameters used to define D_{LL} and τ were adjusted to provide the best fit to the data. The derived parameters for D_{LL} were $D_0 = 2.1 \cdot 10^{-3} \text{ days}^{-1}$, $n=11.7$; and for τ , $\tau_0^{-1} = 5.0 \cdot 10^{-2} \text{ days}^{-1}$, $m=7.6$. This analysis was performed for a single value of the first invariant ($\mu = 6000 \text{ MeV/G}$) which corresponds to an energy range of 3 to 8 MeV over the L range of 6 to 3, respectively. This is a much higher μ compared to the other μ considered in the comparison of D_{LL} , and since it is not clear how such a result scales with μ , it will not be included in the composite plot.

Comparison of D_{LL}

The following table summarizes the D_{LL} determinations discussed in the preceding section. The first column gives a reference number which corresponds to the reference number in the symbol key of the composite plot D_{LL} (Figure 7.7). The second column gives the reference for the expression given in the third column. The fourth and fifth columns give the L and μ (or energy) range for which the D_{LL} was determined.

Table 7.1: Radial Diffusion Coefficient Summary

Ref #	Reference	Expression	L	μ or Energy
1.M	Nakada and Mead, 1965	$D_{LL}L^{-10} = 0.015 R_s^{-8}$	3-6.6	N/A
*2.M	Lanzerotti and Morgan, 1973	$D_{LL}L^{-10} = 10^{0.75KFR - 10.2}$	4	750 MeV/G
3a.M	Lanzerotti, et al., 1978	$D_{LL}L^{-10} = 10^{(0.07SKP - 9.6)}$	6.6	115; 500 MeV/G
*3b.M	Lanzerotti, et al., 1978	$D_{LL}L^{-10} = 10^{(0.07SKP - 8.5)}$	6.6	115; 500 MeV/G
4.E	Cornwall, 1968	$D_{LL}L^{-6} = (cE/B_0)^2 T / [1 + (\omega_D T/2)^2] / 4$	3-6.6	N/A
5.E	Holzworth and Mozer, 1978	$D_{LL}L^{-6} = 14 v^{-1.1}$	6	.25-1.25 MeV
6.P	Newkirk and Walt, 1968	$D_{LL}L^{-10} = 5 \cdot 10^{-9}$	2-5.5	>1.6 MeV
7.P	Lanzerotti, et al., 1970	$D_{LL}L^{-10} = 8.0 \cdot 10^{-10}$	3.5-4.8	~550 MeV/G
8.P	Selesnick, et al., 1997	$D_{LL}L^{-11.7} = 1.9 \cdot 10^{-10}$	3-6	8000 MeV/G

* Note: References (2.M) and (3b.M) are results which are a revision of the original referenced work. See the text for discussion (preceding section and below).

A few points should be made about the references marked by an asterisk. The expression listed under reference 2.M was inferred from Figure 7.4 (as Equation 7.23) and is not the original authors' analytic result. The expression listed under reference 3b.M (and Equation 7.25) is a revision of the original authors result given in reference 3a.M (and Equation 7.24). When using the results of reference #2 and #3, it is assumed

that K_p is constant throughout the time interval specified in the formula for D_o (daily average for reference #2 and half day sum for reference #3).

Figure 7.7 is a composite plot of all the radial diffusion coefficients discussed in this section. $D_{LL}(L)$ [day^{-1}] is plotted against L on a log-log scale. The figure key associates each reference with a reference number (1-7, as in Table 7.1) followed by a letter (M,E, or P) which indicates whether the coefficient was derived from magnetic field (M), electric field (E), or particle (P) data.

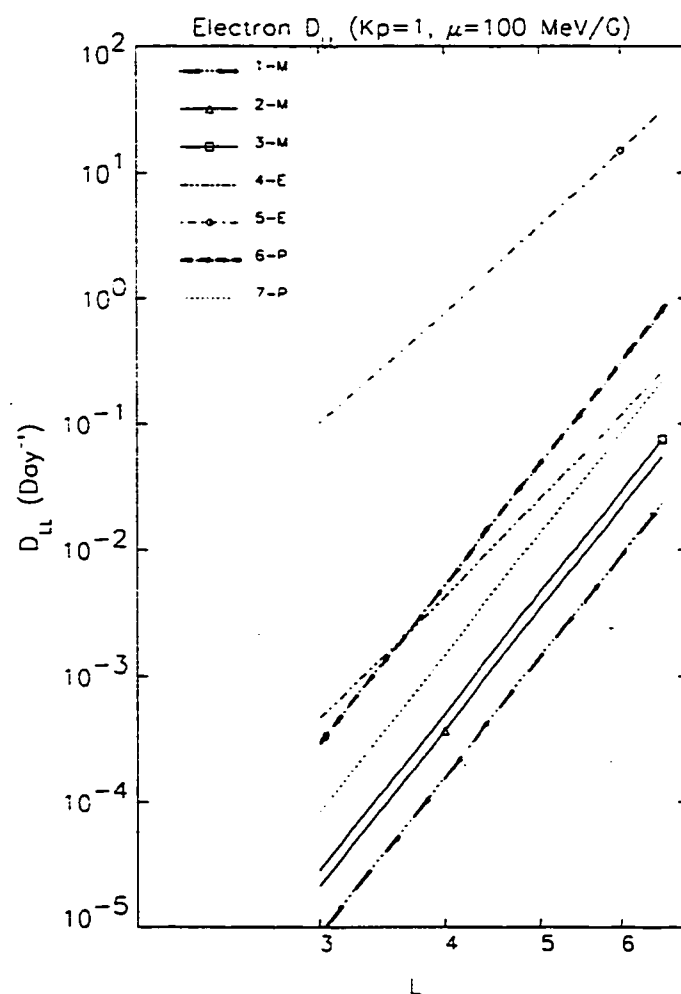


Figure 7.7 : Composite plot of radial diffusion coefficients ($K_p=1$, $\mu=100$ MeV/G).

These results were determined either during an explicitly stated magnetically quiet time (reference 5), during periods of decreasing activity following a storm (references 6,7), over long periods of time including a wide range of activity (reference 1), during variable activity resulting in Kp dependent D_{LL} (references 2,3), or determined with parameters compatible with magnetically quiet times (reference 1: $R_s=10 R_E$; reference 4: $E=0.1$ mV/m). Thus, the $Kp=1$ in the title of Figure 7.7 may be either explicit or implicit (in some averaged sense) depending upon the individual reference. In the same way, the $\mu=100$ MeV/G in the title is loosely used; being explicit in some references, and either approximately true or irrelevant in others.

Although several references (2,3,5) determined $D_o=L^{-n} D_{LL}$ at a single L value (see Table 7.1), the assumed theoretical L^n dependence has been used to extrapolate over the interval $L=3-6.6$ for comparison with other results. The L at which the determination was made is marked on this extrapolated line for reference, with the symbol mark included in the symbol key. The D_{LL}^M and D_{LL}^P are determined assuming an L^{10} dependence. The D_{LL}^E determinations assume an L^6 dependence.

There is obviously considerable spread in the results. Some of the spread is likely the genuine result of the fact that the determinations were made under a variety of magnetic activities and thus reflect a variation in the field fluctuations. However, a good deal of the spread certainly originates from flawed assumptions and techniques, and simply the intrinsic difficulties of dealing with limited data sets.

7.5 Summary of Diffusion Topics

The emphasis of this chapter has been the development of the tools required for modeling radiation belt electron dynamics as a diffusion process. Chapter 7.1 began with the radial diffusion equation describing a diffusion of particles through physical coordinate space (as embodied by Fick's Law and Equation 7.1) and evolved to a modified Fokker Planck equation describing a diffusion in adiabatic invariant space (Equation 7.20). The field fluctuations which drive radial diffusion are those at the electron drift frequency harmonics; and the characterization of these fluctuations are embodied in the radial diffusion coefficient. The radial diffusion coefficient was initially derived from the induced electric field associated with the magnetic compression of storm sudden commencement models. A more general formulation was later developed which enabled the expression of a radial diffusion coefficient in terms of more generalized field fluctuation spectra from both electrostatic disturbances (Equations 7.11), $D_{LL}^E \sim L^6$, as well as electromagnetic disturbances (Equations 7.13), $D_{LL}^M \sim L^{10}$. Chapter 7.4 discusses and tabulates several diffusion coefficients directly inferred from electric and magnetic field fluctuations, as well as indirectly from electron flux measurements. These show orders of magnitude differences, pointing out the difficulty of establishing a single 'standard' D_{LL} .

Chapter 7.2 discusses pitch angle diffusion and its role as the major loss mechanism for radiation belt electrons, particularly in the 'slot' region where plasmaspheric whistler waves are abundant. These whistler waves resonantly interact with electrons and pitch angle scatters them into the atmospheric loss cone leading to

their precipitation from the radiation belts. An effective loss rate (τ) may be derived from the pitch angle diffusion coefficients ($D_{\alpha\alpha}$) which finds agreement with the observed exponential decay of electrons, particularly following a magnetic storm when their fluxes have been greatly enhanced.

The diffusion equation which incorporates both radial and pitch angle diffusion simultaneously is introduced in Chapter 7.3 (Equation 7.20). However, because of the complexities of solving this 'bi-modal' diffusion equation, the pitch angle diffusion term is replaced by a simple pitch angle scattering loss rate (τ), leading to a much simpler equation (Equation 7.21) to solve. It is this equation which has been used extensively throughout outer radiation belt electron diffusion research. By defining D_{LL} and τ , and establishing initial and boundary conditions, both steady state and time dependent solutions may be studied with this equation. Modeling studies which have been performed in the past will be briefly discussed in the following chapter.

CHAPTER 8

DIFFUSION MODELING

In this chapter, modeling efforts which use the diffusion equation introduced in the preceding chapter (in one form or another) will be discussed. The steady state solution represents the electron distribution throughout the radiation belts which is established once all the transient disturbances have died away, and an equilibrium is reached between the sources and losses. Boundary conditions are typically defined with an internal boundary condition set to zero at some minimum L , $f(L_{\min})=0$, and an external boundary condition set to a finite value at some maximum L , $f(L_{\max})$. Thus, the steady state solution f_o , where $(\partial f_o / \partial t) = 0$, represents the dynamic balance between a source as specified by the external boundary condition and any sources and losses within the boundaries.

Lyons and Thorne [1973] (*LT*) and *Lyons and Williams* [1975] (*LW*) used Equation 7.21, reintroduced below, to model observed quiet time 'steady state' electron fluxes (with flux $j = f p^2$, where p =momentum) (*LT*: from Explorer 45 satellite data; *LW*: from OGO satellite data).

$$\frac{\partial f}{\partial t} = L^2 \frac{\partial}{\partial L} \left[D_{LL} L^{-2} \frac{\partial f}{\partial L} \right] - \frac{f}{\tau} \quad (8.1)$$

They used $D_{LL}=D_{LL}^E$ [Cornwall, 1968] given by Equation 7.26 and an electron lifetime τ derived from the combined effects of both pitch angle diffusion [Lyons, *et al.*, 1972] and Coulomb collisions [Wentworth, *et al.*, 1959]. For the energies and L range of interest here, the Coulomb collision term is negligible. Convection electric field (E_c) fluctuation and whistler wave (B_w) amplitudes representative of quiet magnetospheric conditions were used to specify the exact form of D_{LL}^E (LT: $E_c=0.1$ mV/m; LW: $E_c=0.05$ mV/m) and τ (LT, LW: $B_w=10$ pT). They used a constant quiet time electron spectrum (averaged from the data being modeled) as the outer boundary condition fixed at the plasmopause ($L_{max} \sim 5.5$), and set f to zero at $L_{min}=1$ as the inner boundary condition. Solving Equation 8.1 for $\partial f/\partial t = 0$, they quite successfully reproduced the observed quiet time flux profiles for a range of energies (LT: 0.2 - 4.0 MeV; LW: 35-240 keV).

Equation 8.1 may also be used to model the evolution of an initial electron distribution $f(L, t_0)$, which of course would approach a steady state solution such as discussed above at a rate dictated by the specified diffusion and loss rates. As discussed in Chapters 5 and 6.2, electron behavior throughout a magnetic storm is strongly energy dependent. Low energy (<100 keV) electrons (and to a greater degree, ions) contribute to the ring current build up, and so by definition their fluxes will be found increasing during the storm main phase. Lyons and Schulz [1989] seek to explain the contribution of >40 keV electrons (and ions) to the main phase ring current build up by showing that particles greater than ~40 keV may be 'injected' to $L < 4$ by 'enhanced' radial diffusion driven by the electric field fluctuations (D_{LL}^E) associated with the increased substorm activity. They solve the pure radial diffusion equation (Equation 8.1, neglecting the loss

term) with $D_{LL}=D_{LL}^E$ given by Equation 7.26 [Cornwall, 1968]. They assume a pre-SSC initial distribution $f(L, t_0)$ which they evolve in time and compare to a final storm-time distribution. Assuming a value of $E_{rms}=1.37$ mV/m for use in D_{LL}^E , they claim that enhanced (E_{rms} is enhanced over the quiet time value of ~ 0.1 mV/m) radial diffusion can explain the observed main phase injections of two observed storms.

It is interesting to note, however, that the final distributions used for comparison are from the peak of one storm (just before the recovery phase begins) and 6 hours into the recovery phase of the other storm [Lyons and Williams, 1980]. Suitable distributions were not available during the main phase itself for this study on main phase injections. These storms are discussed in more detail in an earlier paper [Lyons and Williams, 1975] which indicates that the 'injections' were initiated near the beginning of the main phase of one storm, but at the very end of the main phase in the second. In both storms, the 'injection' reached peak fluxes well into the recovery phase, even in the >35 keV range, which leads one to question these 'injections' as being a source for the main phase ring current. However, the important point here is that 'enhanced' radial diffusion coefficients can bring large numbers of electrons into low L in a short time period relative to magnetic storm time scales.

More recently, Beutier and Boscher [1995] and Bourdarie, et al. [1996] developed the computer code *Salammbó* for solving a multi-modal diffusion equation which includes diffusion in all three invariants plus some of the cross-coupling modes. Beutier and Boscher [1995] use the NASA static electron models [Vette, 1991] as an outer boundary condition to run their model, demonstrating their code's capabilities and

making some comparisons with the gross features seen in various CRRES electron data. *Bourdarie, et al.* [1996] use the same *Salammbô* code to model the evolution of CRRES measured fluxes following a small storm. They model the storm injection using a LANL geosynchronous average spectrum from the storm period as the external boundary condition ($L=7$) for the first hour of the storm. It is then turned off, and the simulation allowed to run for ~5 days. The diffusion coefficients and plasmapause location are constant throughout. They have moderate success at modeling the decay of 193 keV electrons and the gradual rise of 1 MeV electrons throughout the recovery phase.

CHAPTER 9

DATABASES

9.0 Introduction

The Combined Release and Radiation Effects Satellite (CRRES) was a joint USAF and NASA effort. The 'Release' component (NASA) involved several low altitude releases of chemicals to facilitate the study of diamagnetic cavity formations. The 'Radiation' component (USAF) represents the most thorough effort to date to map the radiation belt environment. It did so with the express purpose of correlating the radiation environment with the performance of a wide range of microelectronic devices.

CRRES was launched on 20 July 1990, a year following the solar maximum peak of Solar Cycle 22. Its data stream was telemetered back to Earth for approximately 14 months before succumbing to a premature failure on 10 October 1991. CRRES traveled in an elliptical geosynchronous transfer orbit inclined at 18° to the ecliptic plane and with a perigee of 350 km. Its apogee of 33,500 km (radius=6.26 Earth radii) precessed westward at $\sim 0.5^\circ$ per day from its initial position at 7 hr LT to its final position at 16 hr MLT. Its orbital period of 9.4 hours enabled it to pass through the inner and outer radiation belts about five times per day. CRRES was spin-stabilized, with its spin axis pointing within 15° of the sun, and spun at two revolutions per minute which provided the most complete pitch angle distribution when the satellite was closest to the magnetic

equator. Data files with complete ephemeris information, including universal time (UT) and satellite position in Earth centered inertial coordinates (see Appendix A for description of ECI coordinates) are provided for each orbit.

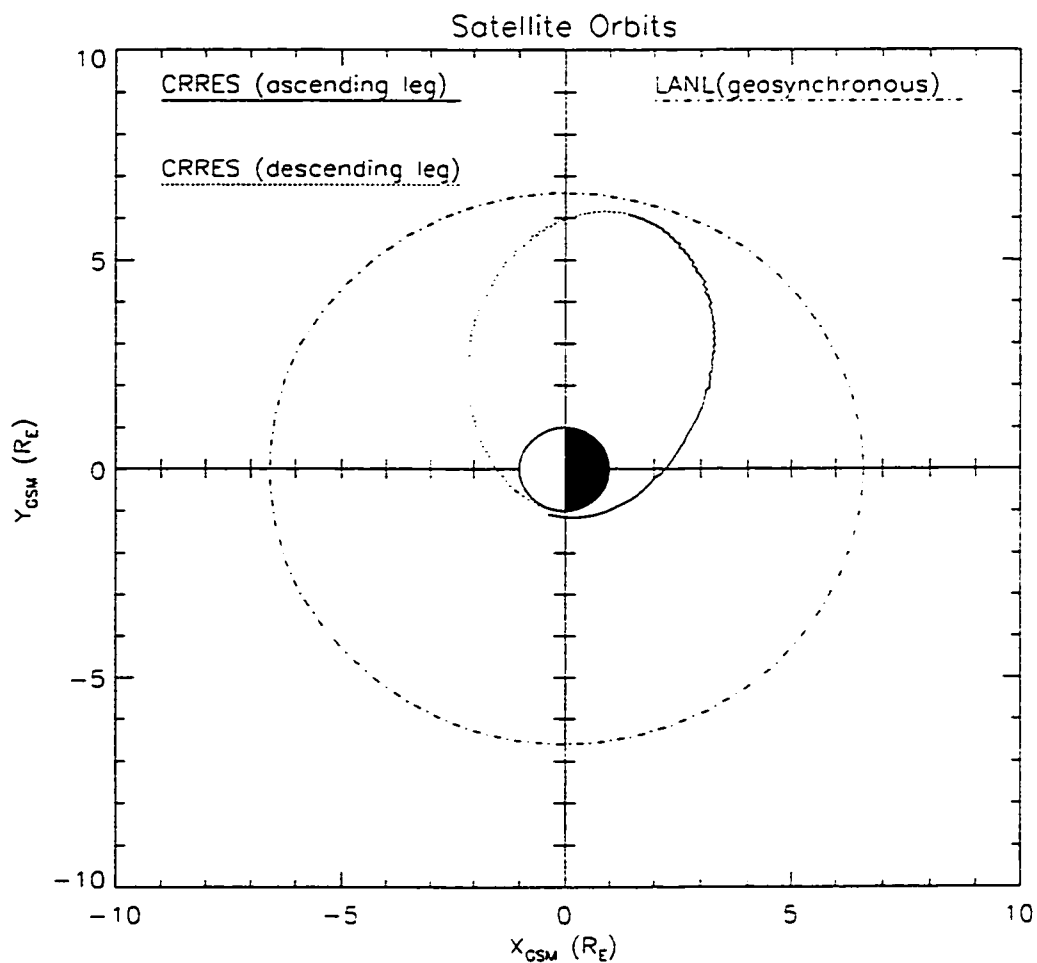


Figure 9.1 : CRRES geosynchronous transfer orbit and LANL satellite geosynchronous orbit.

Throughout the storm to be analyzed for this thesis (8-17 October 1990), CRRES apogee was at ~ 5 hr LT. Figure 9.1 is a scaled drawing of the CRRES orbit during this period. The axes tick marks are in $5 R_E$ increments. An approximate

magnetopause boundary is sketched in with a standoff distance $R_s = 10 R_E$. The CRRES orbit is shown as a separate ascending leg (bold solid line) and descending leg (bold dashed line). The bold circle with a radius of $6.6 R_E$ depicts the orbit of the Los Alamos National Laboratory (LANL) geosynchronous satellite 1989_046 which will be discussed in Chapter 9.6.

The majority of the databases used in this thesis were provided by CRRES (relativistic electrons, electric field, magnetic field, plasma wave, and plasma density). The geosynchronous electrons were provided by LANL satellite 1989_046. The instruments providing these measurements are briefly discussed below. In addition, the solar wind and magnetospheric parameters are also briefly discussed.

9.1 CRRES Electron Magnetic Spectrometer

The Medium Energy Analyzer (MEA) was designed and built by Aerospace Corporation for the USAF [Vampola, *et al.*, 1992]. The MEA is a magnetic spectrometer which separates particle species and energies through momentum analysis. After passing through a collimated aperture (with a nominal view angle of $5-6^\circ$), particles encounter a uniform magnetic field (850 G) which causes ions and electrons to follow near circular paths in an opposite sense. The electrons travel approximately 180° along their circular path, with the higher energies following a smaller radius of curvature. The electrons are thus magnetically focused onto the plane of a linear array of 18 ion-implanted silicon plates. Each of these individual plates are electronically configured with a charged-sensitive amplifier with its lower and upper threshold set for the energy

deposit expected from the radius of curvature. There are seventeen logarithmically spaced energy channels between 0.15 and 1.58 MeV, plus a background channel which responds to very energetic protons (confined to the inner zone) and > 6 MeV electrons which penetrate the MEA housing. A complete energy spectrum is read out every 0.512 seconds, and with a CRRES spin rate of 2 rpms, a full pitch angle distribution ($0-180^\circ$) is accumulated every ~ 15 s. The MEA has large geometric-energy factors (from 2 to 6 $\text{cm}^2 \text{ s sr keV}$) which were calculated from calibration data and provide excellent counting statistics.

During intense fluxes, the two lowest energy channels (0.15 and 0.21 MeV) are often saturated and therefore are excluded from the study to avoid the uncertainties and complexities of their correction. There are also times (and regions) when the highest energy channel fluxes are quite low; these are excluded when their count rates become less than a factor of two higher than the background channel count rates. This was found to be the case near the slot region before the storm.

9.2 CRRES Fluxgate Magnetometer

The magnetic field measurements on board CRRES were made by a triaxial fluxgate magnetometer [*Singer, et al., 1992*] built by Schonstedt Instrument Company. The three sensors are displaced by about 7.5 m from the center of the satellite by a boom to minimize the effect of any residual spacecraft fields. The magnetometer is operated in both a low and high gain mode, with a dynamic range of ± 45000 nT and ± 850 nT, respectively (where $\text{nT}=10^{-9}$ Tesla). The resolution in high gain is 22.0 nT, and in low

gain is 0.4 nT. The sensor signals are sampled at 16 times/s. The database used for this study provided the 3 components of the field at a resolution of 30 s.

9.3 CRRES Electric Field / Langmuir Probe Instrument

The CRRES electric field / Langmuir probe instrument was built by a group at the University of California (Berkeley), Boston University, and the USAF Phillips Lab [Wygant, *et al.*, 1992]. The instrument consists of a pair of orthogonal spherical probe sensors and a pair of cylindrical antennas, each with a tip-to-tip separation of about 100 m. The instrument may be operated in one of two modes. In one mode, the spherical sensors are voltage biased and can be used to determine plasma densities. This thesis will use data from only the electric field mode, in which the sensors are current-biased and measure two electric field components from the potential difference between the opposing sensors of the two pairs of orthogonal booms. These sensors measure the quasi-static electric field in the spin plane of the spacecraft at a rate of 32 samples/s, with a sensitivity of better than 0.1 mV/m.

During the first part of the CRRES mission (before January 1991), there were problems with floating voltages and improper biasing of the instrument. Before using any of this data, the principal investigator (John Wygant) was consulted to ensure proper 'quality control'.

9.4 CRRES Plasma Wave Experiment

The CRRES plasma wave experiment was designed and built at the University of Iowa to measure both electromagnetic and electrostatic plasma waves [Anderson, *et al.*, 1992]. The system includes an electric dipole wire antenna and a search coil magnetometer. The multichannel spectrum analyzer (MCSA) provides magnetic field frequency spectra over the range of 5.6 Hz to 10 kHz in 14 logarithmically spaced frequency channels. The sweep frequency receiver (SFR) provides electric field frequency spectra over the range of .1 to 400 kHz in 128 logarithmically spaced frequency channels.

9.5 Solar Wind / Magnetospheric Activity Indices

Several different parameters are used to characterize the state of the magnetosphere throughout the progression of the magnetic storm. The hourly values of the solar wind speed (V_{sw}) and density (n_{sw}), and the interplanetary magnetic field (z-component and total magnitude) were electronically obtained from the National Space Science Data Center (NSSDC) OMNI database : <http://nssdc.gsfc.nasa.gov/omniweb>.

The magnetic activity indices Kp and Dst were also obtained from the OMNI database. Kp is a 3-hour averaged index derived from a series of magnetometer stations between 46° and 63° latitude. It is a measure of the relative variability of each of the geomagnetic components on a quasi-logarithmic scale varying from 0 to 9 (extremely quiet to extremely active).

Dst is an hourly index determined from the horizontal component (H) of the geomagnetic field measured at a number of low latitude ground stations. H is the projection of the axial field onto the plane tangent to the Earth at the magnetometer station. At each station, a reference H from a magnetically 'quiet' period is determined which is subtracted from every hourly H to give a relative perturbation in H. Dst is the instantaneous average of this set of residuals from around the world, and is a measure of the perturbation from the equatorial ring current [*Kivelson and Russell, 1995*].

The auroral equatorward midnight boundary index [*Gussenhoven, et al., 1983*] can be obtained electronically from: http://www.plh.af.mil/gps/dmspssj4_midnit.html. The auroral boundary index is the geomagnetic latitude, normalized in local time to midnight, of the equatorward boundary of the auroral oval. The boundary is chosen as the magnetic latitude at which the total integrated number flux of 30 eV to 30 keV precipitating electrons drops below a chosen threshold value. This number flux is provided by particle sensors from the Defense Meteorological Satellite Program (DMSP) which typically has a number of satellites in polar orbit at any one time.

9.6 Los Alamos Geosynchronous Electrons

The Los Alamos National Laboratory (LANL) geosynchronous satellite 1989_046 electron data was provided by the LANL website (<http://leadbelly.lanl.gov>) maintained by Geoffrey Reeves. The Synchronous Orbit Particle Analyzer (SOPA) is the instrument on board the LANL satellite which measures the integral electron flux using energy loss (dE/dx) techniques. The instrument consists of three telescopes which are

oriented at 30° , 60° , and 90° to the spacecraft spin axis. The data collection cycle is 10 s which is approximately one spin period of the satellite. The post-flight data analysis involves the subtraction of integral energy channels to determine the differential energy channel spectrum. The principle investigator of the SOPA instrument is Richard D. Belian.

CHAPTER 10

SURVEY OF MAGNETIC STORM

10.0 Introduction

This chapter surveys the magnetic storm initiated on 9 October 1990 with a sudden storm commencement (SSC). This storm was chosen for study for a number of reasons. One primary reason is that it is a well isolated storm, and one need not be concerned with unraveling the effects of multiple disturbances superimposed upon one another as is the case during the second half of the CRRES mission. A second reason is that CRRES was well positioned to witness the injection of electrons into the geosynchronous region, followed by the sudden transport into the slot region. A third reason, is the availability (though incomplete) of interplanetary parameters leading up to and including the storm main phase. The detailed study of such a well defined event such as this one, with data from the suite of instruments provided by CRRES and LANL, provides a unique and valuable opportunity to explore the storm dynamics of the relativistic electrons.

10.1 Interplanetary and Magnetospheric Parameters versus Electron Fluxes

It is the interplanetary conditions (solar wind and interplanetary magnetic field parameters) which modulate the energy flow into the magnetosphere, and thus they are

crucial to understanding magnetospheric storm dynamics. Figure 10.1 surveys key interplanetary parameters, and Figure 10.2 surveys parameters and CRRES electron fluxes which reflects the magnetosphere's response. Figure 10.3 is a survey of the LANL geosynchronous (radius = $6.6 R_E$) electron data which provide the response of the outer edge of the radiation belt (near magnetic equator). The general format of these figures will first be discussed, followed by their interpretation.

Figure 10.1 surveys the interplanetary parameters for approximately one and a half days preceding, and one day following, the SSC on 13:15 UT, day 282 (9 October) 1990. Plotted, from the top panel down, are the interplanetary magnetic field (IMF) magnitude (B) and z component (B_z), the solar wind speed (V_{sw}) and density (n_{sw}), and the standoff distance (R_s) which is derived from n_{sw} and V_{sw} (Equation 3.1). The x-axis scale is in day of the year 1990 and spans two and a half days. Unfortunately, according to the magnetospheric scientist's version of *Murphy's Law*, there are inevitable data gaps in the solar wind data at the most critical moments. However, despite *Murphy*, enough data remains to allow a reasonable assessment of the interplanetary conditions which lead to the global magnetospheric disturbance studied here.

Discussed in conjunction with these interplanetary parameters (cause), are the magnetospheric parameters (effect) plotted in Figure 10.2. The top three panels are the auroral equatorward boundary (Λ_{eq}) and the magnetic activity parameters K_p and D_{st} (see Section 6.5 for a description of these parameters). The bottom two panels are the CRRES electron differential flux (at 0.42, 0.78, 1.09, and 1.37 MeV; for fixed invariant J) at $L^* = 5.2$ and 3.6. The x-axis scale is in day of year for the top three panels, and is

in orbit number for the bottom two panels. There are two flux points per orbit, one each from the ascending and descending leg of the orbit. Obviously, the flux data at $L^*=5.2$ and $L^*=3.6$ were measured at different times during the orbit and thus, the average time of these orbital points provides only an approximate alignment with the time scale of the top three panels of the figure. The time span is approximately 10 days (25 orbits) as opposed to the 2.5 days in Figure 10.1.

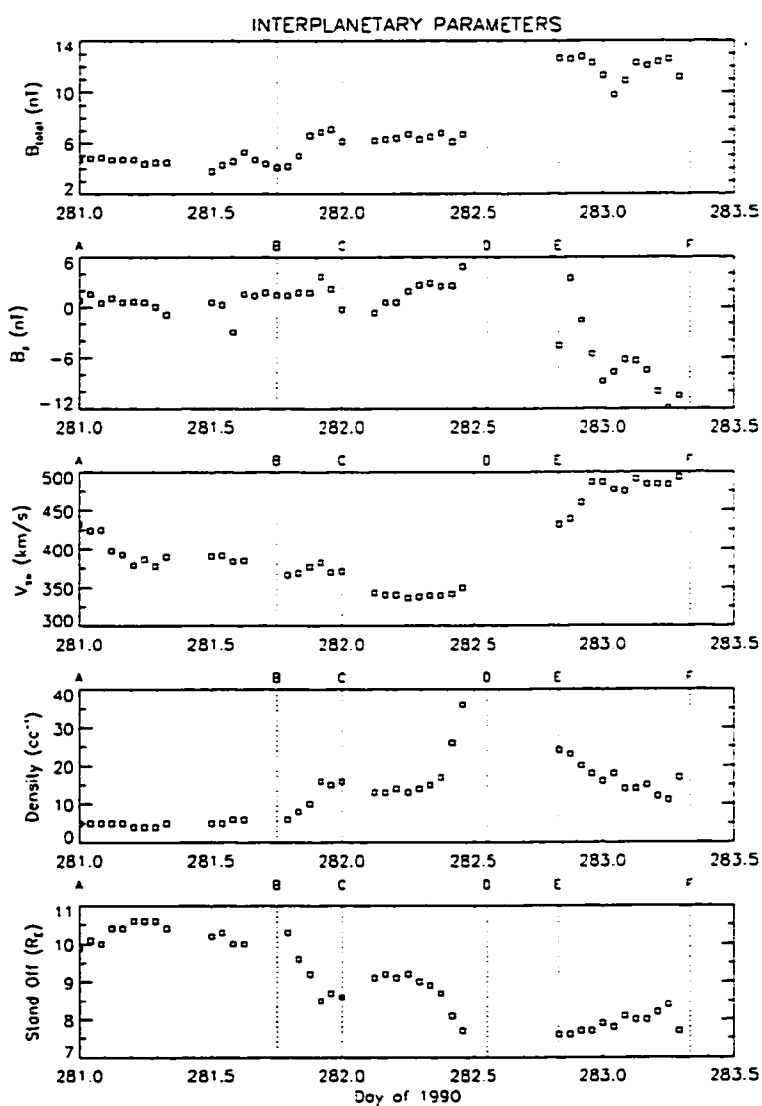


Figure 10.1 : Survey of interplanetary parameters.

Figure 10.3 is a survey of LANL geosynchronous electron data. The top four panels plot differential flux for 0.22-0.31, 0.31-0.50, 0.50-0.75, and 0.75-1.10 MeV electrons; the bottom panel is D_{st} . The time scale (x-axis) is in day of year.

The storm, characterized from start to finish by Figures 10.2 and 10.3, is divided into several time intervals, delineated by vertical dotted lines labeled with letters A-K (placed along the top of the middle panel in Figure 10.2 and above the bottom panel in Figure 10.3), in order to aid the visual correlation between the various parameters, as well as to facilitate discussion. The time interval between point A and B will be designated AB , and so forth. The intervals AB through EF are common to Figure 10.1 as well as Figures 10.2-10.3, and correspond to identical time intervals.

The interplanetary data (Figure 10.1) during the 18 hour interval AB show a solar wind flow with nominal values of $V_{sw} = 400$ km/s and $n_{sw} = 5$ cc⁻¹, corresponding to a weak dynamic solar wind pressure and a quiet time magnetopause standoff distance $\sim 10.25 R_E$. The IMF $B \sim 4.5$ nT and $B_z \sim 1$ nT northward, implying very little solar wind - magnetospheric coupling (as discussed in Chapters 3 and 5, a southward B_z leads to an enhanced coupling of solar wind energy into the magnetosphere). Indeed, the parameters in the top 3 panels of Figure 10.2 show interval AB indicate a very quiet, stable magnetosphere, with an average $\Lambda_{eq} \sim 66^\circ$, $Kp \sim 1$, and $D_{st} \sim 0$. The electron flux levels at $L^* = 5.2$ remain constant at all energies, and those at $L^* = 3.6$ are at background levels indicative of an 'empty' slot region.

The interval BC (12 hrs) shows a gradually approaching interplanetary disturbance. The IMF changes minimally, with B increasing slightly from 4.5 to 7 nT

and B_z remaining predominantly northward at ~ 2 nT. V_{sw} decreases from 400 to 360 km/s. However, n_{sw} gradually rises from 5 to 15 cc^{-1} leading to a modest compression of the dayside magnetosphere, decreasing the empirical standoff distance from $R_s=10.25$ to $9 R_E$. Aside from the 'jitter' about their quiet time values, there is no meaningful change

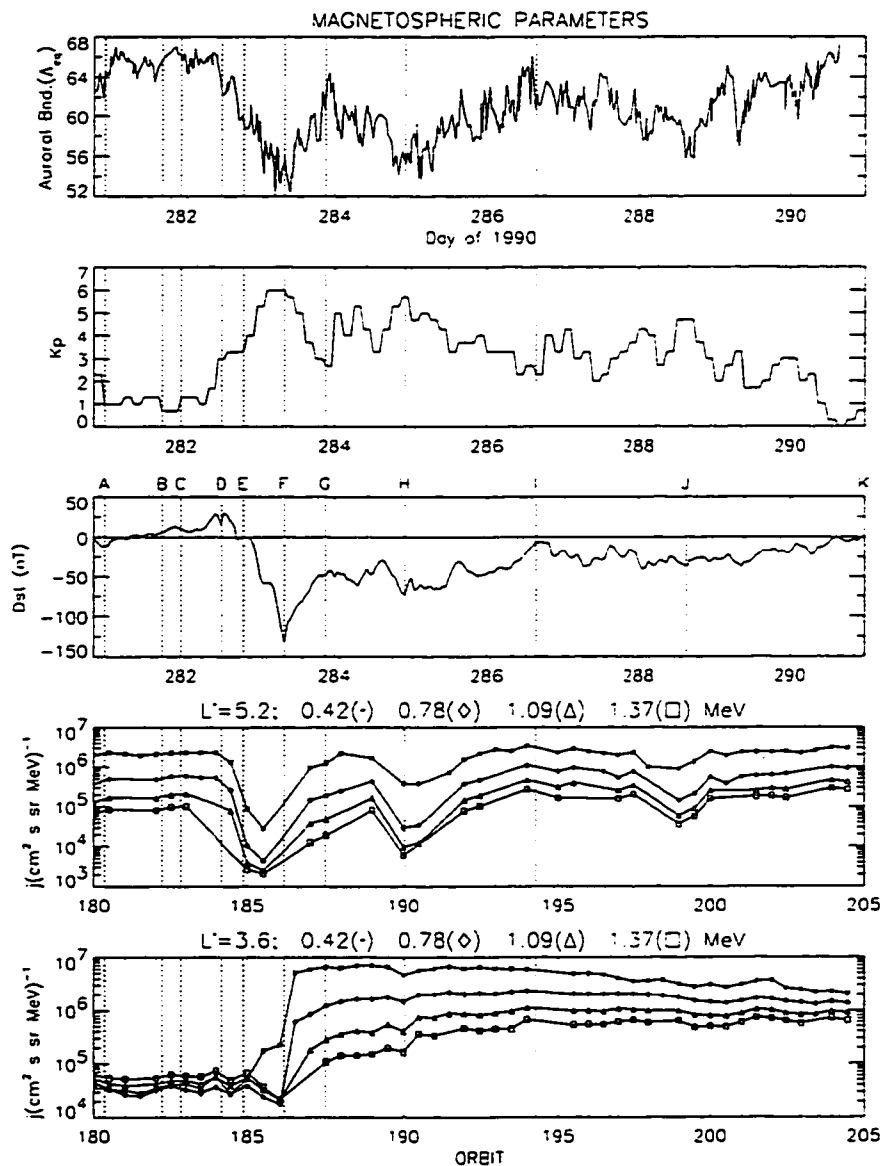


Figure 10.2 : Survey of magnetospheric parameters and electron flux.

in Λ_{eq} , K_p , or electron fluxes. Dst does continue to slowly but steadily rise, indicating a gradual increase in the geomagnetic field due to the compression as R_s decreases to $9 R_E$.

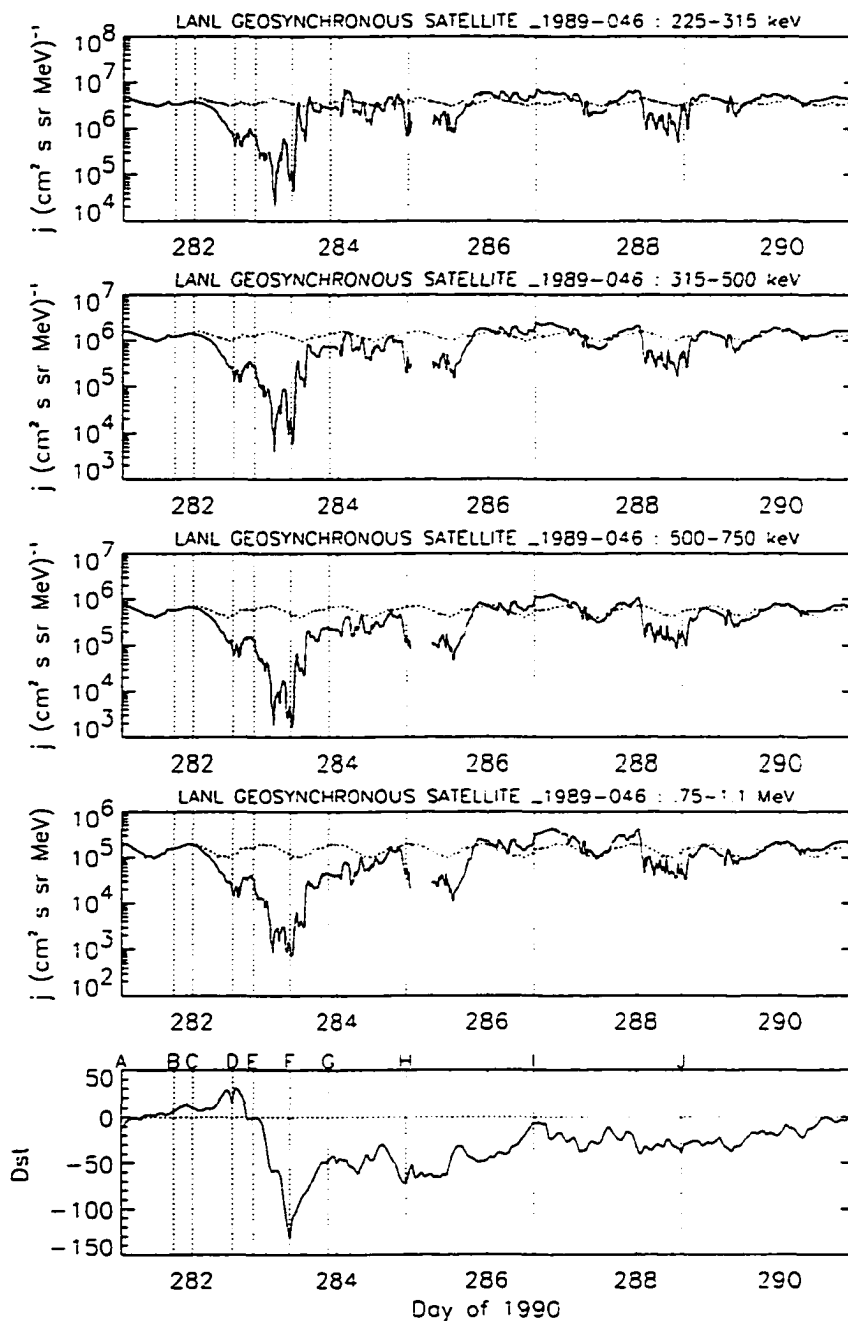


Figure 10.3 : Survey of LANL geosynchronous electron flux.

During interval *AC*, the geosynchronous fluxes (Figure 10.3) exhibit a smoothly varying oscillation with a period of 24 hours. This diurnal effect [*Brown*, 1968] is the result of the day-night asymmetry of the geomagnetic field, and is quite distinct during magnetically quiet times. This quiet time diurnal variation observed for day 281 has been reproduced for days 282-289 as a reference with which to measure relative variations during the disturbed period. The fact that the dayside magnetopause has been compressed to $9 R_E$ during this interval *AC* has no apparent effect on geosynchronous electrons.

Interval *CD*, which culminates in the sudden storm commencement, shows no significant changes in B , B_z , or V_{sw} , relative to the previous interval. However, n_{sw} jumps from 15 to at least 36 cc^{-1} . Unfortunately, the precise parameter values at the time of the SSC are unknown because of a data gap (*Murphy!*) which extends from ~ 2 hours before, to ~ 7 hours beyond, the SSC. However, from the existing data, it is inferred that the magnetopause was compressed from $R_s=9$ to at least $7.5 R_E$ preceding the SSC. This abrupt compression is mirrored in the sharp rise in Dst from 9 to 27 nT. The Kp index jumps from 1 to 3, the Λ_{eq} begins to drop, but no changes are observed in the CRRES electron fluxes at $L^*=3.6$ or 5.2. In Figure 10.3, however, the effect of the dayside compression can be seen in the geosynchronous fluxes (with a higher time resolution for a fixed radial position compared to CRRES). It can be seen that starting at the beginning of interval *CD*, the fluxes decrease below day 281's quiet time reference flux level. This flux decrease correlates with the increase in Dst and the decrease in R_s , and ends with the SSC. The close tracking of Dst and geosynchronous fluxes with R_s during this interval

(without any dramatic slope changes) provides reassuring evidence that despite the data gap in solar wind parameters, the minimum standoff distance is $R_s \approx 7.5 R_E$ and that n_{sw} doesn't rise much higher than the observed value. *[Note: The dip in Dst right at the SSC consists of three points (27, 16, 30 nT) and it is not clear whether this is a real physical effect or a data glitch of some sort. In any event, assuming it is real, it is in the wrong direction to signify a further decrease in R_s .]* This pre-SSC flux decrease may be the result of 'magnetopause shadowing'. This effect is the result of the dayside magnetopause being compressed to the point where electrons following once closed drift shells now intersect with, and are lost through, the magnetopause [West, 1979]. The decrease observed during this interval in the LANL data is certainly not related to the main phase 'Dst' effect, as the build up in ring current has not yet begun.

There are no interplanetary parameters available during interval *DE*, the beginning of the storm main phase. The auroral boundary drops from $\Lambda_{eq} \sim 62^\circ$ to $\sim 58^\circ$ and K_p remains steady at a moderate value of 3. Dst drops back to 0, and 7 hours following the SSC, there is still no enhanced ring current. The CRRES electron fluxes at $L^*=5.2$ have begun to decrease, but still no change at $L^*=3.6$. At geosynchronous, fluxes actually increase slightly to a plateau, in contrast to the CRRES fluxes.

Beginning with the ~ 12 hour interval *EF*, the main phase of the storm really begins. It is from this point that D_{st} begins its dive to its minimum of -133 nT which marks the end of the main phase and the beginning of the recovery phase of the storm. Also during this interval, B remains > 10 nT, while B_z turns southward to as low as -12 nT. This sustained southward B_z (at least 11 hours) greatly enhances the convection

electric field which accelerates 10s of keV electrons and ions into the $L^* \sim 4$ region. This newly energized particle population pumps up the ring current resulting in a depressed geomagnetic field signature at Earth, and hence, the abrupt drop in D_{st} characteristic of the main phase. As the ring current builds to its maximum, K_p increases to its maximum of 6, and Λ_{eq} decreases to $\sim 53^\circ$ signifying the earthward motion of the inner edge of the tail current sheet and the associated thinning of the tail field [Kaufmann, 1987].

Coincident with these changes is an electron flux decrease (to background levels in some cases) seen at all energies ($> .3$ MeV) in both CRRES (at $L^*=5.2$) and LANL data.

Large uncertainties still surround these main phase flux decreases. It is difficult to determine to what extent the decrease is due to the adiabatic ' D_{st} effect', 'magnetopause shadowing', pitch angle scattering into the loss cone, or some other loss process. This will be discussed further in Chapter 13. At $L^*=3.6$, the 0.42 MeV electrons increase by a factor of ~ 5 .

The ~ 1 week long recovery phase (interval FK) begins at point F where the parameters displayed in Figure 10.2 can be seen reversing their main phase trends (the interplanetary parameters in Figure 10.1 are unavailable until the very end of the recovery and will not be further referenced). During the ~ 6 hour interval FG there is a rapid reconfiguration of the magnetosphere, when the auroral boundary moves poleward from $\Lambda_{eq} \sim 53$ to $\sim 64^\circ$ (tail current sheet moves anti-sunward), K_p drops from 6 to 3, and D_{st} increases from -133 to -50 nT. Within an hour following the onset of the recovery phase, an injection of 100s of keV electrons is observed at CRRES apogee. The injection leads to flux increases which are most pronounced where the 'slot' fills in (lower

L* and lower energies). At L*=5.2, by the end of interval *FG*, fluxes at all energies fall short of pre-SSC levels, though they are still rising.

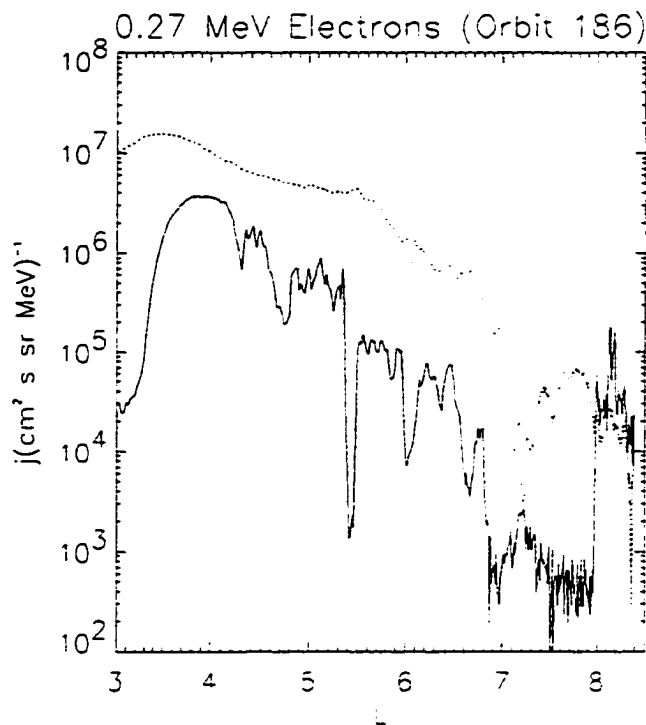


Figure 10.4 : Orbit 186 survey of 0.27 MeV electron flux with injection at CRRES apogee.

A high time resolution plot of orbit 186 (Figure 10.4) shows the injection of 0.27 MeV electrons at CRRES apogee. In this figure, electron flux is plotted versus L, with the ascending leg of the orbit shown with a dashed line and the descending leg, with a solid line. During the ascending leg, the flux is at background levels for L=7-8. At L~8 (13.25 hr UT), the injection appears as the flux increases nearly three orders of magnitude above background level. The injection has a very steeply falling spectrum, $j(E) = 14.53 \cdot 10^{-7.352} (\text{cm}^2 \text{ s sr MeV})^{-1}$, with >0.5 MeV electrons below background. It is interesting to note the periodic dips in flux during the ascending leg of the orbit, from

which it may be suggested that due to the highly stretched and thinned tail magnetic field (see Chapter 11), CRRES is skimming the outer belt trapping boundary at these high magnetic latitudes ($>25^\circ$). Following the injection, associated with a dipolarization of the field (see Chapter 11.3), CRRES becomes engulfed by the trapped region with much elevated fluxes.

Interval *GH* (~24 hours) is an active but quite variable time period, with the auroral boundary decreasing from $\Lambda_{\text{eq}} \sim 64^\circ$ to $\sim 54^\circ$ and K_p jumping up and down between 3 and 6. The Dst index does not show as much variability, fluctuating about -50 nT. During this interval, electron fluxes at $L^*=5.2$ reach a local maximum followed by a short term decrease. At $L^*=3.6$, the 0.42 MeV electrons remain at a fairly constant level while the higher energies continue to rise.

The magnetospheric parameters show similar behavior throughout intervals *HI* (~38 hours) and *JK* (~58 hours), though the behavior is most pronounced in interval *HI*. Both intervals show an overall decrease in magnetospheric activity: auroral boundary retreats poleward (tail current sheet moves tailward), K_p decreases, and Dst increases (ring current decays). The interval between these two, *IJ*, shows a very slight trend towards increasing activity, most obvious in the auroral boundary moving equatorward. The electron fluxes at $L^*=5.2$ track the magnetic activity inversely, with the greatest rise through interval *HI*, a slight fall during *IJ*, and a slight rise through *JK*. The electron fluxes at $L^*=3.6$ are more isolated from the magnetic activity effecting the higher L^* . After responding to the injection into the slot region, beginning around marker *H* (orbit

190), the 0.42 and 0.78 MeV electrons continuously decay while the >1 MeV electrons gradually increase throughout the remaining intervals.

The apparent correlation between the indices in the top three panels and the electron flux at $L^*=5.2$ (on the time scale of fractions of days) is suggestive that the electrons are responding adiabatically to the gross magnetic field variations reflected in the magnetospheric activity parameters. However, despite possible adiabatic effects from the ring current and tail current, there are quite clearly non-adiabatic processes at work here. The geomagnetic field during orbit 180, and ~ 10 days later during orbit 204, is in nearly an identical quiescent state, as can be inferred from a set of nearly identical magnetospheric activity parameters ($\Lambda_{eq} \sim 66^\circ$, $K_p \sim 1$, and $Dst \sim 0$), as well as nearly identical orbital B field plots (Figures 11.2 and 11.7). Assuming that only adiabatic processes transpired over that 10 day period, then the electron flux profiles measured during orbits 180 and 204 should be identical. The fact that electron fluxes at $L^*=3.6$ as shown in Figure 10.2 have increased ten-fold clearly points to some non-adiabatic process(es). The issue of adiabatic variations is addressed in Chapter 13.

The color survey plot of electron fluxes, included here as Figure 10.5, provides a more inclusive snapshot of the storm period for a continuous range of L^* . There are no new features revealed here which haven't already been discussed within the context of Figure 10.2, so the discussion will be brief. The flux intensity is color coded and is units of electrons/($\text{cm}^2 \text{ s sr MeV}$). L^* is plotted along the y-axis, with orbit number along the x-axis. From the top panel down, the fluxes plotted are for electron energies 0.34, 0.78, 1.09, and 1.47 MeV; all at fixed second invariant $J=1.78 \cdot 10^{-16} \text{ g}(\text{cm/s})R_E$. The slot

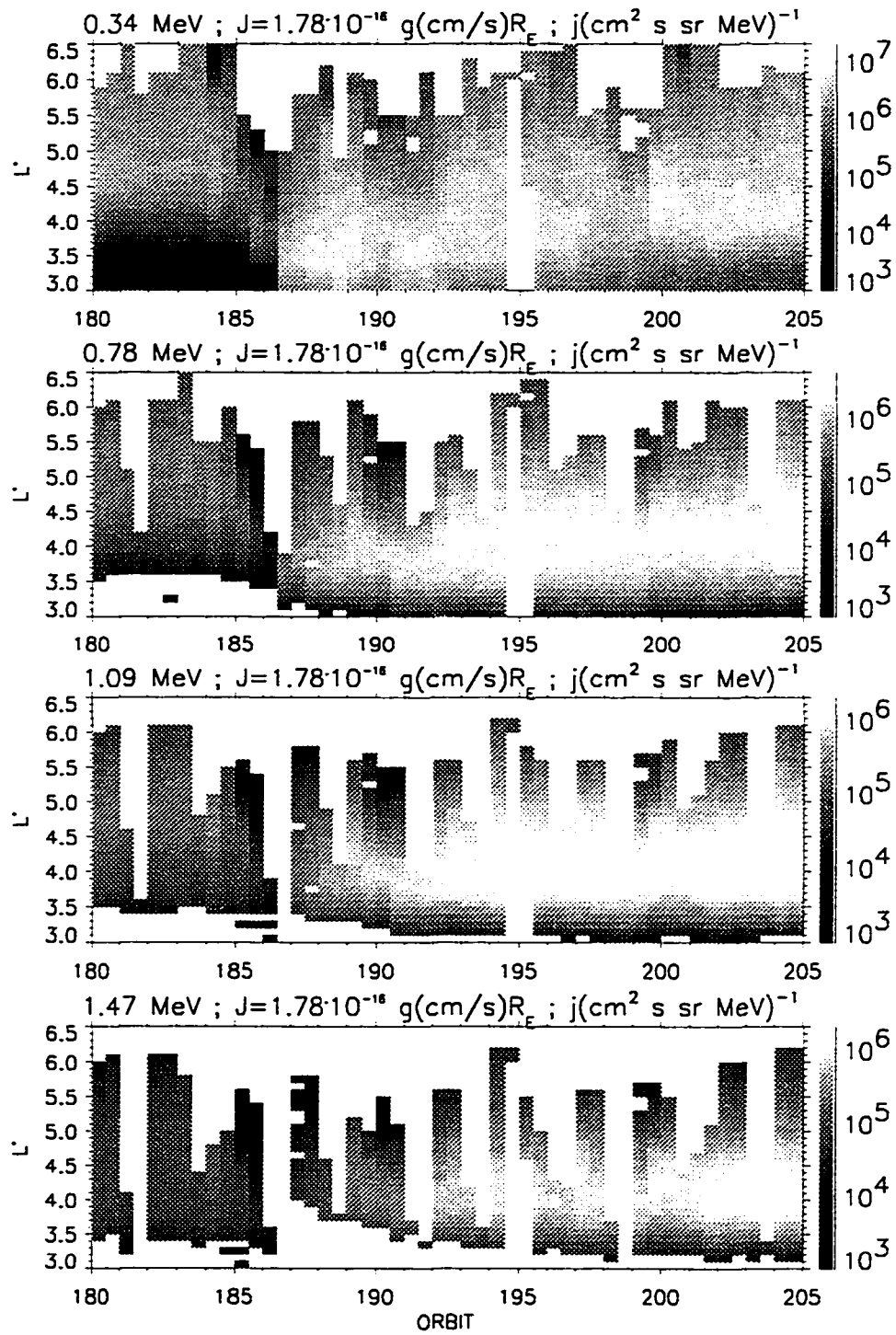


Figure 10.5: Survey of electron flux.

region is easily identifiable in the 0.34 MeV fluxes (top panel) as the deep blue below $L^*=3$ for orbits < 186 . Since the outer edge of the inner radiation belt is below $L^*=3$, the full extent of the slot is not shown in this figure. The fall off in fluxes following the SSC in orbit 184 can be seen in all energies. If one draws an imaginary line through the four panels at orbit 187, it is clear that the injection deep into the slot is limited to the lowest energies. The higher energy fluxes rise gradually through the following several orbits. The decay of 0.34 MeV electron flux below $L^*=3.5$ is apparent; the result of the plasmaspheric whistler waves pitch angle scattering the freshly injected electrons into the atmospheric loss cone.

10.2 Quasi-Static Electric Field

As discussed in Section 7.1, radial diffusion is proportional to the square of the electric field fluctuation amplitude at frequencies comparable to the electron azimuthal drift frequency. It is therefore of interest to examine how the electric field fluctuation amplitude varies through the storm.

The y-component (MGSE coordinates, see Appendix A) of the CRRES electric field measurements (Section 9.3) is plotted for several orbits in Figure 10.6. The $\mathbf{V}_s \times \mathbf{B}$ component of the electric field seen by the moving satellite (\mathbf{V}_s) has been subtracted from the total. Each panel is an orbital plot of E_y versus time (UT, hr) from $L^*=3$ to apogee (ascending leg) and back to $L^*=3$ (descending leg). The top two panels (orbits 182 and 183) represent the magnetically quiet time ($K_p \sim 1$) period before the SSC. An average peak to peak amplitude is ~ 0.4 mV/m which gives $E_{rms} \sim 0.14$ mV/m ($E_{rms} = 0.35 \cdot E_{pk-to-pk}$).

During orbits 184 and 185 (the next two panels), the SSC occurs (orbit 184, 13.25 hr UT) and K_p rises from 1 to 6. Some very large amplitude (~ 5 mV/m) coherent oscillations (estimated at 3 to 4 mHz by counting peaks) are seen near geosynchronous altitude during orbit 184, and by orbit 185 the fluctuation amplitudes have become significantly larger ($E_{rms} \sim 0.3$ to 1.0 mV/m) throughout much of the inner region ($L^* < 5$). For orbits 186, 189, and 190 (bottom three panels) magnetic activity remains moderately high, with K_p varying between 4 and 6, and significant amplitudes ($E_{rms} \sim 0.2$ to 2 mV/m) are observed throughout the inner magnetosphere. The injection of < 0.5 MeV electrons into the slot region occurred during the second leg of orbit 186 when some very well ordered 2-3 mHz oscillations are seen for $L^* < 6$. This frequency range corresponds to the drift frequency of ~ 1 MeV electrons at $L^* \sim 5-6$. During orbits 189 and 190 there are coherent mHz waves throughout much of the inner magnetosphere (seemingly more coherent for the descending leg, 6-7 MLT, then for the ascending leg, 2-3 MLT).

Although E_y amplitudes vary widely with L^* , the bottom line here is that even a cursory glance at these seven orbits shows that on average E_{rms} significantly increases with magnetic activity (K_p).

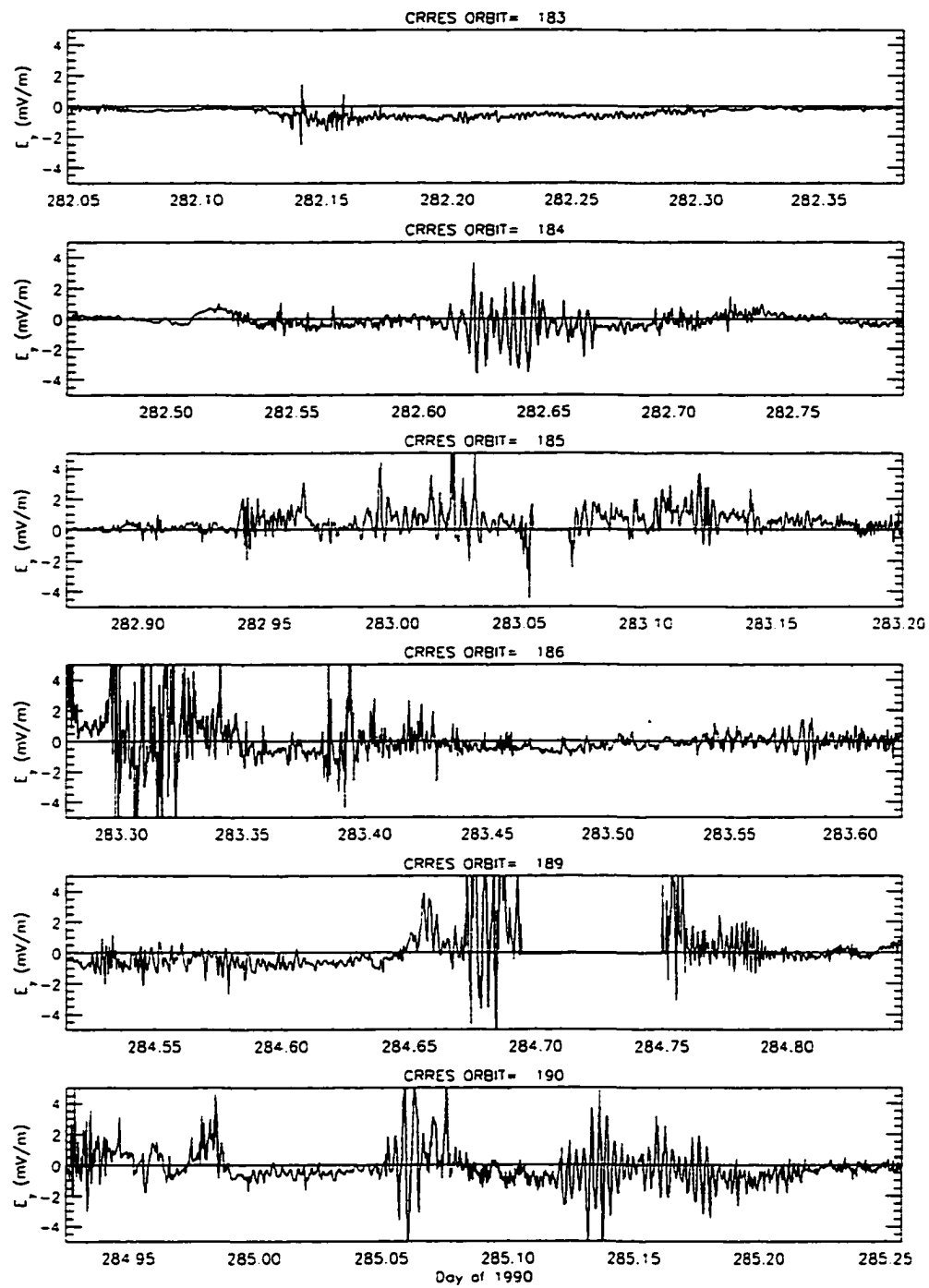


Figure 10.6 : Electric field survey for orbits 183-186 and 189-190.

CHAPTER 11

MAGNETIC FIELD MODEL

11.0 Introduction

In order to properly analyze the dynamics of the electron population, it is necessary to examine the time variation of phase space density in terms of the three adiabatic invariants. To calculate the three invariants, the magnetic field all along the electron's drift shell must be known or assumed. Since it is virtually impossible to measure the magnetic field at all points for all times, a model magnetic field must be assumed. In order to compensate for adiabatic variations induced by a gradually changing magnetic field, it is necessary to use a time dependent model which is parameterized by some magnetospheric parameter(s). Because the magnetic field plays such a critical role, effort is made to select a model which most successfully reproduces the CRRES magnetic field measurements.

The geomagnetic field is modeled as the sum of an internal plus an external magnetic field. The internal field to be used here is the International Geomagnetic Reference Field (IGRF). The IGRF model assumes that the internal geomagnetic field is generated by currents internal to the Earth. The magnetic field within the volume above the surface of the Earth and below the region of external currents may thus be expressed as the gradient of a magnetic scalar potential. This potential may be written as a

spherical-harmonic expansion (truncated according to desired accuracy and empirical precision) whose coefficients are fit to observations. The IGRF model is essentially a table of these expansion coefficients. One further complication which is accommodated by the IGRF model is the tilt of the Earth's dipole moment relative to its spin axis which introduces a diurnal effect. The universal time (UT) as well as spatial coordinates are thus provided as the input parameters to the IGRF model. There is also an epochal variation in the internal field which requires that the IGRF model is updated every five years. This analysis uses the 1985 version of IGRF (IGRF85).

Beyond a radius of 2-3 R_E the magnetic field becomes increasingly affected by external current systems so that the field is no longer amenable to spherical-harmonic analysis. Thus, separate external field models are developed which are combined with the internal model to give the total geomagnetic field. The successful external field model must represent the major magnetospheric current systems, including: the magnetopause surface current, the tail current, and the ring current. These current systems all vary in time and the external field models must be parameterized in such a way as to mimic this time variation.

11.1 Selection of Magnetic Field Model

In selecting a magnetic field model to be used in this storm analysis, several models are compared with the CRRES fluxgate magnetometer measurements. Although not expected to compete with the success of the external plus IGRF85 field models, two 'internal' field models, the dipole and the IGRF85 model, are compared with CRRES

measurements as a reference. The following three external field models (in combination with the IGRF85 model) are also compared with CRRES measurements: Hilmer-Voigt [Hilmer and Voigt, 1995], Olson-Pfitzer dynamic [Olson and Pfitzer, 1982], and Tsyganenko [Tsyganenko, 1989]. The Hilmer-Voigt (HV) and Tsyganenko (T89) models may both be parameterized by Kp, whereas the Olson-Pfitzer (OP) is parameterized by Dst and the stand off distance.

A comparison of the magnetic field magnitude (B) and three components (B_x, B_y, and B_z in GSM coordinates) is made between the CRRES field measurements and the individual models. For every time step (1 minute) of a given orbit (above a radius of 3 R_E), the model field is determined and its difference from CRRES measurements is calculated for each of the three components and magnitude as $\Delta \equiv \text{abs}[(B_{\text{CRRES}} - B_{\text{model}})/B_{\text{CRRES}}]$. Individual histograms for this difference are made for three different time periods: the four quiet orbits (180-184) leading up to the SSC, the twenty orbits following the SSC (185-204), and the entire interval (orbits 180-204). The results are summarized below (Table 11.1), with a separate table for each of the three orbit intervals: orbits 180-184 (Table 11.1a), orbits 185-204 (Table 11.1b), and orbits 180-204 (Table 11.1c). The percentage of points which yielded a fractional difference (Δ) <0.10 and <0.20 are given in the columns for each of the field components and for each model.

As would be expected, all model fields show the best agreement with CRRES measurements during the magnetically quiet time (Table 11.1a) when the geomagnetic

Table 11.1c shows that Tsyganenko (T89) is the most successful in reproducing CRRES measurements, with 92% of all fractional differences of B within <0.10 (out of all 25 orbits). The next most successful was OP with 79%.

Table 11.1a: CRRES and Model Field Comparisons (Orbits 180-184)

	ORBITS 180-184 (% of points with $\Delta < 0.1, 0.2$)			
	Bx	By	Bz	B
DIPOLE	39, 64	64, 92	43, 77	83, 100
IGRF	47, 65	85, 94	41, 77	87, 100
HILMER-VOIGT	67, 81	90, 96	77, 94	98, 100
OLSON-PFITZER	55, 72	87, 95	54, 75	92, 100
TSYGANENKO	72, 83	90, 96	97, 99	99, 100

Table 11.1b: CRRES and Model Field Comparisons (Orbits 185-204)

	ORBITS 185-204 (% of points with $\Delta < 0.1, 0.2$)			
	Bx	By	Bz	B
DIPOLE	35, 56	47, 72	16, 35	66, 92
IGRF	39, 55	43, 79	14, 33	65, 88
HILMER-VOIGT	64, 79	57, 86	50, 75	66, 96
OLSON-PFITZER	49, 65	64, 89	44, 62	76, 93
TSYGANENKO	65, 81	84, 94	59, 81	89, 97

Table 11.1c: CRRES and Model Field Comparisons (Orbits 180-204)

	ORBITS 180-204 (% of points with $\Delta < 0.1, 0.2$)			
	Bx	By	Bz	B
DIPOLE	35, 57	51, 76	22, 45	70, 94
IGRF	41, 58	53, 83	20, 43	70, 91
HILMER-VOIGT	65, 80	65, 88	56, 80	73, 97
OLSON-PFITZER	50, 67	69, 91	46, 65	79, 95
TSYGANENKO	66, 81	85, 95	68, 85	92, 98

It is not the intent here to investigate why any one model did better or worse in reproducing any particular component of the CRRES measurements. It is apparent that T89 fared better than the others in agreement with CRRES, and for this reason, it was

It is not the intent here to investigate why any one model did better or worse in reproducing any particular component of the CRRES measurements. It is apparent that T89 fared better than the others in agreement with CRRES, and for this reason, it was chosen for the modeling of this thesis. In the following sections, a brief description of T89 will be given, and a comparison between CRRES, T89, and IGRF will be presented on an orbit by orbit basis.

11.2 Tsyganenko 1989 Magnetic Field Model

The Tsyganenko 1989 (T89) magnetic field model [Tsyganenko, 1989] is a semi-empirical model which provides a different magnetic field configuration for 6 levels of magnetospheric activity as specified by K_p ($K_p = 0, 1, 2, 3, 4,$ and ≥ 5). Analytical expressions are developed to describe the three major magnetospheric current systems (magnetopause boundary, magnetotail, and ring current) in terms of various fixed and adjustable parameters. Two large magnetic field databases are then separated by K_p , and these subsets are then used to optimally fit the adjustable parameters.

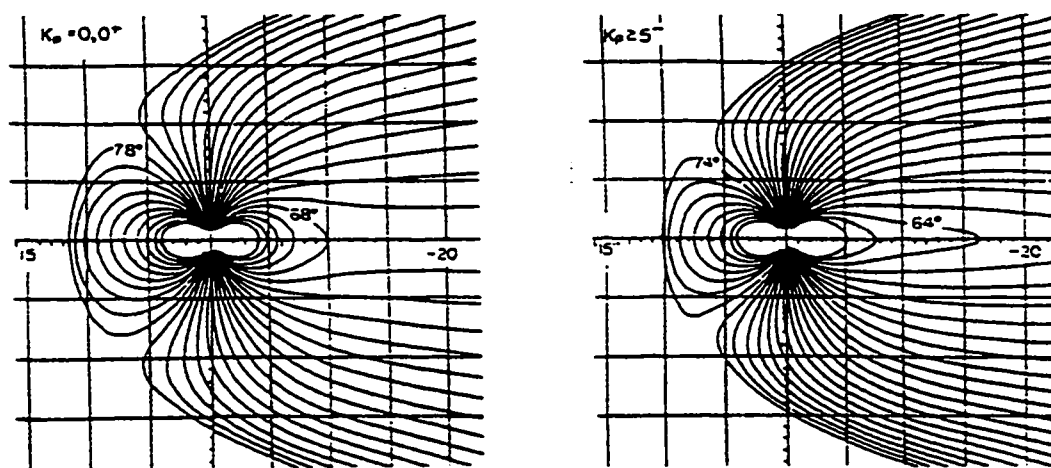


Figure 11.1 : Model magnetic field line profiles for $K_p=0$ (left) and $K_p \geq 5$ (right) [Tsyganenko, 1989].

The magnetic field lines in the x-z plane (in GSM coordinates, see Appendix A) are shown in Figure 11.1a for the lowest activity case ($K_p=0$), and Figure 11.1b for the highest activity case ($K_p \geq 5$). Both are given for a dipole tilt of 0° meaning that the solar wind flow will be approaching the dayside magnetopause essentially head on (in GSM coordinates, the x-axis points directly towards the sun). The grid is in $5 R_E$ increments, and the field lines emanate from the poles in 2° magnetic latitude increments. The nightside field line stretching ('tail thinning') during active periods is evident when one compares the 64° field line in the two cases shown here. For $K_p=0$, the 64° line crosses the magnetic equator around $5.5 R_E$ and is quite dipolar, whereas for $K_p \geq 5$, the same field line crosses the magnetic equator around $16 R_E$ and is obviously quite 'stressed' from enhanced magnetotail currents. On the dayside, the 74° field line crosses the equator around $10 R_E$ in both cases, though for the $K_p \geq 5$ model the field line appears more compressed from enhanced magnetopause boundary currents.

11.3 Comparison of Model Fields With CRRES Measurements

Since the electron dynamics are largely tied to the Earth's magnetic field, the fidelity of the model field chosen to follow the evolution of the electron population is of significant importance. Comparison between CRRES and IGRF fields provides a measure of the strength of the external fields generated from the various magnetospheric current systems. These include not only the three major global current systems (the magnetopause boundary, ring, and magnetotail currents), but also various localized transient currents associated with magnetospheric disturbances. The T89 model reflects

the variations of the three major current systems in an average sense, as scaled by the magnetic activity index K_p , but is not expected to reproduce the short term (<3 hr) variations observed throughout a storm. However, as the following comparisons show, it does quite well in following the gross changes of the magnetic field which undergoes significant distortion over the course of the several days of this storm.

Figures 11.2(a-e) compare the CRRES (solid line), IGRF (dot-dash), and T89 (dash) magnetic field for each of the three B components and magnitude for orbits 182, 184-187, and 204. In the top to bottom panel, respectively, are plotted B_x , B_y , B_z , and B (y-axis) versus the day of year (x-axis). The y-scale is linear with a fixed magnitude span, but with an origin which may shift up or down to accommodate each particular orbit's B component range. This facilitates the comparison of the relative size of perturbations seen for different orbits. An exception to this is orbit 186 which had an anomalously large range of B_y values and required a scale with twice the span as the typical orbit. Two auxiliary x-axes (non-linear) giving radial distance (r) and magnetic latitude (MLat) have been appended to the bottom of the plot. While sequencing through the sample orbits of magnetic field data to be discussed, it may be of interest to refer back to Figure 10.2 which surveys the magnetospheric parameters throughout the storm.

Orbit 182 (Figure 11.2a) is representative of the quiet before the storm (orbits 180-183) when $K_p=1$. All components vary smoothly, and CRRES and T89 are virtually indistinguishable.

Orbit 184 (Figure 11.2b) is a period when K_p is beginning to increase (from $K_p=1$ to 3) and includes the SSC magnetic field signature between day 282.55 and 282.60. Relative to the IGRF model, CRRES B_x becomes more depressed while B_y is enhanced, with the net result being little deviation in the total B magnitude at the storm onset.

Orbit 185 (Figure 11.2c) follows the SSC and is a period when K_p rises from 3 to 6, and shows significant variability in the various CRRES B components, mainly for $r > 5.2 R_E$. Since the ascending legs of orbits 182 and 185 pass through similar magnetic latitudes, it makes for a meaningful comparison between the two orbits. The pre-SSC orbit 182 shows that at $4.8 R_E$ CRRES B_z is 85% of IGRF B_z . The storm main phase orbit 185 shows that at $4.8 R_E$ CRRES B_z is 74% of IGRF B_z . This decrease in the measured B_z component relative to the internal field is attributed to the main phase enhanced ring current.

The ascending leg of orbit 186 (Figure 11.2d) shows the most dramatic variations in the B components seen throughout the storm. Note that the magnitude of the B_y scale is double that of the preceding figures. For $r < 4.5 R_E$, and at relatively high latitudes ($> 20^\circ$), the B_y component is up to ~ 100 nT above that modeled by either the IGRF or T89 models. In this same range, B_z drops from 225 nT to 20 nT. After further abrupt recoveries and drops, B_z goes negative. At 9.4 hrs UT (around day 283.39) B_z jumps abruptly from 0 to 45 nT, B_y jumps ~ 30 nT, and B_x drops ~ 120 nT, all, coincident with the electron injection discussed in Chapter 10.1 and indicative of a dipolarization of the field.

By orbit 204 (Figure 11.2e), with K_p back to ~ 1 , the geomagnetic field has essentially returned to its pre-SSC state, with all its components showing smooth variations and all within $\sim 5\%$ of T89.

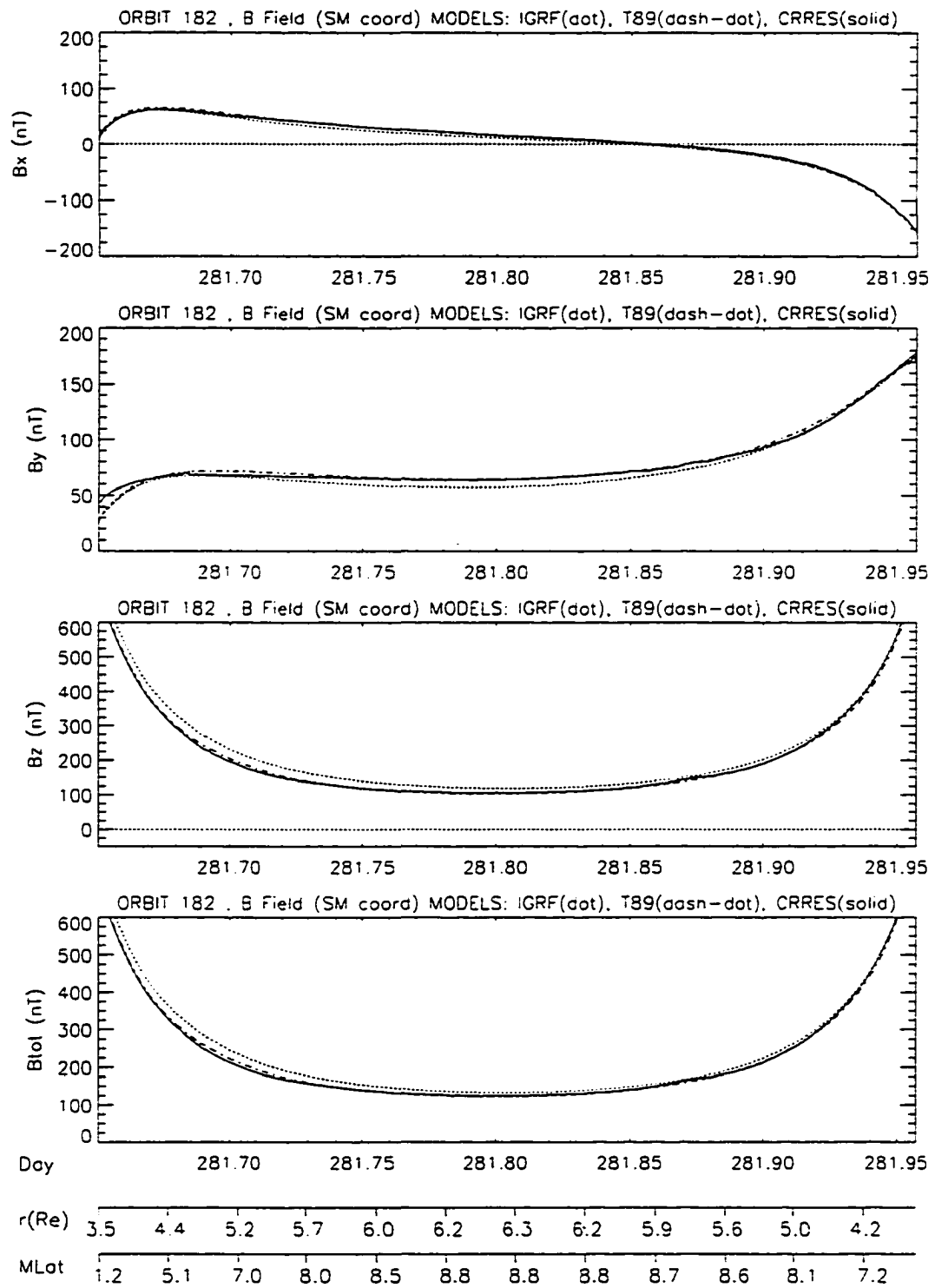


Figure 11.2a : Magnetic field comparison for orbit 182.

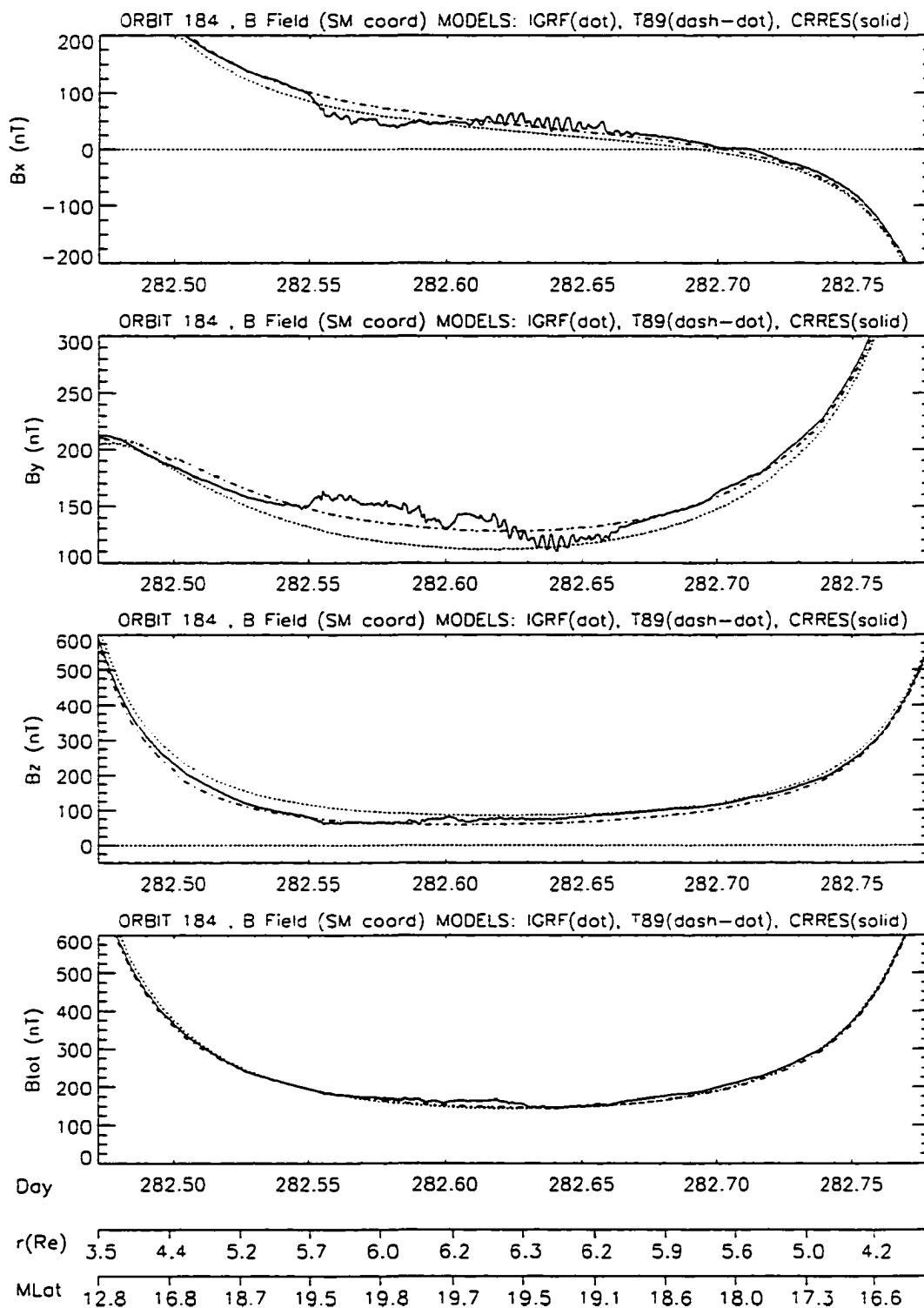


Figure 11.2b : Magnetic field comparison for orbit 184.

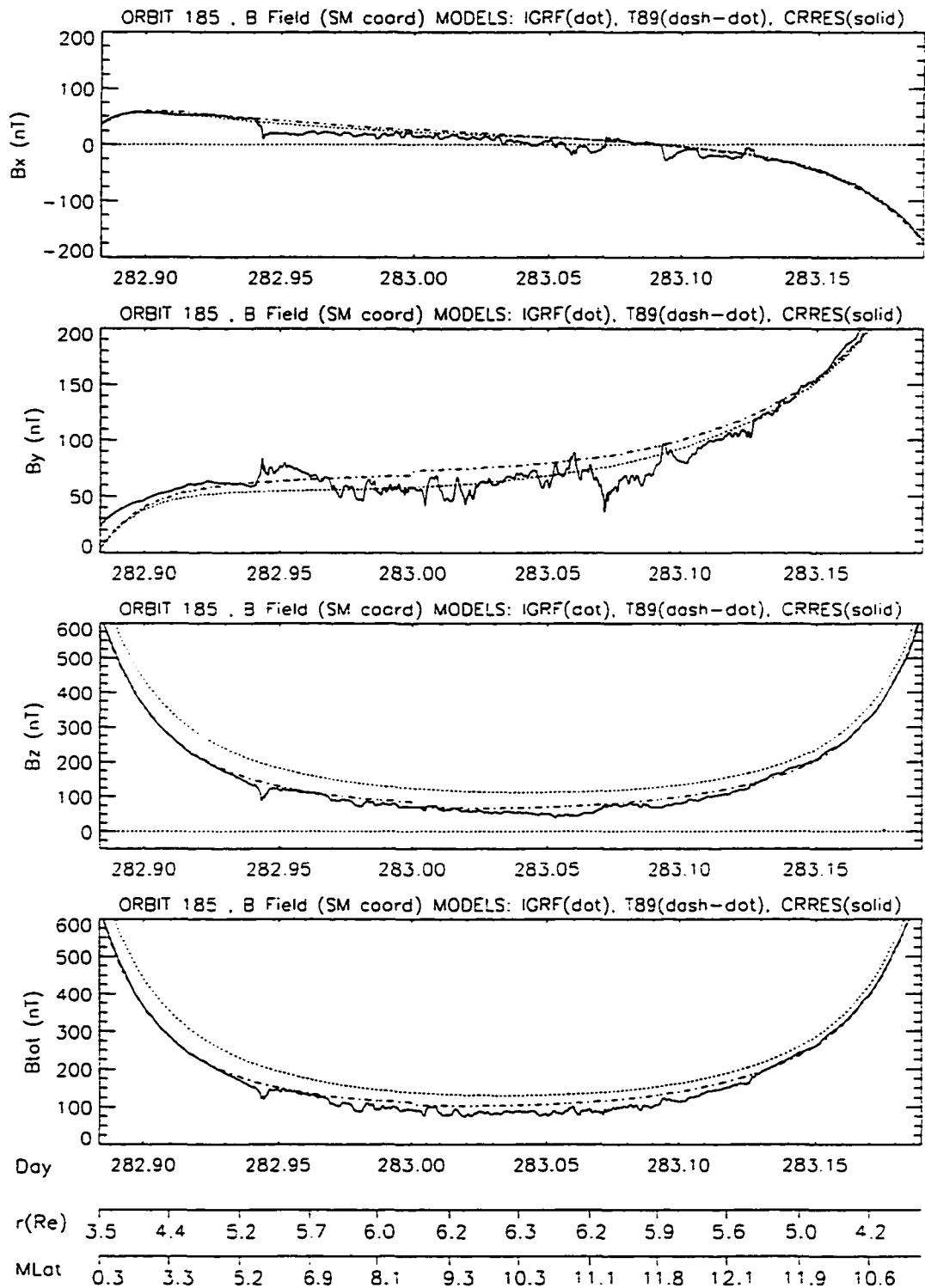


Figure 11.2c : Magnetic field comparison for orbit 185.

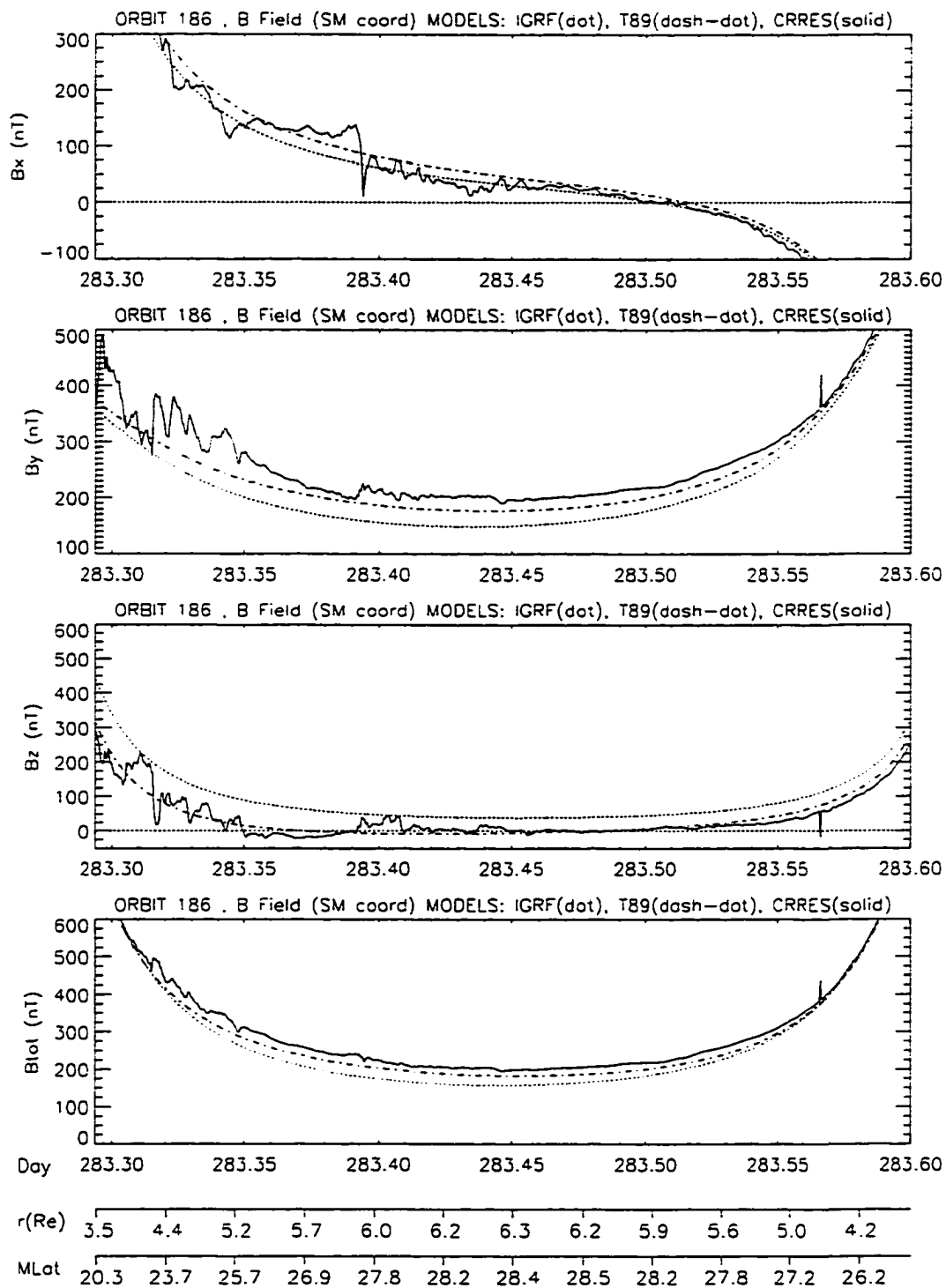


Figure 11.2d : Magnetic field comparison for orbit 186.

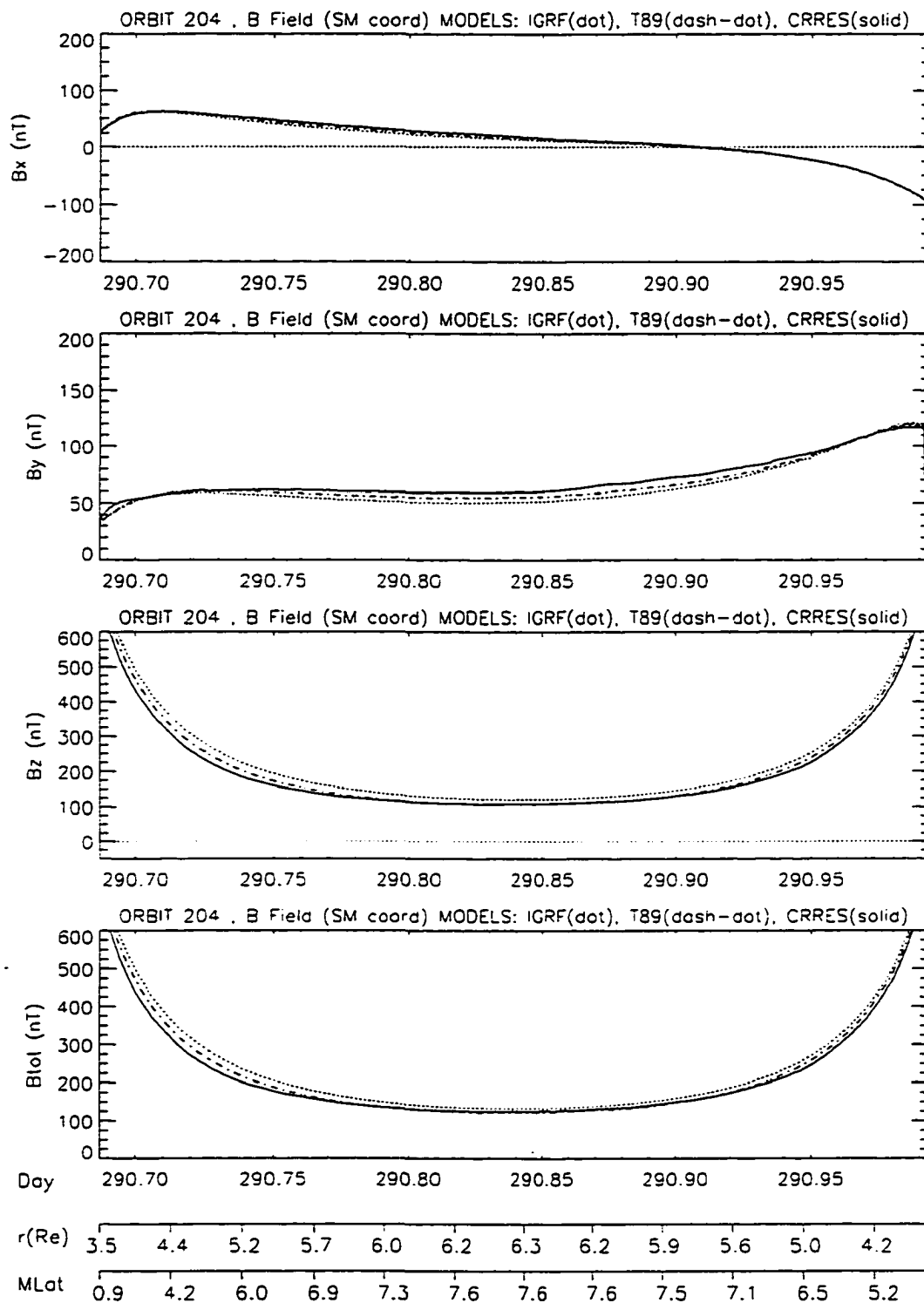


Figure 11.2e : Magnetic field comparison for orbit 204.

CHAPTER 12

TRANSFORMATION OF $j(X,E,\alpha)$ TO $f(\mu,J,L^*)$

CRRES electron measurements were made with a magnetic spectrometer (Chapter 9.1) designed to count the number of electrons within a fixed energy band which pass through an aperture of fixed solid angle within a fixed time interval. The directionality of the electrons is determined relative to the magnetic field vector as measured by CRRES, and is specified by a pitch angle $\alpha = 0^\circ$ to 180° . Using calibrated geometric factors, measured count rates are converted to differential energy fluxes $j(X_{eci}, E, \alpha, t)$ giving the number of electrons/($\text{cm}^2 \text{ s sr MeV}$) at a given energy, pitch angle, and universal time. The satellite ephemeris file tags each time with a set of spatial coordinates in Earth centered inertial coordinates X_{eci} (defined in Appendix A).

To be amenable to theoretical treatment (radiation belt diffusion), the differential fluxes $j(E, \alpha, X_{eci}, t)$ are transformed to a phase space density as a function of the three invariants, $f(\mu, J, L^*; t) = j(E, \alpha, X_{eci}, t) / p^2$. Figure 12.1 presents a flow diagram of the overall data processing scheme for each orbit leg of data for orbits 180-204. One data file (designated by a set of brackets { } enclosing the pertinent data) for each CRRES orbit leg is first created which gives the universal time (t), the Earth centered inertial coordinates X_{eci} , the CRRES (satellite) measured magnetic field magnitude B_s , and the K_p index for every 30 s. This file is the input to the program *roederer.f* which calculates both the bounce integral I

DATA PROCESSING SCHEME

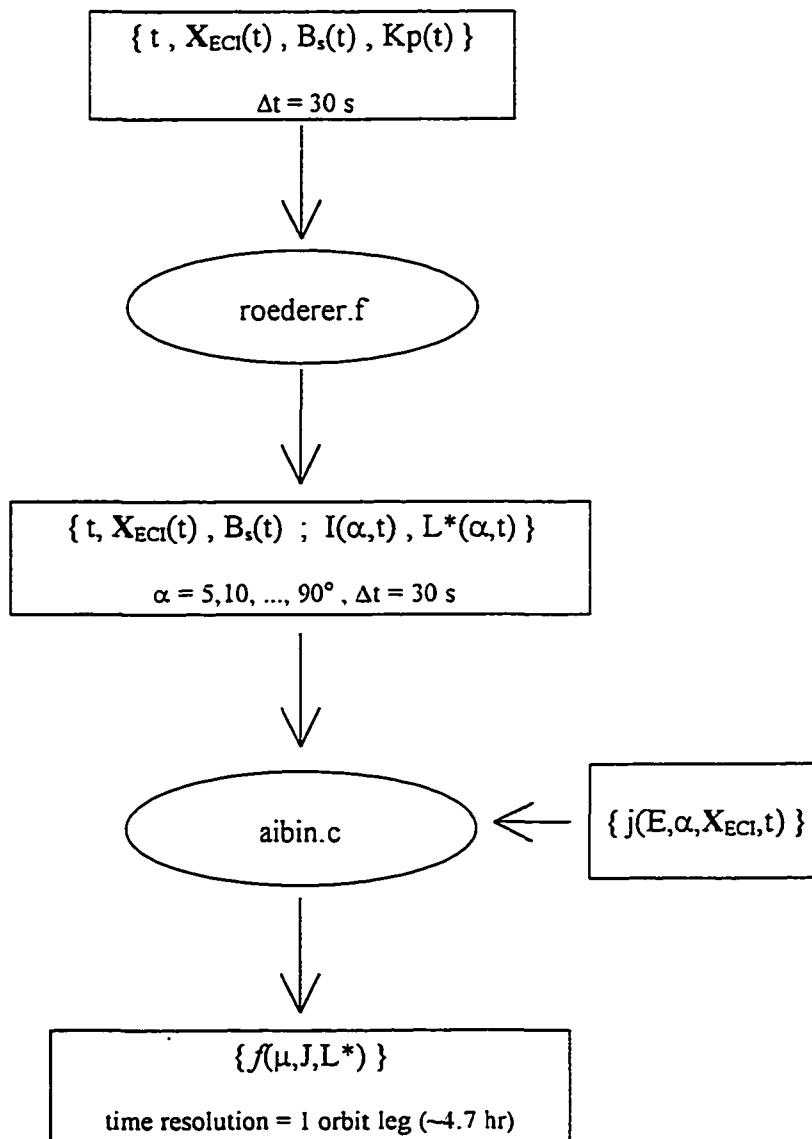


Figure 12.1 : Overall data processing scheme for transforming $j(X, E, \alpha)$ to $f(\mu, J, L^*)$.

used to determine the second invariant $J=2pI$, and the third invariant L^* using the T89 magnetic field model [Tsyganenko, 1989]. The output from *roederer.f* is a file which includes its input, as well as $I(\alpha,t)$ and $L^*(\alpha,t)$ for each time and pitch angle from 5 to 90° in intervals of 5° . This file, along with a file of differential fluxes $j(E,\alpha; X_{eci},t)$ at identical time intervals, are input to a program *aibin.c* which transforms the $\{j\}$ to $\{f=j/p^2\}$, binning f according to the three invariants. For each 30 s time step, the flux array $j(E,\alpha)$ is dimensioned by 14 logarithmically spaced energy channels (0.27-1.58 MeV) and 19 pitch angle bins ($\alpha=0-90^\circ$, $\Delta\alpha=5^\circ$). The phase space density array $f(\mu,J,L^*)$ is defined by 19 μ bins logarithmically spaced from 20 to 1258 MeV/G; 15 J bins logarithmically spaced from 10^{-19} to 10^{-15} g(cm/s) R_E ; and 36 L^* bins from $L^*=3.0 - 6.5$ (0.1 wide). The simplified algorithms for the programs *roederer.f* and *aibin.c* are outlined in Appendix B.

It is unusual to see particle (electron) data binned in all three invariants. It is more typical (provided electron measurements are somewhat near the equator), and far simpler, to assume equatorially mirroring electrons (second invariant $J=0$). For the case of $J>0$, a range of pitch angles and energies fall within a given invariant bin, and Figures 12.2 and 12.3 illustrate what this range is.

Figure 12.2 consists of four panels, each for a fixed μ (designated in the title of each panel). For the range of orbits covered in this study (180-204), J is plotted versus equatorial pitch angle (α_0) for $L^*=3.5$ (+ symbol) and 5.5 (* symbol). For $\alpha_0 = 90^\circ$, the electron mirrors at the equator and its bounce invariant ($J=0$) obviously can not be included on the log scale necessarily used here. Since there are relatively few points where $J=0$, it has been included in the lowest non-zero J bin. For decreasing α_0 , the electron mirrors farther down

the field line towards the Earth, and its J increases. For an intermediate value of $\mu=316$ MeV/G, and for $J=1.8 \cdot 10^{-16}$ g(cm/s) R_E , the range of α_0 is 30 to 55° for the range of $L^*=3.5$ -5.5 typically found in the analysis in the follow chapters.

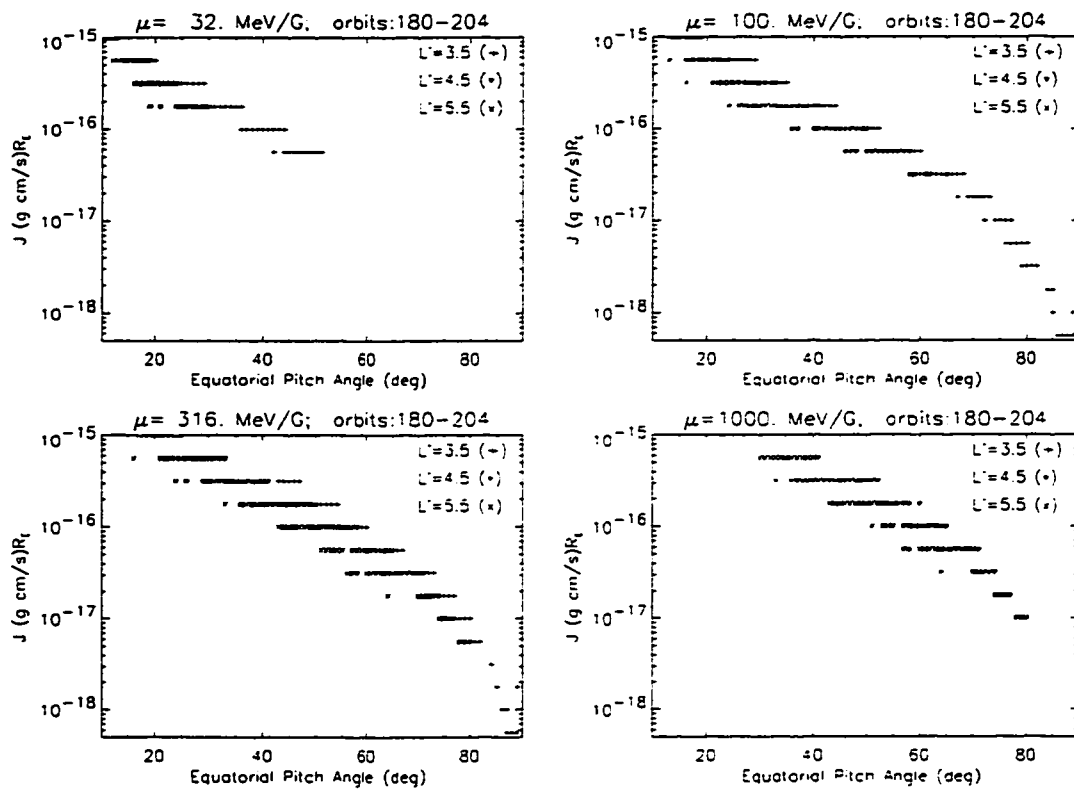


Figure 12.2 Second invariant (J) dependence on equatorial pitch angle for fixed μ and L^* .

Figure 12.3 consists of four panels, each for a fixed J (designated in the title of each panel). For the range of orbits covered in this study (180-204), μ is plotted versus energy for $L^*=3.5$ (+ symbol), 4.5 (* symbol), and 5.5 (x symbol). For a fixed J and μ , the energy increases for decreasing L^* . For $J=1.8 \cdot 10^{-16}$ g(cm/s) R_E , $\mu=316$ MeV/G corresponds to a 0.45 MeV electron at $L^*=5.5$ and a 1.5 MeV electron at $L^*=3.5$.

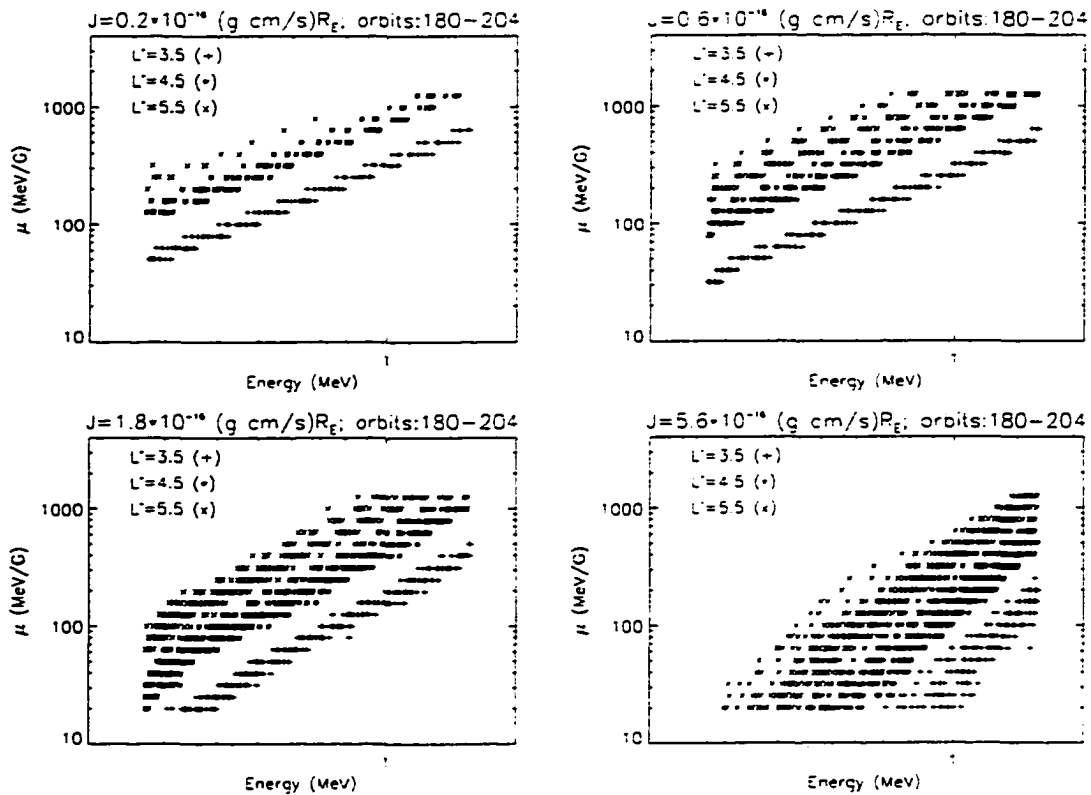


Figure 12.3: First invariant (μ) dependence on energy for fixed J and L^* .

CHAPTER 13

STORM ADIABATIC VARIATIONS

13.0 Introduction

A major obstacle to assessing the dynamic processes affecting the outer zone electrons is the ability to distinguish between the adiabatic and non-adiabatic variations of measured fluxes. With the slowly waxing and waning of the major magnetospheric current systems, the Earth's magnetic field is perpetually changing - displacing electron drift shells radially in and out, conserving the third invariant. As electrons move outward (inward) into regions of lesser (greater) magnetic field strength their energy decreases (increases) so as to conserve their first invariant. Although the adiabatic invariants of a given electron population may be conserved, its energy and radial distribution will vary. Since particle detectors measure fluxes at a given time and position and in a given energy band, a satellite-borne detector will measure temporal flux variations at a fixed point in its orbit simply due to the gradual variation of the magnetic field. It is a difficult task to determine to what extent observed flux variations are adiabatic versus non-adiabatic.

The main phase of a storm is associated with a large build up of the ring current which subsequently depresses the magnetic field within its bounds. The question of adiabaticity therefore arises quite frequently in relation to the large flux decreases observed during the main phase of a magnetic storm, and the ensuing gradual restoration

of these fluxes during the recovery phase (Chapter 6.3). This chapter addresses these issues quantitatively.

13.1 Adiabatic Variation in Flux at Fixed Position and Energy

This section determines the expected flux change, at a fixed position and energy, which would be expected to occur between orbits 182 (pre-SSC) and 185 (post-SSC) assuming purely adiabatic variations. These orbits were chosen for the analysis because they lie nearly in the equatorial plane (within 10°) so that the simplifying assumption of equatorially mirroring ($\alpha=90^\circ$) electrons may be made, setting the second invariant $J=0$. The survey plot of magnetospheric parameters (Figure 10.2) indicates that orbit 182 is a magnetically quiet period with average values of $K_p \sim 1$ and $Dst \sim 10$ nT, and orbit 185 is a moderately active period with average values of $K_p \sim 5$ and $Dst \sim -100$ nT.

Figure 13.1 compares various parameters measured along the ascending legs, for $r=3.5$ to $6.2 R_E$, of orbits 182 and 185. From the top to bottom panel, the parameters being compared are the measured magnetic field magnitude (B), magnetic local time (MLT), magnetic latitude (MLAT), and the 0.5 and 1.2 MeV electron fluxes. The magnetic field during the post-SSC orbit (185) is depressed relative to the pre-SSC orbit (182) by 30-50 nT (25% at $r=6 R_E$; 10% at $r=4 R_E$). The MLT coverage for each orbit is essentially identical, spanning the range of 2 to 5 hr MLT. The satellite trajectory for the 2 orbits is always within 2° MLAT of each other, and the average MLAT of the 2 orbits varies from 1° at $r=3.5 R_E$ to 8.5° at $r=6.0 R_E$. The flux plots clearly show a threshold radius ($r=4.5 R_E$) below which the post-SSC fluxes are greater or equal to the

pre-SSC fluxes, and above which, the decrease between pre-SSC and post-SSC fluxes increases with radius. Apparently the innermost region ($r < 4.5$) of the outer zone is shielded from the process(es) which lead to a decrease in flux for $r > 4.5 R_E$. The remainder of this section will be devoted to quantifying the extent to which the flux decrease may be attributed to purely adiabatic variations.

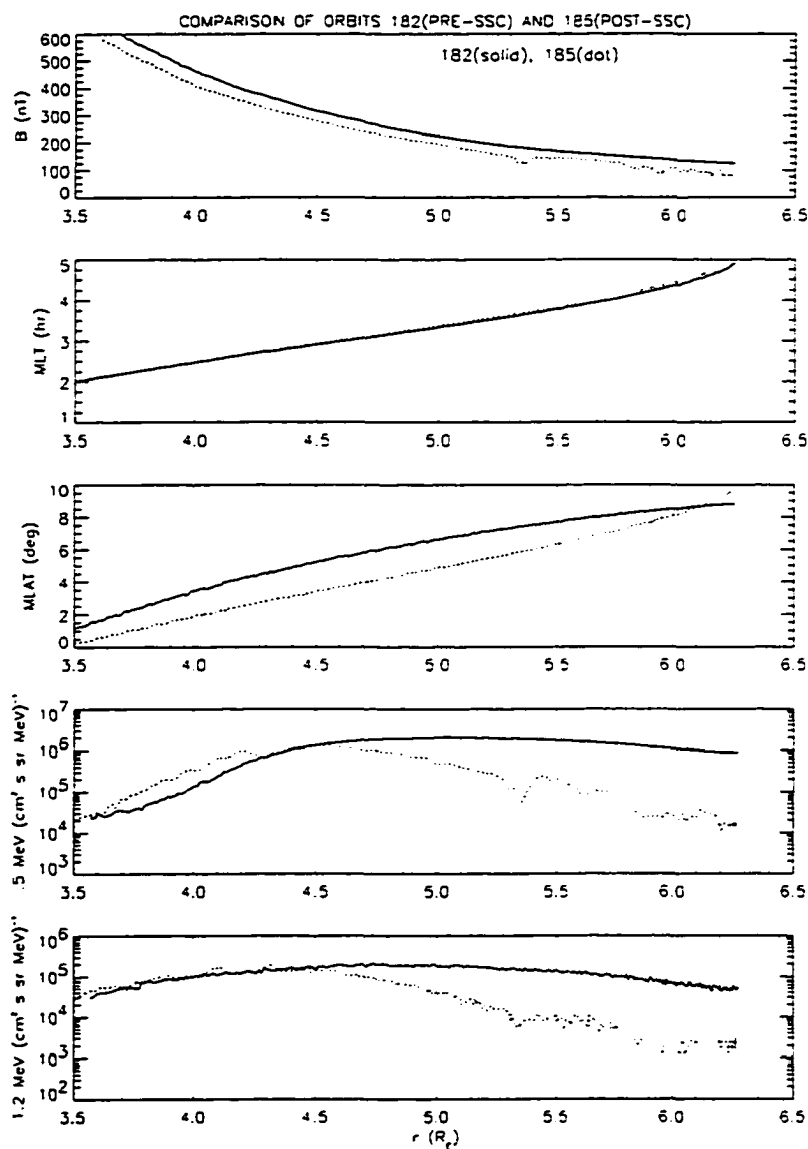


Figure 13.1 : Comparison of orbit 182 and 185 parameters (B, MLT, MLAT, and electron flux).

Figure 13.2a shows an equatorial drift shell ($L^*=3.93$) for equatorially mirroring electrons for both the magnetically quiet time ($Kp=1$, orbit 182 : bold trace) and the magnetically active time ($Kp=5$, orbit 185 : light trace) as determined from the Tsyganenko 1989 field model (T89). The two closed drift paths are contours of constant B which enclose equal amounts of magnetic flux ($\Phi = -2\pi k_p/L^*R_E$). The value of B for each contour is given in parentheses following the Kp label at the top of the figure. As the magnetic field evolves from the $Kp=1$ towards the $Kp=5$ configuration, the magnetic field becomes more depressed in the inner region, and the drift shell must expand outward to conserve the magnetic flux enclosed within it. The asterisk on the $Kp=5$ drift shell marks the approximate position of CRRES at a particular point during orbit 185 ($r=4 R_E$, $MLT=3$ hr).

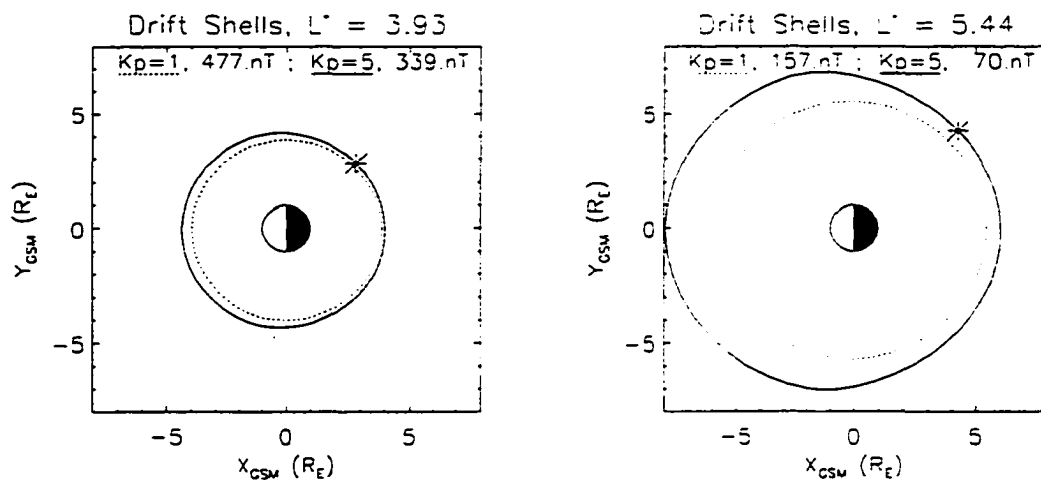


Figure 13.2 : Equatorial drift shells for (a) $L^*=3.93$; and (b) $L^*=5.44$.

Figure 13.2b is analogous to Figure 13.2a, but shows the drift shell with $L^*=5.44$. The azimuthal asymmetry of the field is clearly evident in the distorted drift shell, particularly for the $Kp=5$ case where the drift shell extends to $r=6 R_E$ along the midnight meridian

and to nearly $8 R_E$ along the noon meridian. In comparison to Figure 13.2a, it is obvious that variations in the external field become more significant at larger radius. The approximate position CRRES at a point during orbit 185 ($r=6.0 R_E$, $MLT=3$ hr) is marked on the $K_p=5$ contour with an asterisk.

As K_p increases from $K_p=1$ to 5, a detector positioned at the asterisk (in Figure 13.2b, $r=6.0 R_E$, $MLT=3$ hr) will begin to sample electrons which were initially closer to the Earth and in a stronger B field. These electrons will lose energy as they move into the weaker B field (while conserving μ , $J=0$, and L^*). The question to be answered at this point is, "How will the flux spectrum $j(E)$ being sampled at this fixed point evolve adiabatically?" This question may be answered assuming that the quiet time spectrum is known as a function of r (at fixed MLT) and that it is known how the magnetic field evolves. Using Liouville's theorem and the relation $f=j/p^2$, one may then relate the initial $j(E)$ to the final $j(E)$.

In describing the algorithm followed for this calculation, the following notation will be used. The subscript 1 or 5 refers to the K_p which specifies the field configuration. The flux distribution for $K_p=1$ will thus be $j_1(E,r)$; and for $K_p=5$, $j_5(E,r)$. The subscript a designates the shell (identified by the fixed position $r=r_a$, $MLT=3$ hr, $MLAT=0^\circ$) on which the comparison of spectra is to be made. Thus the magnetic field of shell a will be given as B_a . The subscript b designates the shell (identified by the fixed position $r=r_b$, $MLT=3$ hr, $MLAT=0^\circ$) which is to be adiabatically transformed into the shell designated as a . The following sequence of steps is followed for four different radii at which the modeled and observed spectrum for orbit 185 will be compared.

Algorithm followed for determining adiabatically transformed spectrum:

1. Fix radius at $r_a = 4.5, 5.0, 5.5, 6.0 R_E$
2. Fix energy at E_a
3. For fixed r_a , determine B_a from Kp=5 T89 model. B_a contour defines drift shell a .
4. Determine L_a^* for drift shell a .
5. From E_a , calculate $p_a^2 = (\gamma^2 - 1)E_0^2/c^2$, where $\gamma = (E_a + E_0)/E_0$ and E_0 is the electron rest energy.
6. Calculate $\mu_a = p_a^2 / (2mB_a)$
7. Using Kp=1 T89 model, guess an initial value of r_b at MLT=3 hr ; determine B_b and trace out drift shell b . Determine L_b^* . Iterate in radius r_b until $L_b^* = L_a^* = L^*$. Save final iterated value of r_b and B_b .
8. Assuming conservation of μ ($\mu_a = \mu_b = \mu$), and using the new B_b (from step 7), determine a new $p_b^2 = 2\mu m B_b$, and $E_b = (p_b^2 c^2 + E_0^2)^{1/2} - E_0$.
9. Use Liouville's theorem : $f_1(\mu, L^*) = f_2(\mu, L^*)$ and $f = j/p^2$, to get $j_1(E_b, r_b) / p_b^2 = j_2(E_a, r_a) / p_a^2$, or, $j_2(E_a, r_a) = j_1(E_b, r_b) [p_a / p_b]^2$.
10. Return to step 2; increment to next E until a complete spectrum is constructed.
11. When complete spectrum constructed for given r_a , return to step 1 and increment in radius for next spectrum.

Thus, given the Kp=1 spectrum from orbit 182, j_1 , the adiabatically transformed Kp=5 spectrum for orbit 185, j_2 , may be determined. The comparison between $j_2(E_a, r_a)$ and $j_1(E_a, r_a)$ can then be made, where $j_2(E_a, r_a)$ gives flux at energy E_a on position a under Kp=5 conditions (orbit 185), and $j_1(E_a, r_a)$ gives the flux at the same energy and at the same position a under Kp=1 conditions (orbit 182). The comparison shows the extent to which adiabatic variations cause a flux decrease at the fixed position a .

Figures 13.3(a,b) show the results of adiabatically transforming orbit 182 ($Kp=1$) spectra to orbit 185 ($Kp=5$) spectra. Figure 13.3a are the results from using the T89 model for calculating L^* (B is not known globally), and CRRES B measurements for calculating $\mu=p^2/2mB$ (B need only be known locally). Figure 13.3b are the results from using the T89 model for calculating both L^* (tracing out drift shells) as well as calculating $\mu=p^2/2mB$. Each figure includes four separate panels showing spectra at different radii ($r = 4.5, 5.0, 5.5,$ and $6.0 R_E$). The symbol key in the top left panel of each figure labels three spectra: the CRRES spectrum for orbit 182 (square), the CRRES spectrum for orbit 185 (triangle), and the theoretical spectrum for orbit 185 which was adiabatically transformed from an orbit 182 spectrum at a smaller radius.

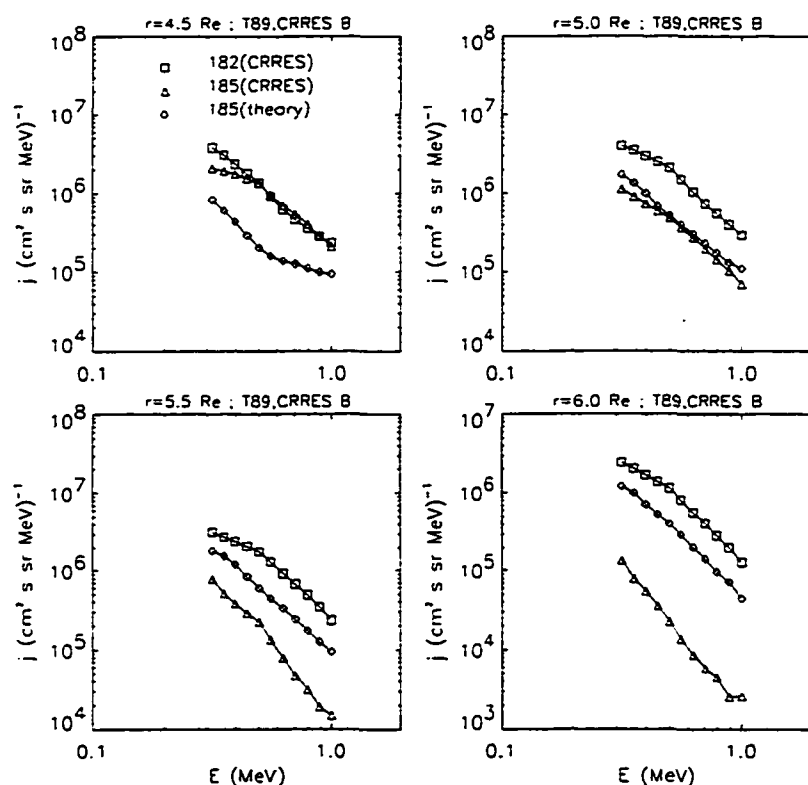


Figure 13.3a : Comparison of observed and adiabatically transformed spectra, using CRRES and T89 B.

For the two energy channels (0.5 and 1.2 MeV) shown in Figure 13.1, electron fluxes observed during orbits 182 and 185 are approximately equal at $r=4.5 R_E$. Above $4.5 R_E$ the ratio of orbit 185 fluxes to orbit 182 fluxes decreases with increasing radius. This trend is seen in the observed spectra for orbits 182 and 185 shown in Figures 13.3a and 13.3b (up to a factor of ~ 70 decrease at the high end of the spectrum is observed at $r=6 R_E$). In both Figures 13.3a and 13.3b, the largest predicted adiabatic flux decrease between orbit 182 and 185 is seen at $r=4.5 R_E$ (factor of ~ 6 decrease in Figure 13.3a and a factor of ~ 10 decrease in Figure 13.3b). The predicted adiabatic flux decreases at the larger radii are somewhat smaller (factor of ~ 3 decrease in Figure 13.3a and a factor of ~ 7 decrease in Figure 13.3b). The results shown in Figure 13.3a are expected to be more

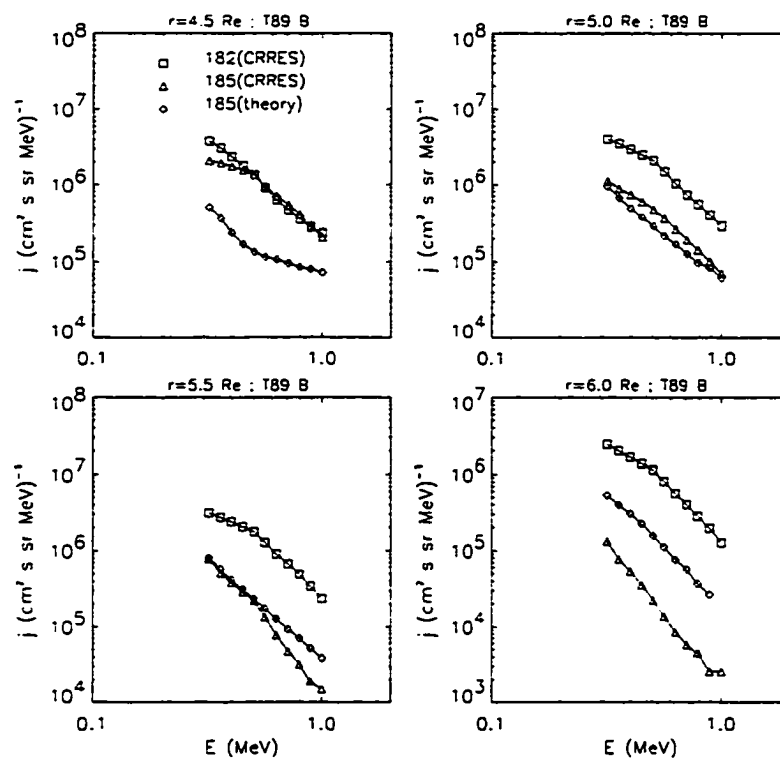


Figure 13.3a : Comparison of observed and adiabatically transformed spectra, using T89 B only..

accurate than those in Figure 13.3b, particularly at larger radius, since the measured B is used to calculate μ and the model B decreases in accuracy at larger radius.

Within the accuracy of T89, the adiabatic transformation predicts too large a flux decrease at small radius, and not enough of a decrease at large radius. At $r=6.0 R_E$, it is estimated that less than 10% of the flux decrease may be attributed to purely adiabatic variation. At $r=4.5 R_E$, an adiabatic flux decrease by a factor of ~ 6 is predicted but not observed. For some intermediate radii the agreement between theory and observation is reasonable. As discussed in Chapter 11.1, the T89 model showed superior overall agreement with observations as compared to the Hilmer-Voigt and Olson-Pfitzer field models, and significant improvement in modeling the adiabatic effect with alternate magnetic field models is not anticipated in the near future.

13.2 Evidence for Non-Adiabatic Flux Losses

The LANL geosynchronous data discussed in Chapter 10.1 indicated that flux losses at all energies (by up to a factor of ~ 10) during the pre-SSC period may be attributed to magnetopause shadowing, representing a real loss of electrons from the magnetosphere. Of course, magnetopause shadowing need not be restricted to the pre-SSC period, but may contribute to a significant loss of electrons throughout the main phase, as long as the stand off distance maintains its pre-SSC value of $R_s \approx 7.5 R_E$ which it does through most of the storm main phase.

One by-product of magnetopause shadowing is the formation of 'butterfly' (after their shape in a velocity space plot) pitch angle distributions [West, 1979]. As a result of

'L-shell splitting' [Stone, 1963; Roederer, 1967], electrons with a pitch angle (α) of 90° will azimuthally drift further out on the dayside than electrons with lower pitch angles. Thus, in the course of their eastward drift about the Earth, the higher pitch angle electrons are more likely to encounter the magnetopause than the lower pitch angle electrons. If a satellite is in the position to sample the electron drift shells which have been depleted of the higher pitch angle population, it will observe a pitch angle distribution which has a local minimum at 90° . An example of such a 'butterfly' pitch angle distributions observed by CRRES following the SSC is shown in Figure 13.4.

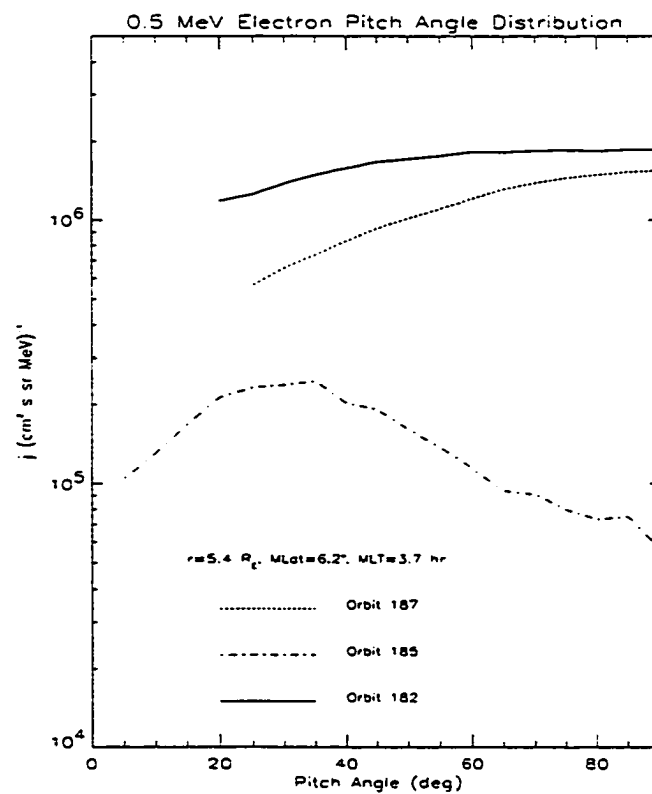


Figure 13.4 : Observed 'butterfly' pitch angle distribution following the SSC (orbit 185).

The differential flux of 0.5 MeV electrons is plotted versus pitch angle for intervals during the quiet pre-SSC period (orbit 182, solid curve), following the SSC (orbit 185, dash-dot curve), and following the injection (orbit 187, dot curve). These pitch angle distributions were all observed near 6° magnetic latitude at a radius $\sim 5.4 R_E$ and a magnetic local time of 3.7 hrs. Following the SSC, the electron flux at $\alpha \sim 90^\circ$ decreased by a factor of ~ 30 , and at $\alpha \sim 30^\circ$, by a factor of ~ 6 . This preferential loss at $\alpha \sim 90^\circ$ is evidence for the non-adiabatic 'magnetopause shadowing' loss mechanism.

For a more in depth analysis of the storm dynamics of the outer radiation electrons, which involves adiabatic and non-adiabatic variations, it is necessary to resort to the time evolution of phase space density at fixed adiabatic invariants (μ, J, L^*). This task is taken up in the following chapter.

CHAPTER 14

STORM DYNAMICS

14.0 Introduction

As discussed in the preceding chapter on adiabatic variations, there is clear evidence that there are nonadiabatic as well as adiabatic processes taking place throughout the storm interval under study here. In this chapter, the role which radial diffusion may play throughout the storm is examined. Radial diffusion studies have typically focused on the time period following a storm, after an impulsive process has elevated the intensity of energetic electrons deep within the trapping region and the magnetosphere has begun its gradual approach towards equilibrium [*Newkirk and Walt, 1968; Lanzerotti, et al., 1970; Lyons and Williams, 1975; West, et al., 1981; Bourdarie, et al., 1996; Selesnick, et al., 1997*]. In these cases, time (magnetic activity) independent diffusion coefficients were either derived from the radiation belt electrons, or used for modeling them.

Here, for the first time to my knowledge, time dependent radial diffusion coefficients and time dependent outer boundary conditions are used to model the radial diffusion of the radiation belt electrons through all phases of a magnetic storm.

14.1 Phase Space Density Survey

Radiation belt diffusion analysis requires that particle fluxes be transformed to phase space density (as described in Chapter 12), and this has been done for the 25 orbits of CRRES electron data spanning the storm period of interest. To limit the scope of this study, a large part of the analysis will be restricted to a single value of the second invariant ($J=1.78 \cdot 10^{-16} R_E \text{ g cm/s}$). Examination of Figure 12.3 shows that at this fixed J , the equatorial pitch angle varies between $30\text{-}50^\circ$. From Figure 12.4, it can be seen that for $\mu=100 \text{ MeV/G}$, the electron energy ranges from $\sim 0.27 \text{ MeV}$ (at $L=5.5$) to 0.8 MeV (at $L=3.5$). For 1000 MeV/G , the range is from 0.7 MeV (at $L=5.5$) to 1.5 MeV (at $L=4.5$). Considering the problems with saturation at the lowest energy channels and background at the highest energy channels, this span of μ represents the maximum coverage of electron measurements for this L^* range.

Figure 14.1 is a color coded 'snapshot' of the storm time phase space density $f[\text{s}^3/\text{km}^6]$ variations at fixed J ($1.78 \cdot 10^{-16} R_E \text{ g cm/s}$) and fixed μ (top to bottom panel, respectively: 100, 316, and 1000 MeV/G). L^* is scaled along the y-axis ($L^* = 3$ to 6) and orbit number (180 to 204) is scaled along the x-axis. The $f(L^*)$ profile for each leg (ascending and descending) of an orbit is plotted individually as a vertical color bar. It is evident that the coverage at low L^* is most complete for the 100 MeV/G electrons, with increasingly sparse L^* coverage at the higher μ due to the upper limit of the energy channels. Aside from these energy limitations, the most complete coverage is from those orbits which traverse the outer belt within 10° of the magnetic equator, and thus sample the equatorial pitch angle distribution most completely. A convention followed in the

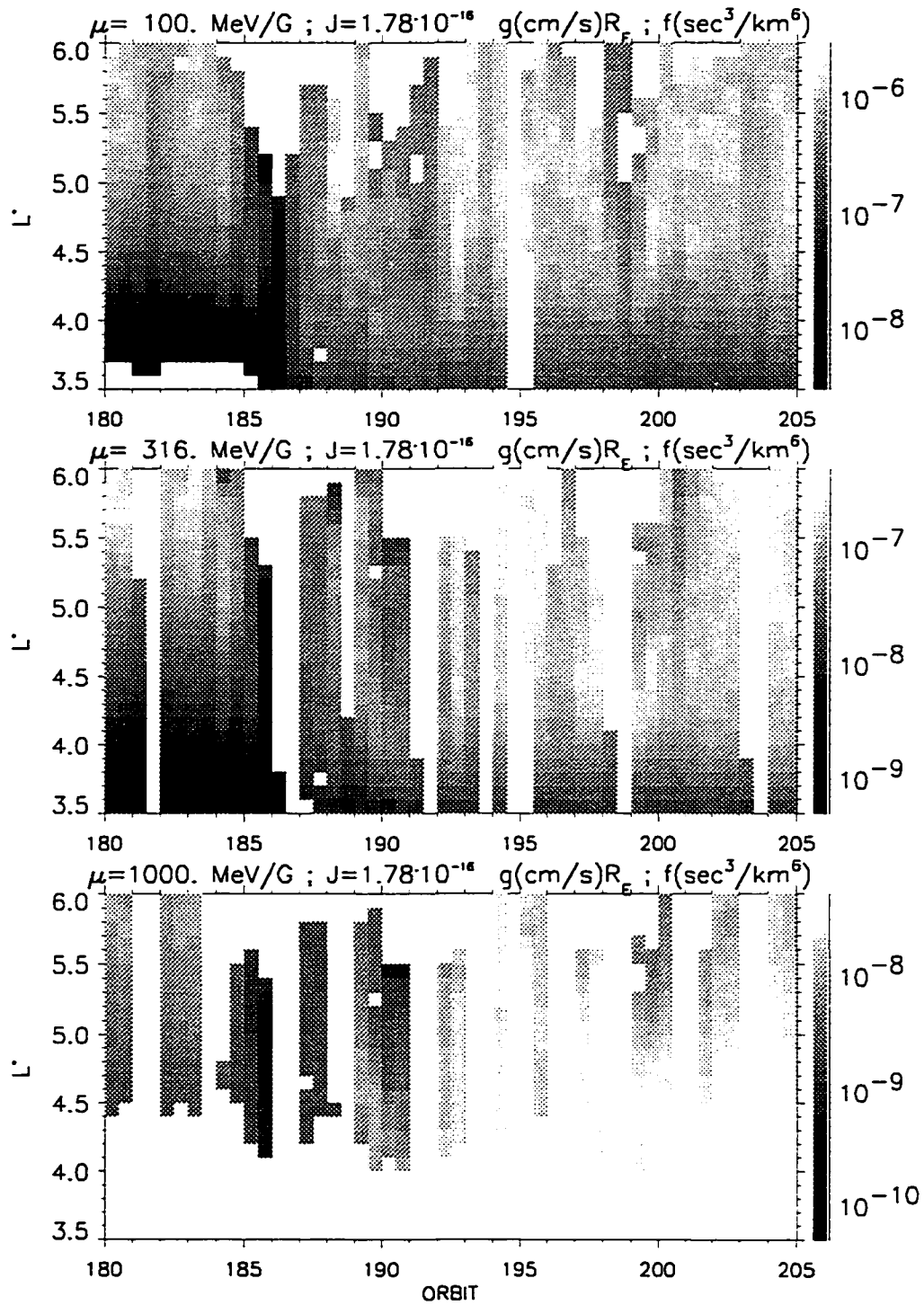


Figure 14.1: Survey of phase space density.

discussion below uses fractional orbit numbers to identify individual legs of an orbit (i.e., orbit 180.0 refers to the ascending leg and 180.5, the descending leg).

Orbits 180.0 to 183.5 are during the quiet period before the SSC. The $f(L^*)$ profile is quite stable during this time, and monotonically increases from low to high L values for all μ , with a steep gradient below $L^*=4.5$ as seen for the lower μ electrons. The SSC occurs during orbit 184.0, and significant decreases in f are observed for all L^* during orbits 184.5-186.0 following the SSC. The extent to which the decrease in flux observed during this period is adiabatic versus non-adiabatic was addressed in the preceding chapter. However, any temporal variation in $f(t)$ at fixed μ , J , and L^* , is by definition a non-adiabatic variation, and is potentially explicable in terms of some combination of diffusive processes. As discussed in Chapter 10.1, an abrupt enhancement (injection) of <0.5 MeV electrons was observed at apogee during orbit 186.5, and by orbit 187.0 $f(\mu=100 \text{ MeV/G}, L^*<4)$ has increased by a factor of ~ 10 over its pre-injection value. The rate of increase in $f(t)$ following the dropout decreases with increasing μ . By orbit 192, $f(t)$ has nearly reached its maximum for all μ , and from that point on, the magnetosphere appears to have stabilized at a fairly constant f , which for $L^*>5.6$, is approximately equal to that during the pre-SSC period, even for $\mu=1000$ MeV/G.

Although the radial diffusion will be modeled at a single value of the second invariant ($J=1.78 \cdot 10^{-16} R_E g \text{ cm/s}$), Figure 14.2 is included to show that there are differences in seen at different J for a given μ . In this figure, f is plotted versus orbit at three fixed values of μ (100, 316, and 1000 MeV/G, for top to bottom panels) and at a

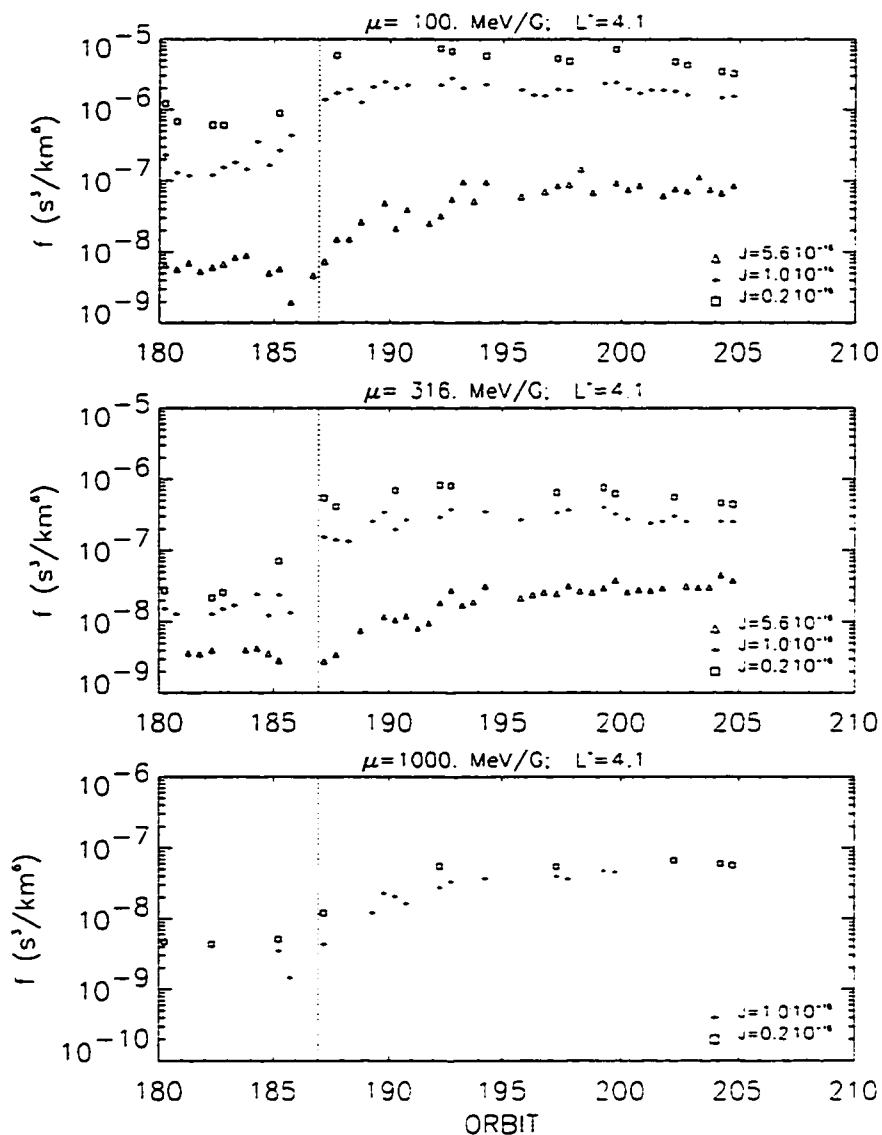


Figure 14.2 : J dependence of $f(\mu, J, L^*)$.

fixed $L^*=4.1 R_E$. For each value of μ , f is plotted for three values of J ($0.2 \cdot 10^{-16}$, 10^{-16} , and $5.6 \cdot 10^{-16} R_E g \text{ cm/s}$) which are labeled by the symbol key in the lower right corner. A vertical line is drawn at orbit 187.0 as a reference to the first post-injection orbit. The correspondence between J and pitch angle (α) may be approximated from Figure 12.3,

and varies with μ . For the range of J 's shown in Figure 14.2, α ranges from 20° - 60° (high to low J) for $\mu=100$ MeV/G ; from 35° - 70° (high to low J) for $\mu=316$ MeV/G ; and up 80° (low J) for $\mu=1000$ MeV/G (where data for low α becomes very limited). One important point shown here is that the electrons (for $\mu=100$ and 316 MeV/G) with the lowest J (largest α), which are most closely confined to the magnetic equator, respond most quickly to the injection. These electrons reach their maximum f almost immediately following the injection, and then remain at these levels, or proceed to decay slightly. The electrons with the highest J (smallest α), which are mirroring farthest down the field line, show a much more gradual increase (even while the more equatorial electrons are decaying). These trends seen for electrons at different α will be discussed in the following chapter.

14.2 Time Dependent D_{LL}

Before discussing the details of the radial diffusion modeling itself, the time dependence of D_{LL} needs to be addressed. In the early years of radial diffusion research [*Kellogg*, 1960; *Parker*, 1960; *Davis and Chang*, 1962; and *Nakada and Mead*, 1965] the isolated SSC was considered to be the primary driver of radial diffusion. A meaningful time scale for the diffusion process was thus measured in terms of the months over which a statistically significant number of SSCs occurred and could be averaged over. Consequently, early research fostered the notion of a single average diffusion coefficient, $D_{LL}(L)$, which was relevant for a long term steady state solution. However, once *Falthammer* [1965] developed the theoretical tools for evaluating time dependent

D_{LL}^E and D_{LL}^M from general power spectra, the relevant time scale was no longer the weeks to months between SSCs, but hours. The time dependent D_{LL}^E and D_{LL}^M used in the following radial diffusion analysis, with $D_{LL} = D_{LL}^E + D_{LL}^M$, are elaborated upon below.

Time Dependent D_{LL}^E

As first suggested in Chapter 7.4, assuming a K_p dependence of the root mean square electric field, $E_{rms}(K_p)$, enables one to write *Cornwall's* [1968] form of the radial diffusion coefficient (Equation 7.26) as a function of K_p :

$$D_{LL}^E(K_p) = \frac{1}{4} \left(\frac{cE_{rms}(K_p)}{B} \right)^2 \left[\frac{T}{1 + (\omega_D T / 2)^2} \right] \quad (14.1)$$

An explicit relation $E_{rms} = E_{rms}(K_p)$ may be inferred from the CRRES electric field measurements and is discussed next.

In Chapter 10.2, the electric field was surveyed for several sample orbits through out the storm (Figure 10.6). That survey provides support for the claim that $E_{rms} = E_{rms}(K_p)$, but this dependence must be quantified for Equation 14.1. *Rowland and Wygant* [1997] performed a statistical study on the K_p dependence of the large scale DC convection electric field. The dawn-to-dusk convection electric field is given by the y-component of E in geocentric solar ecliptic (GSE) coordinates (Appendix A). Because CRRES did not always point exactly towards the sun, a modified GSE coordinate (mGSE) was used to specify the electric field components. Using the same CRRES electric field data set as used for Figure 10.6, Rowland and Wygant binned and averaged

10 months (orbits 408-944) of E_y (mGSE) in an $L \times Kp$ grid. Their results are displayed in Figure 14.3 (adapted from *Rowland and Wygant [1997]*) where E_y is plotted versus L (not L^*) for the five Kp ranges identified by the key in the upper left hand corner. For a given Kp , E_y increases rapidly from $L=2$ to some characteristic L_0 , above which, it remains relatively constant. The L_0 is Kp dependent and moves to lower L for increasing Kp , indicating that the convection electric field penetrates to lower L as magnetic activity increases.

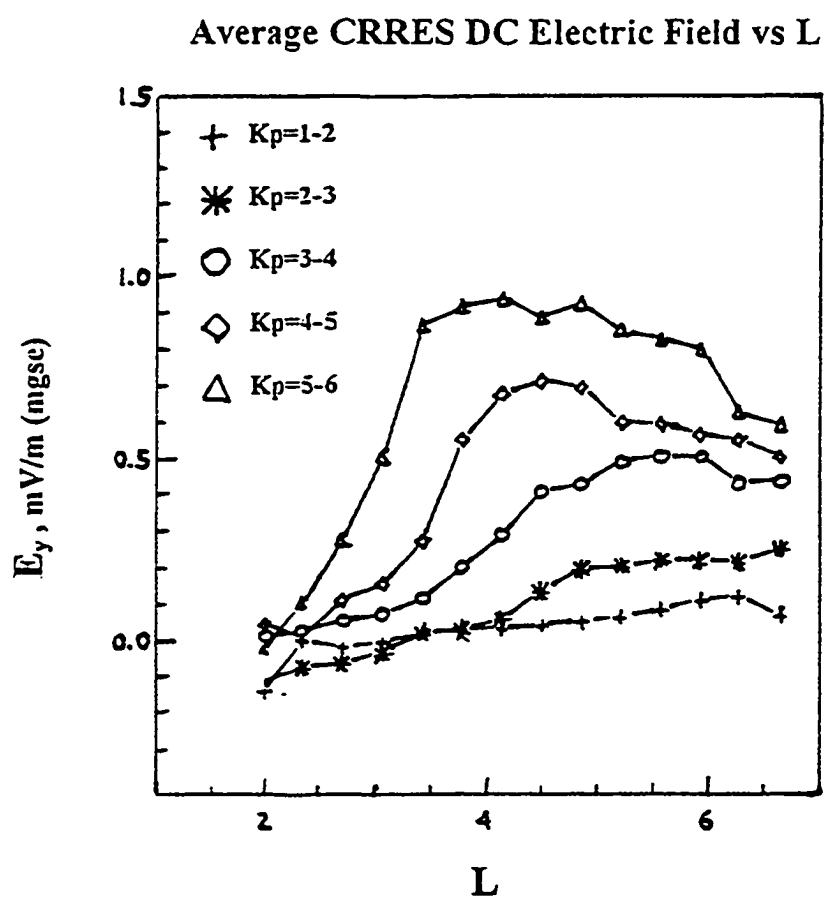


Figure 14.3 : DC convection electric field dependence on L for $Kp=1$ to 6 [Rowland and Wygant, 1997].

The average E_y for $L=3.5-6$ is plotted (filled rectangles) versus K_p in Figure 14.4 and shows that E_y linearly increases with K_p for $K_p > 2$, with $E_y = 0.225(K_p - 1) - 0.075$.

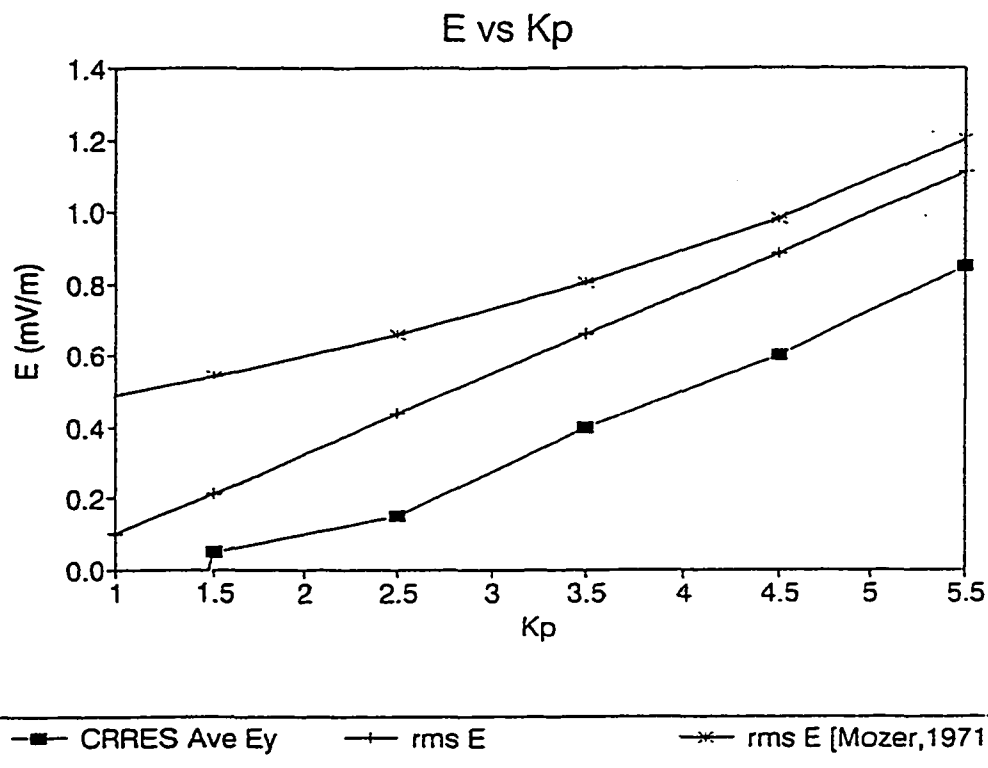


Figure 14.4 : Average E_{rms} as a function of K_p .

The standard deviations about each calculated average are comparable to or greater than (particularly so at the higher K_p levels) that average (private communication, Wygant, 1997). Since this standard deviation is a measure of the fluctuation about a mean E_y , it provides an estimate for the rms value of $E(K_p)$. Since the E_y averages were determined from 10 months of data they are taken to be a lower limit of what may be considered a representative value of E_{rms} for a single storm period (as being studied here). With this in mind, the linear relation for E_y is assumed for E_{rms} , but is scaled up so that $E_{rms}(K_p=1)$

=0.1 mV/m. This linear relationship for $E_{rms}(Kp)$ is given below, and is also plotted ('+' symbols) in Figure 14.4.

$$E_{rms}(Kp) = 0.225(Kp-1) + 0.1 \text{ mV/m, for } Kp=1,6 \quad (14.2)$$

The $E_{rms} = 0.1$ mV/m is used by *Lyons and Thorne* [1973] in their quiet time steady state solution where D_{LL} is defined by Equation 14.1, and it is also consistent with the amplitudes observed for orbits 182-183 in Figure 10.6. For higher magnetic activity, this relation gives $E_{rms}(Kp=5) = 1.0$ mV/m (2.8 mV/m peak to peak) which is in line with the amplitudes observed for orbits 186, 189, and 190.

A second empirically determined form of $E_{rms} = E_{rms}(Kp)$ was found from balloon-based measurements of ionospheric electric fields which were mapped back to the equator [*Mozer*, 1971]. *Mozer* analyzed more than 200 power spectra representing ~700 hours of electric field measurements taken at a range of latitudes corresponding to an L range of 2.8 to 23. He found that a single component of the equatorial E_{rms} , for $3 < L < 8$, could be expressed as a function of Kp, independently of magnetic latitude and L as:

$$E_{rms} = 0.4 \exp(0.2 Kp) \text{ mV/m} \quad (14.3)$$

This relation is also plotted in Figure 14.4 ('x' symbols) and may be compared to the estimate of the single component (E_y , mGSE) of the averaged CRRES E_{rms} fields. At low Kp, *Mozer's* values are 2 to 5 times higher than CRRES estimates, but approach to within ~10% at high Kp.

Since Equation 14.2 is based upon CRRES measurements at high altitudes (thus avoiding the problem of mapping ionospheric fields) and is more consistent with observed amplitudes (Figure 10.6) at low Kp, it is used in Equation 14.1 to calculate D_{LL}

for the time dependent radial diffusion analysis in this chapter. $D_{LL}^E(L, Kp=1 \text{ to } 6)$ is calculated for $\mu=100 \text{ MeV/G}$ and is plotted versus L in Figure 14.5. The symbol key in the upper left labels the coded lines with the corresponding Kp (1-6) and E_{rms} (0.1-1.23 mV/m) values.

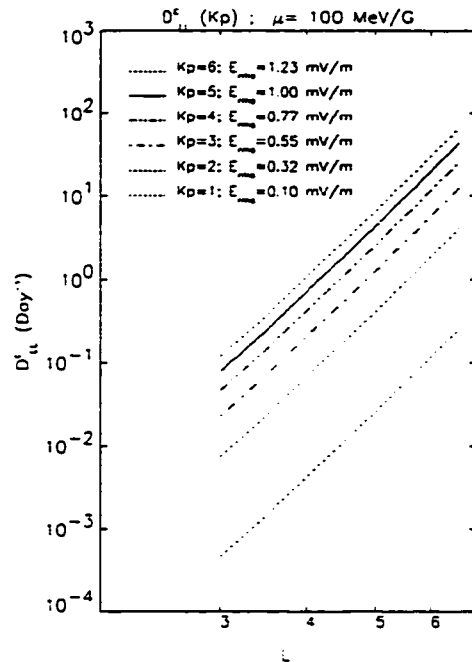


Figure 14.5 : D_{LL}^E as a function of L and Kp .

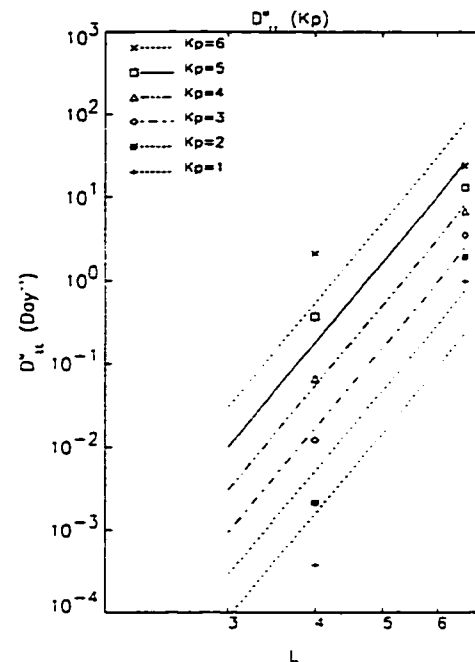


Figure 14.6 : D_{LL}^M as a function of L and Kp .

Time Dependent D_{LL}^M

As discussed in Chapter 7.4, Kp dependent $D_{LL}^M (= D_0 L^{10})$ were determined at $L=4$ [Lanzerotti and Morgan, 1973] and at $L=6.6$ [Lanzerotti, et al., 1978] from both the local day and night sectors. An average of the daytime and nighttime values were used at $L=4$, but only the daytime values were used at $L=6.6$. In Figure 7.7 these point (at single L) determinations of D_{LL}^M are extrapolated throughout the range $L=3$ to 6.6 using the assumed L^{10} dependence. However, the extrapolations from the two points are

not well aligned and give a double-valued D_{LL}^M as a function of L . To rectify this situation, the local night time results were averaged in with the local day time results for $L=6.6$. This procedure was motivated by the work of *Lanzerotti and Wolfe* [1980] discussed in Section 7.4, and brings the results for $L=4$ and $L=6.6$ into better agreement with the L^{10} dependence. $D_o(L=4)$ and $D_o(L=6.6)$ were iteratively adjusted to a single D'_o to minimize the differences between the point values (at $L=4, 6.6$) and $D_{LL}^M = D'_o L^{10}$. This 'hybrid' result from the two individual studies by Lanzerotti and coworkers, is shown in Figure 14.6, where the adjusted $D_{LL}^M(Kp)$ is plotted versus L . The values of the new D'_o , for $Kp=1-6$, are $1.5 \cdot 10^{-9}$, $4.9 \cdot 10^{-9}$, $1.6 \cdot 10^{-8}$, $5.2 \cdot 10^{-8}$, $1.7 \cdot 10^{-7}$, $5.1 \cdot 10^{-7}$, respectively. The symbol key in the upper left of the figure associates a Kp value with a line style for the extrapolated results, and with a symbol for the individual results at $L=4$ and 6.6 . The best agreement between $D_{LL}^M = D'_o L^{10}$ and the individual point results occurs for $Kp=4$ which is nearly exact; the worst agreement is for $Kp=1$ where there is a factor of 6 difference.

14.3 Radial Diffusion Modeling: Algorithm

In this analysis, it will be assumed that radial diffusion proceeds at constant first and second invariants. The radial diffusion equation to be modeled (introduced as Equation 7.21 and reproduced below for convenient reference) is a one dimensional (in the third invariant L) parabolic partial differential equation:

$$\frac{\partial f}{\partial t} = L^2 \frac{\partial}{\partial L} \left[D_{LL} L^{-2} \frac{\partial f}{\partial L} \right] - \frac{f}{\tau}. \quad (14.4)$$

In Equation 14.4, and in the discussion which follows, the parameter L is taken to be synonymous with L^* , but is dropped for convenience of notation. This partial differential equation may be numerically solved using standard finite differencing techniques [Press, *et al.*, 1998]. Assuming a discrete grid in L and t , with a finite step size (resolution) of ΔL and Δt , the above equation may be solved by expressing the derivatives as finite differences. Rewritten within this finite difference scheme, the partial differential equation is expressed as a system of linear equations of the form: $\mathbf{A} \bullet \mathbf{X} = \mathbf{X}'$, where \mathbf{A} is a tridiagonal matrix which is a function of step sizes (ΔL and Δt) and dynamic parameters (D_{LL} and τ). \mathbf{X}' is an array containing values of phase space density, f , at different points along the L grid at a fixed time, t , and \mathbf{X} is the array to be solved for, with values of f at a later time, $t + \Delta t$. Thus, presented with an initial distribution $f(L, t=0)$, the diffusion algorithm propagates the distribution $f(L, t)$ forward in time in fixed time steps. The matrix \mathbf{A} controls the dynamics and must be updated in time for the case of a time dependent D_{LL} . A flowchart summarizing this radial diffusion algorithm is given in Appendix B.

14.4 Radial Diffusion Modeling: Parameterization

The diffusion coefficient $D_{LL}(Kp) = D_{LL}^E(Kp) + D_{LL}^M(Kp)$ used are displayed in Figures 14.5 (D_{LL}^E) and 14.6 (D_{LL}^M). In this study, the Kp to be used is an average over individual legs of an orbit (~5 hour). Since Kp is published as eight 3-hour indices per day, each Kp value is represented as 3 equal 1-hour indices for purposes of calculating

the 5-hour averages. Over the course of the 10-day storm period, the average K_p varies from 0.2 to 5.8 (3-hour K_p varies from 0 to 6).

The electron decay lifetimes, $\tau(L, \mu)$, to be used here are those used by *Lyons, et al.* [1972] and were calculated using a whistler wave amplitude of $B = 35$ pT. These lifetimes were shown in Figure 7.2a and 7.2b as a function of energy and L . They are plotted in Figure 14.7 as a function of L for $\mu=100, 200, 316, 501, 794,$ and 1000 MeV/G. The loss process due to pitch angle scattering is confined to within the

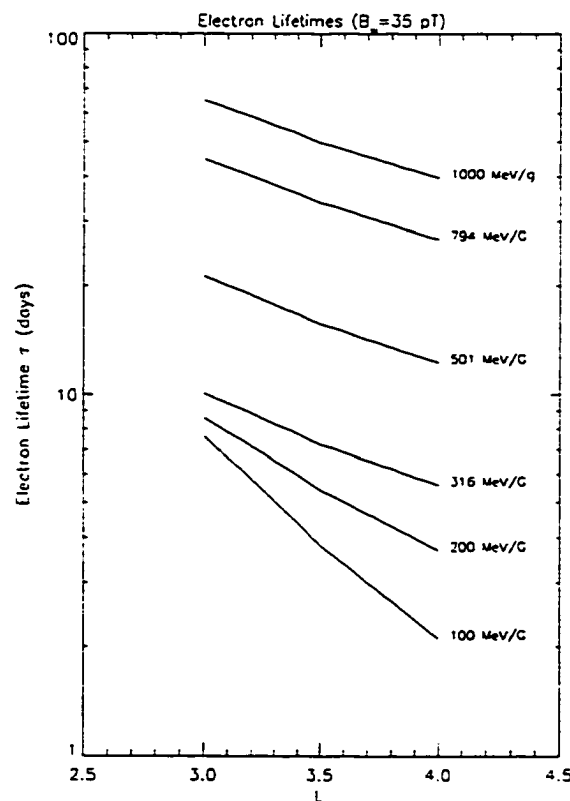


Figure 14.7 : Electron lifetimes versus L for $\mu = 100-1000$ MeV/G.

plasmasphere where the relatively high cold plasma density supports the necessary wave-particle-interactions. The lifetimes, as calculated by Lyons, et al., are valid only within

the plasmasphere, which is chosen to be within $L=4$ for this modeling. Within this boundary, τ assumes the values in Figure 14.7, and beyond, τ assumes an effectively infinite lifetime (i.e., no decay). In principle, τ should vary with K_p since the wave activity responsible for the electron loss represented by τ is magnetic activity dependent (as is D_{LL}). However, for lack of complete information on the factors affecting pitch angle diffusion losses (i.e., whistler wave amplitudes, plasma densities), constant lifetimes will be used.

The L grid is defined from $L=3.5$ (L_{\min}) to 6.0 (L_{\max}) in steps of $\Delta L=.05$. The initial array of phase space density values, $f(L,t=0)_{\mu,J}$ is filled with data from the ascending leg of orbit 180, during the magnetically quiet period before the storm. Individual diffusion modeling runs are made for a number of μ values.

The outer boundary condition is varied according to the observed behavior of the geosynchronous ($r=6.6 R_E$) LANL flux data. The energy range of the LANL flux channels plotted in Figure 10.3 correspond to the approximate range of μ being modeled: 225-315 keV (~ 100 MeV/G), 315-500 keV (~ 16 MeV/G), and 750-1100 keV (~ 1000 MeV/G). For each of these energy channels, a time dependent ratio of disturbed to quiet geosynchronous fluxes is defined, $\mathfrak{R}(E,t)_{\text{geo}}$. During the quiet interval leading up to day 281.99 (orbit 184), $\mathfrak{R}_{\text{geo}}=1$ by definition. For the CRRES data, orbit 180 is used as the reference quiet time $f(\mu, L_{\max}, t_0)$ distribution at the outer boundary, and the initial condition for the modeling interval. Making the proper correspondence between E and μ channels noted above, the assumption is made that:

$$\mathfrak{R}(E,t)_{\text{geo}} \approx \mathfrak{R}(\mu, L_{\max}, t) \equiv f(\mu, L_{\max}, t) / f(\mu, L_{\max}, t_0) \quad (14.5)$$

Thus, the time dependent boundary condition for the diffusion problem is specified by:

$$f(\mu, L_{\max}, t) = \mathfrak{R}(\mu, L_{\max}, t) \cdot f(\mu, L_{\max}, t_0) \quad (14.6)$$

Beginning with the initial profile $f(\mu, L, t_0)$ for fixed μ (and J), the diffusion algorithm incrementally evolves the distribution in time steps of $\Delta t = 0.05135$ days. Every four time steps (0.2054 days = time of single orbit leg) the array $f(L)$ is written to a file, and $D_{LL}(t)$ is updated according to $K_p(t)$ and $f(\mu, L_{\max}, t)$ is updated according to Equation 14.6.

14.5 Radial Diffusion Modeling: Results

The results to the radial diffusion modeling are conveyed in the survey plots (orbits 180-204) in Figure 14.8 for $\mu = 100$ MeV/G, $J = 1.78 \cdot 10^{-16}$ g(cm/s) R_E , and Figure 14.9 for $\mu = 1000$ MeV/G, $J = 1.78 \cdot 10^{-16}$ g(cm/s) R_E . The two figures follow identical formats. The top panel shows the variation of $\mathfrak{R}(E, t)_{\text{geo}} \approx \mathfrak{R}(\mu, L_{\max}, t)$ used in specifying the outer boundary condition (Equations 14.5, 14.6). The LANL energy channel used to determine \mathfrak{R} is given in the title heading. The next panel shows the K_p index used to parameterize D_{LL} . The third panel gives the empirical $f(L, t)$ distributions for fixed μ and J (identical to the corresponding panel in Figure 14.1). The bottom panel gives the model $f(L, t)$ distributions.

Figure 14.8, for the lower energy electrons ($\mu = 100$ MeV/G) will be discussed first. The model reproduces the observations for orbits 180 to 183 quite well by virtue of the fact that the model was initialized by the observations of orbit 180, and essentially nothing happened for the first few orbits (very little activity to drive any significant

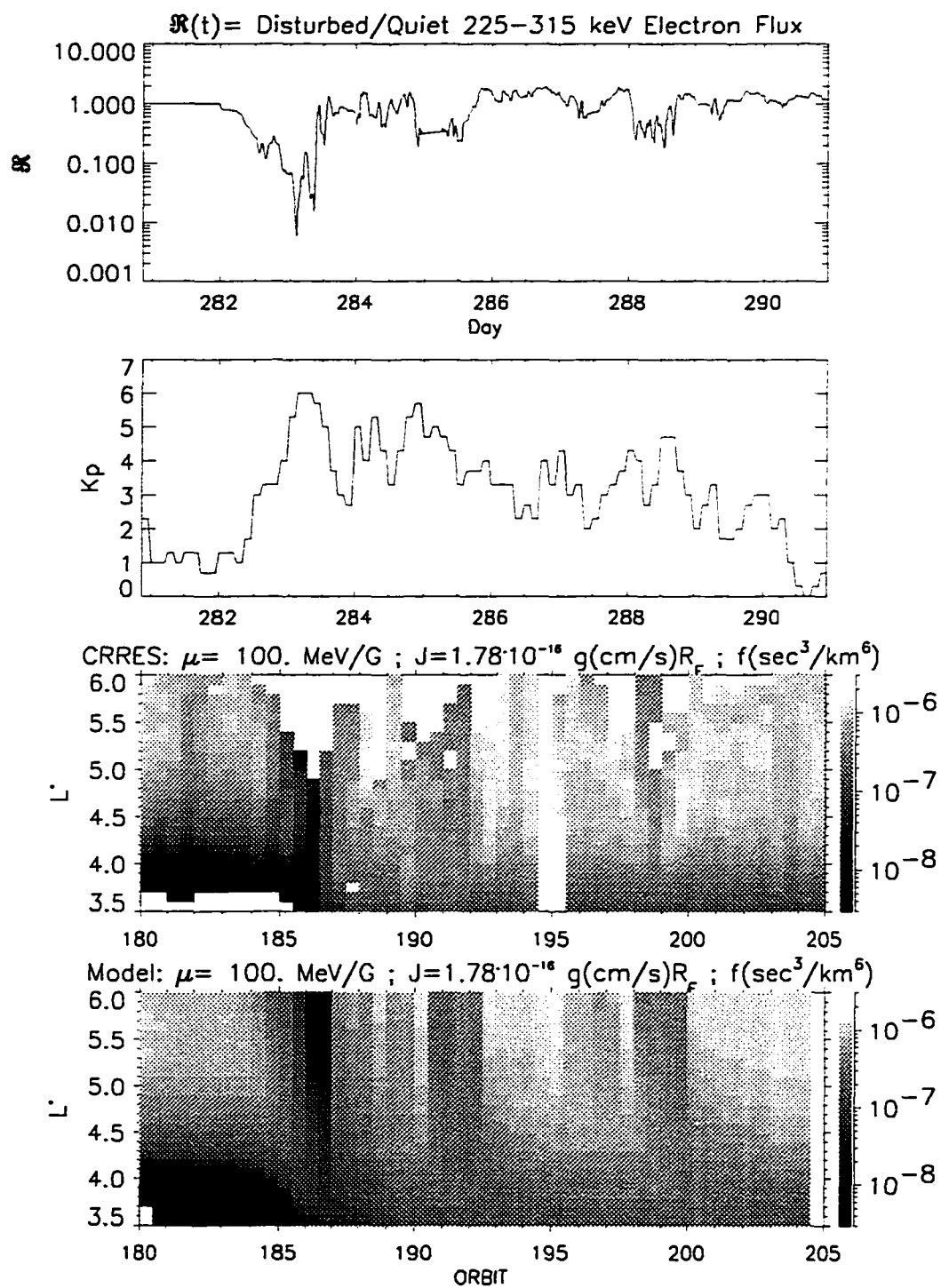


Figure 14.8: Radial diffusion results for $u=100 \text{ MeV/G}$.

diffusion). For orbits beyond 183, when K_p begins to increase and \mathcal{R} begins to drop, it is apparent that the enhanced D_{LL} is quite efficient in translating the variations seen at the outer boundary ($L_{\max}=6.0$) into the inner region. The SSC occurs during orbit 184 and K_p begins to ramp up. As the boundary $f(L_{\max},t)$ begins to decrease (loss of electrons observed at geosynchronous), the outer region of the radiation belt ($L>4.5$) sees a reversal in sign of $\partial f/\partial L$ (positive to negative) such that the increased activity leads to enhanced outward radial diffusion, thus draining electrons from the inner region at an accelerated rate. Unfortunately, the data is sparse at the higher L which precludes a determination of how big a decrease f experiences. The model reflects the onset of the dropout during orbit 184, but does not show as an abrupt and steep decrease in f . The model also underestimates both how far the injection penetrates and the speed of the recovery. By orbit 187.0 (post-injection) the empirical $f(L=3.8)$ has increased by a factor of >10 over its orbit 186.0 (pre-injection) value, whereas there is no discernible change in the modeled result. Above $L=5.5$ the model shows much better agreement throughout the recovery. It is notable that several other observed minor dropouts and recoveries are replicated in the model (best agreement at $L>5$, with lesser agreement towards lower L). The effect of the loss term (τ) can be seen in the modeled f below $L=4$ beginning with orbit ~ 200 , when $f(L=3.9)$ reaches its peak value (in the yellow) of $\sim 5 \cdot 10^{-7}$ (s^3/km^6). From this point on, magnetic activity diminishes ($K_p \leq 3$) and radial diffusion as modeled is weakening. Below $L=4$, the pitch angle diffusion process (loss) associated with τ now begins to dominate the radial diffusion process (source), and $f(L=3.9)$ begins to decrease (yellow to green).

Figure 14.9 conveys the radial diffusion modeling results for $\mu=1000$ MeV/G, and may be compared to the results shown for $\mu=100$ MeV/G in Figure 14.8. The agreement between the theoretical and empirical results at $L>5$ is comparable to that seen at lower μ , and the results for $L<5$ show consistently poorer agreement.

Unfortunately, the sparse empirical data makes comparisons more difficult. The model for the higher μ has the same problems as for the lower μ in terms of accounting for the suddenness and depth of the dropout in f . The longer recovery time is apparent in both the modeled and empirical results, though the missing data precludes a precise assessment. A major difference in the observed response of the low and high energy electrons is seen in the shape of the empirical $f(L)$ profile which evolves throughout the recovery phase. Whereas the empirical f for 100 MeV/G electrons evolves towards a profile consistent with earthward radial diffusion from an external source, f for the 1000 MeV/G electrons does not. The 1000 MeV/G electron profile $f(L,t)$ shows a negative gradient which implies a source within the outer boundary which is producing the higher energy electrons.

This anomalous $f(L)$ profile for the higher energy electrons is seen more clearly in Figures 14.12 and 14.13. Both figures are of identical format, and include four panels, each of which compares various $f(L)$ profiles at a fixed value of μ (100, 200, 501, and 1000 MeV/G, as indicated at the top of each panel). Both figures include the CRRES $f(L)$ profile for orbit 180 as the pre-SSC reference curve (drawn as a solid line and labeled as curve A in the symbol key). In addition, each figure includes both the CRRES $f(L)$ profile (drawn as a dash-dotted curve and labeled as curve C) and the modeled $f(L)$

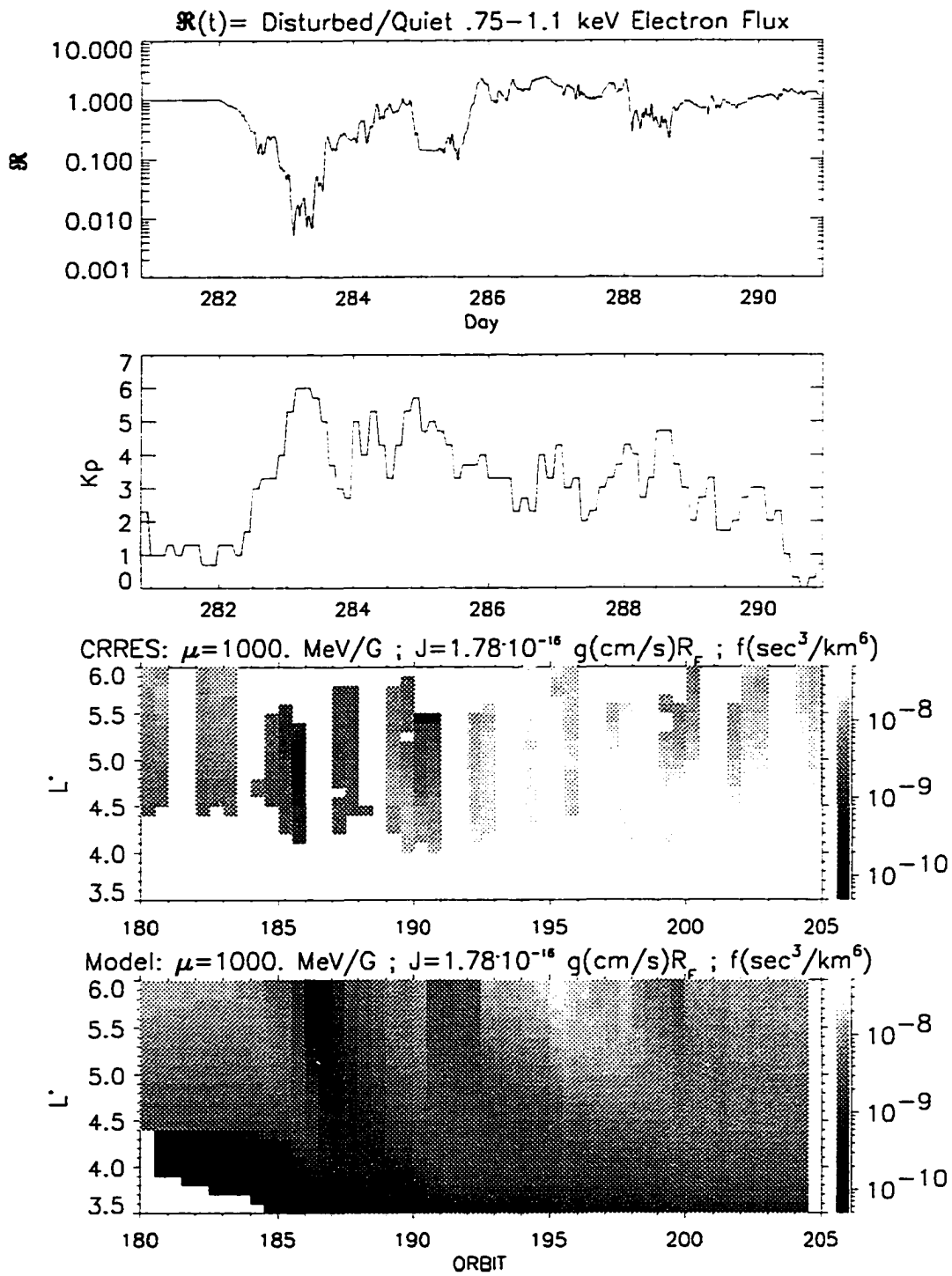


Figure 14.9: Radial diffusion results for $u=1000 \text{ MeV/G}$.

profile (drawn as a dotted curve and labeled as curve B) for a second orbit for comparison.

Figure 14.10 compares the CRRES and modeled curves for orbit 189 (~1 day following the injection), and shows that for the lower μ (top two panels), curves B and C agree within a factor of 2 and exhibit the $f(L)$ profile shape expected for inward radial diffusion from an outer boundary source. This is in sharp contrast to the curves shown for the higher μ (bottom two panels) which clearly show a region where $f(L)$ maintains a negative gradient in L , implying a source within the bounded region.

Figure 14.11 compares the CRRES and modeled curves for orbit 204 (~7.5 days following the injection) and shows that CRRES and modeled $f(L)$ for the low energies is excellent, and the anomalous profiles at the high energies are even more accentuated.

Figure 14.11 shows something further about the effects of the loss term τ . The panels for $\mu=100$ and 200 MeV/G show a kink in the slope of modeled f at $L=4$ (curve C). This is the result of the modeled loss process inside the plasmapause ($L \leq 4$). In the remaining panels, for $\mu > 200$ MeV/G, there is no sign of this slope change. The plot of lifetimes (Figure 14.7) shows that at $L=4$, electrons with $\mu > 700$ MeV/G have a lifetime >5 times that of electrons with $\mu = 200$ MeV/G. That higher energy electrons are more resistant to precipitation losses (i.e., larger τ), is evident in Figure 10.5 which shows the edge of the slot region of the 0.34 MeV electrons (top panel) receding at a much faster rate than that seen at the higher energies.

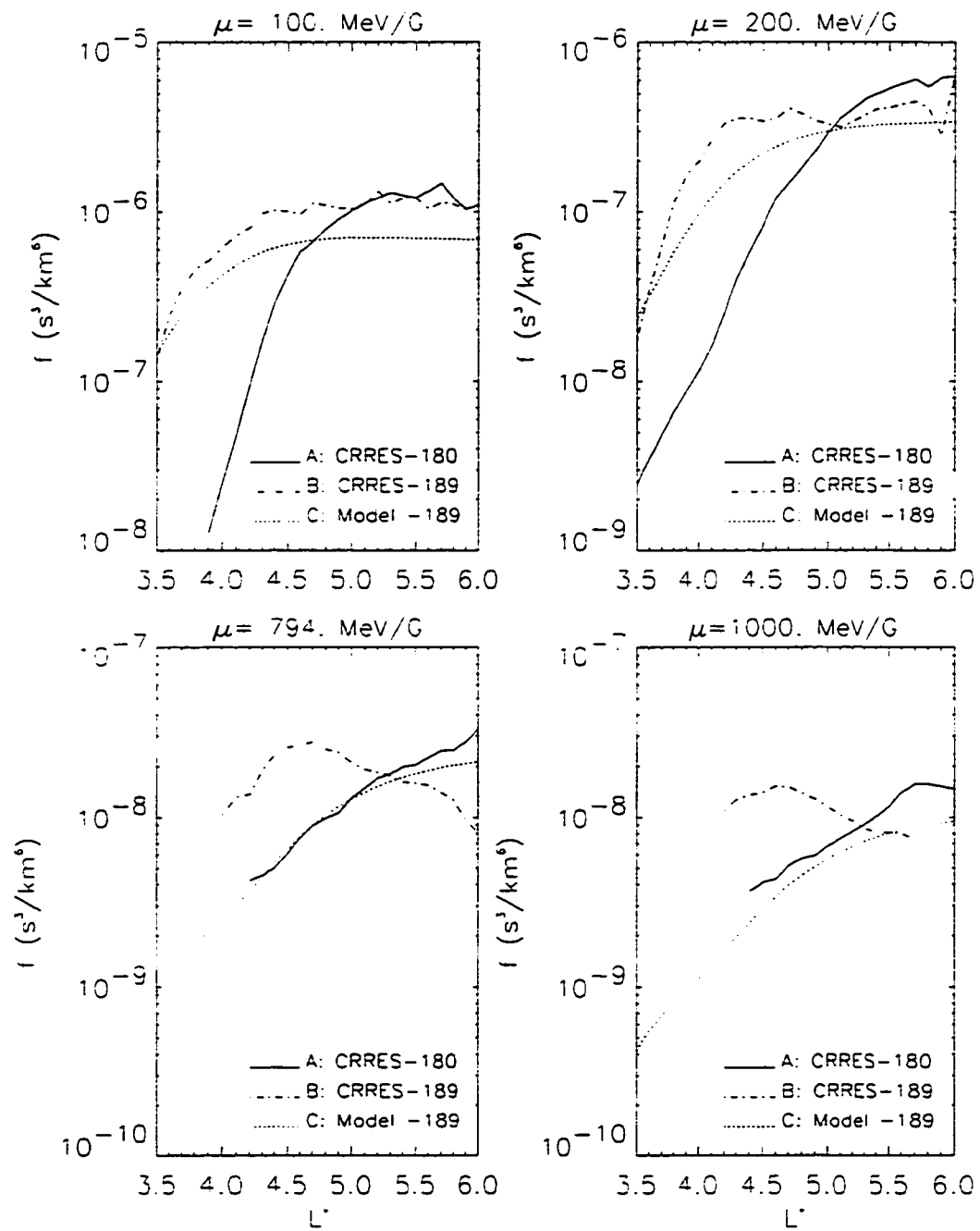


Figure 14.10 : Comparison of empirical and model $f(L)$ for orbit 189.

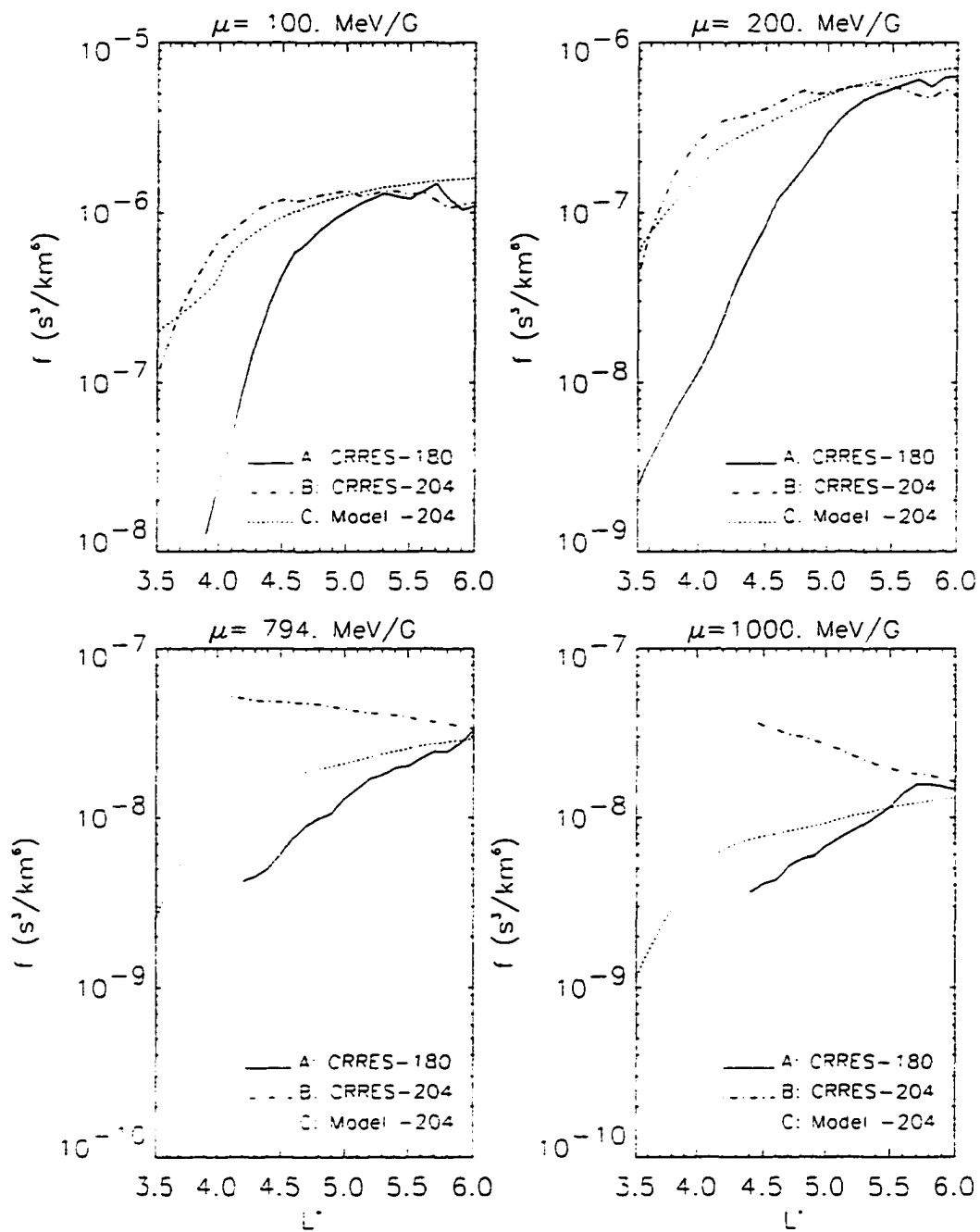


Figure 14.11 : Comparison of empirical and model $f(L)$ for orbit 204.

In summary, the radial diffusion modeling did quite well reproducing the features of the main phase dropout and the recovery phase enhancements (on the time scale of ~ 1 day) for the $\mu=100$ and 200 MeV/G electrons. The best agreement between the empirical and theoretical dynamics was for $L>5$. On the time scale of a single orbit leg (~ 5 hours), the major dropout was underestimated in its abruptness and its loss (at the peak dropout at $L=4$, $f_{\text{model}} / f_{\text{CRRES}} \sim 10$). Also, the enhanced radial diffusion did not bring adequate numbers of electrons in far enough or rapidly enough. The $\mu=1000$ MeV/G electrons (both model and empirical) showed a more gradual recovery relative to the $\mu=100$ MeV/G electrons. For $\mu=1000$ MeV/G electrons, a major discrepancy between the modeled and the empirical $f(L)$ profiles was observed throughout the recovery phase. This discrepancy suggests that another non-adiabatic process is acting as an internal source which, at the higher energies, is dominant over the radial diffusion process being modeled here. This possibility will be discussed in the following chapter.

CHAPTER 15

SUMMARY AND DISCUSSION

15.0 Summary

The preceding chapters have examined in great detail the magnetic storm which commenced on October 9, 1990. Chapter 10 surveyed the well isolated storm and showed it to be a fairly 'typical' storm as described in Chapter 5. The enhanced solar wind pressure during the initial phase of the storm led to a compression of the geomagnetic field which drove Dst to positive values indicating an enhanced field. During the main phase, there was a sustained southward IMF B_z which, it may be inferred, led to an enhanced convection electric field that swept particles of 10s keV into $L^* \sim 4$. This increased ring current depressed the magnetic field and drove Dst down to its minimum. During this time, decreases (by a factor >10) in 0.3 to 1.4 MeV electron flux were observed down to $L^* < 4$. An hour following the onset of the recovery phase, when Dst had begun to recover, an injection of < 0.5 MeV electrons was observed at CRRES apogee. Soon afterwards (within 5 hours) fluxes at these energies were increased dramatically in the slot region. Whereas the <0.5 MeV electron increase was quite sudden following the injection, the higher energy electron flux rose more gradually.

The question of whether adiabatic variations can explain the main phase dropout was addressed in Chapter 13. It was concluded that at an equatorial radius of $6 R_E$, less

than 10% of the flux decrease could be attributed to adiabatic variations. Evidence for real losses (as opposed to 'apparent' losses due to adiabatic variations) from magnetopause shadowing was presented in terms of 'butterfly' distributions in the CRRES fluxes. An argument for real losses was also presented in terms of a factor of ~ 10 decrease observed at geosynchronous before the main phase began.

The radial diffusion model was discussed in Chapter 14. Here, for the first time, a time dependent outer boundary condition (determined by LANL geosynchronous data) and time dependent diffusion coefficients (parameterized by Kp) are used to evolve $f(L,t)$ through an entire 10 day storm period (in steps of 0.2 days). The D_{LL} coefficients are conservatively defined to be within the limits of values found in the literature. The model reproduces the essential features seen in the empirical results for 100-200 MeV/G electrons, including the main dropout and recovery, as well as other minor disturbances. Quantitatively, the model does not capture the abruptness (time scale of ~ 5 hours) of the dropout and injection, nor does it bring in enough electrons to low enough L. This perhaps could be remedied by fine tuning the various parameters., and will eventually be investigated. However, the level of agreement shown (Figures 14.8 to 14.11) supports the general conclusion that given an accurately defined time dependent outer boundary condition and time dependent D_{LL} , and a loss term τ , that $f(L, \mu \leq 200 \text{ MeV/G}, t)$ can be appropriately modeled by the radial diffusion equation (Equation 14.4). The dynamics which are incorporated in the outer boundary condition (temporal sinks and sources) may be translated deep into the radiation belts by 'enhanced' diffusion coefficients.

However, for higher energy electrons, with $\mu > \sim 700$ MeV/G, the dynamics are more complex. These electrons will now be discussed.

15.1 Inner Source for >1 MeV Electrons

In Chapter 14.5 it was pointed out that towards the end of the recovery phase the high energy electrons had developed a much different $f(L)$ profile as compared to the low energy electrons. Contrary to the 100 and 200 MeV/G electron $f(L)$ profiles which are consistent with an earthward radial diffusion from an external source, the 794 and 1000 MeV/G electron profiles $f(L)$ show a negative gradient which indicates an internal source of higher energy electrons within the outer boundary (Figures 14.10 and 14.11).

Wave particle interactions with whistler waves and pitch angle diffusion at constant energy as discussed in Chapter 7.2 involve a limited case of the fully general problem of diffusion in velocity space (including energy diffusion). In what follows, it should be recalled that the gyrofrequency given by $\Omega_{ce} \equiv |eB/m_e c|$ is defined for non-relativistic electrons. A relativistic electron will gyrate at a frequency corrected by the relativistic correction factor γ . *Kennel and Engelmann* [1966] performed a quasi-linear analysis for the general case of velocity space diffusion. They found that although electron resonant cyclotron interactions for $\omega \ll \Omega_{ce}/\gamma$ (as is the typical case within the plasmasphere) led primarily to pitch-angle diffusion, Landau resonance and cyclotron resonance for $\omega \geq \Omega_{ce}/\gamma$ could lead to energy diffusion rates comparable to or greater than pitch-angle diffusion rates. *Kennel* [1969] suggested that electron heating within the inner magnetosphere due to cyclotron resonant wave-particle-interactions is possible,

particularly just outside the plasmasphere where the cold plasma density drops off but the magnetic field is not yet greatly weakened. *Lyons* [1974a] developed general expressions which relate energy diffusion coefficients (D_w) to pitch-angle diffusion coefficients ($D_{\alpha\alpha}$). He then applied them to the specific case of electron resonance with an assumed whistler wave spectrum *Lyons* [1974b]. *Lyons* found that in the limit of strong pitch-angle diffusion, where pitch-angle scattering rates are much greater than loss rates, energy diffusion can become quite significant. Based on these analyses, it is therefore possible that considerable energy diffusion may accompany pitch-angle diffusion at relatively low L (though outside the plasmasphere) during storms when the plasmasphere is compressed inwards from $L \sim 5$ to $L \sim 3$.

Chapter 7.2 introduced the whistler mode prevalent throughout the plasmasphere (plasmaspheric hiss) and discussed how hiss drives electron pitch angle diffusion through cyclotron resonant wave-particle interactions. This is the dominant loss mechanism for electrons within the plasmasphere. Chorus is another whistler mode which exists outside the plasmasphere. The generation of chorus has been discussed in terms of substorm injection of keV electrons [*Thorne, et al.*, 1974; *Anderson and Maeda*, 1977], yet much less attention has been devoted to quantifying the role which chorus may play in radiation belt electron dynamics [*Temerin*, 1994; *Li, et al.*, 1997b].

The CRRES Plasma Wave experiment (Chapter 9.4) provided measurements of plasma waves throughout the radiation belt region and may provide a clue as to the internal source required for the > 1 MeV electrons. Figure 15.1 is a survey plot of the electric field spectral power density (color coded) in units of $(V/m)^2/Hz$ plotted for 0.1

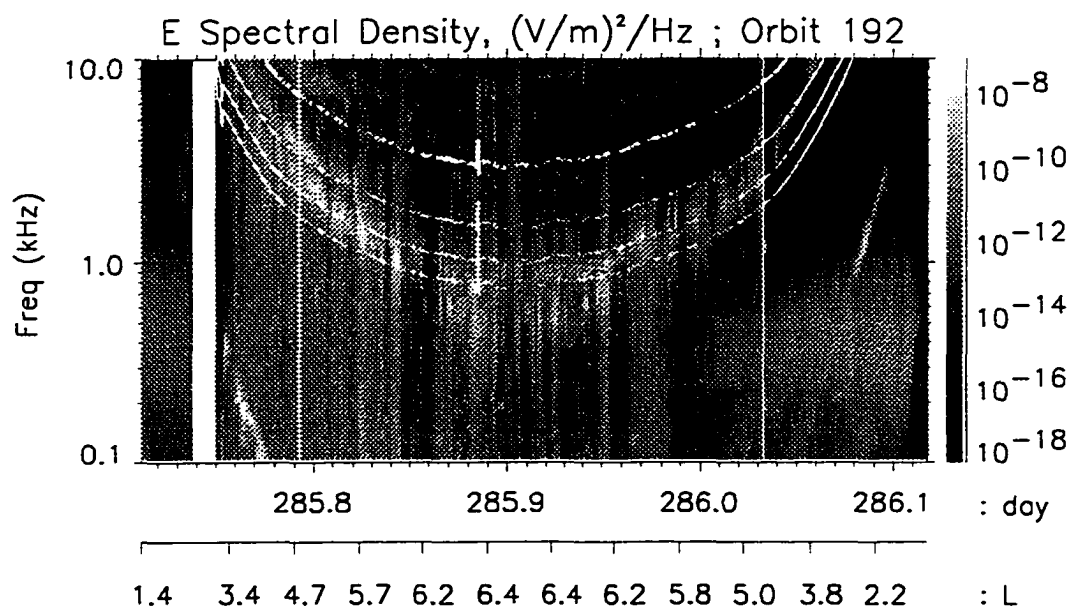
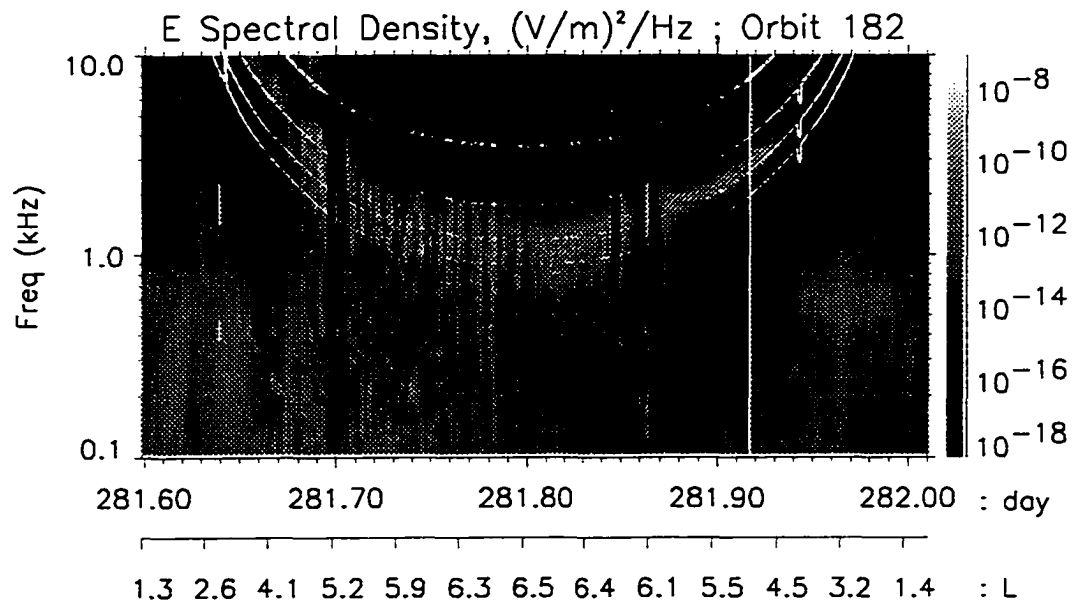


Figure 15.1: Plasma wave survey for orbits 182 and 192.

to 10.0 kHz (y-axis) versus decimal day of year (x-axis). The top panel is for orbit 182 (quiet, pre-SSC) and the bottom panel is for orbit 192 (active, recovery phase). Small arrows along the x-axis mark the plasmopause location. Included as auxiliary axes are L and magnetic latitude (Mlat). The full orbit is shown, from perigee to apogee around L=6.5 and back to perigee. For the region below L=6, the magnetic local time (MLT) coverage for the ascending(descending) leg is from 2-3 (6-7) hours MLT. The thick top white curve superimposed on the wave data is the gyrofrequency (kHz) of the cold plasma electrons (with $\gamma=1.0$) calculated from the following equation:

$$f_{gyro} = \frac{1}{2\pi} \left(\frac{qB}{m_o \gamma c} \right) \frac{1}{1000} \text{ kHz} \quad (15.1)$$

where charge $q=4.803 \cdot 10^{-10}$ esu, electron rest mass $m_o=9.11 \cdot 10^{-28}$ g, speed of light $c = 3.0 \cdot 10^{10}$ cm/s, the CRRES magnetic field B is in Gauss, and γ is the relativistic factor. The three thinner white curves below this reference gyrofrequency, are the gyrofrequencies for the relativistic electrons (0.5, 1.0, and 1.5 MeV from top to bottom).

Orbit 192 clearly demonstrates wave power of intensities much greater than seen for orbit 182, though both types of whistler waves (hiss and chorus) are present in each orbit. Plasmaspheric hiss is seen as the band of 0.2 to 0.8 kHz wave power confined to the plasmasphere and with a maximum power shown for orbit 192, $\sim 10^{-10}$ (V/m)² / Hz (in yellow). Chorus, with the most intense wave power for orbit 192, $\sim 10^{-8}$ (V/m)² / Hz (in red), is found outside the plasmasphere in frequency bands below the cold electron gyrofrequency. The chorus amplitudes seen throughout orbit 192 are more than an order of magnitude larger than those seen for orbit 182. Integrated over frequency and

space, the total chorus power available to resonant electrons in orbit 192 is even more significant. Referring to the thin white curves representing the relativistic electron gyrofrequencies, it is evident that there is considerable whistler power at wave frequencies $\omega \geq \Omega_{ce}/\gamma$ outside the plasmasphere, criteria which *Kennel and Engelmann* [1966] and *Kennel* [1969] set forth for energy diffusion.

A survey of the wave spectral densities for the remaining orbits throughout this storm period (not shown) show other orbits with whistler intensities equal to that of orbit 192. However, it is seen that chorus has a strong magnetic latitude and local time dependence, as well as the dependence on magnetic activity evident in Figure 15.1. The intense chorus bands are confined to those orbits which lie within 10° of the magnetic equator. Of these orbits, the more intense chorus is primarily (though not exclusively) found during the ascending leg (MLT=2-3 hr) as opposed to the descending leg (MLT=6-7 hr). These observations agree with those of *Tsurutani and Smith* [1974], and are consistent with the scenario where 10-100 keV electrons are injected at midnight local time during high magnetic activity (substorms) and drift eastward (gradient plus curvature) around to post-midnight. The intense chorus located in the early post-midnight sector are attributed to these freshly injected <100 keV electrons [*Thorne, et al.*, 1974; *Anderson and Maeda*, 1977].

To quantitatively 'prove' that these waves are the internal source needed to explain the 1000 MeV/G electrons is beyond the scope of this thesis. However, the wave observations, taken together with the earlier theoretical work, supports the plausible scenario that enhanced chorus activity brought on by the storm activity

provides the required environment for energy diffusion inside the outer boundary of $L^*=6$.

15.2 Pitch Angle Dependent Diffusion Coefficients

The radial diffusion modeling in this thesis used diffusion coefficients whose form originated from the general formalism developed by *Falthammar* [1965] for equatorial mirroring particles (Equations 7.11, D_{LL}^E ; 7.13, D_{LL}^M). This can be seen by the fact that the derivations began with the guiding center equation (Equation 7.8) for \mathbf{u}_\perp which included the $\mathbf{E} \times \mathbf{B}$ and the ∇B drift, but ignored the curvature drift for particles moving along the field line (\mathbf{u}_\parallel). It has been shown that when the effects for parallel motion are considered, D_{LL}^M is seen to have a sensitive dependence on equatorial pitch angle, being strongest for equatorial mirroring particles [*Schulz and Lanzerotti*, 1974; *Walt*, 1994]. An electron with an equatorial pitch angle of $\alpha_{eq} < 30^\circ$ will diffuse ~ 10 times more slowly than an electron with $\alpha_{eq} = 90^\circ$. The dependence changes sharply for $\alpha_{eq} > 30^\circ$; a 55° particle will diffuse half as fast. It may be recalled from the discussion of Figure 14.2 (Chapter 14.1) that electrons observed with smaller J ($\alpha_{eq} \sim 60^\circ - 75^\circ$) appeared to be injected to $L^* = 4.1$ more rapidly than electrons with larger J ($\alpha_{eq} \sim 20^\circ - 35^\circ$). Assuming that the injection may be interpreted as the result of 'enhanced' radial diffusion from magnetic field fluctuations, these observations would be consistent with the D_{LL}^M latitudinal effect.

The dependence on pitch angle found for D_{LL}^M is not found for D_{LL}^E [*Schulz and Lanzerotti*, 1974; *Walt*, 1994] This assumes there are no field-aligned electric fields,

which is usually taken to be a good assumption inside the plasmasphere where there are plenty of fast moving electrons to short out transient electric fields, but not as good outside the plasmasphere. An electron will respond to convection electric field fluctuations independent of its latitude.

The modeling in Chapter 14 used $f(\mu, J, L^*)$ for $J=1.78 \cdot 10^{-16}$ g(cm/s) R_E which corresponds to electrons with $\alpha_{eq} \sim 40-60^\circ$. Assuming the latitudinal dependence for D_{LL}^M shown by *Walt* [1994], the errors introduced by assuming an equatorial D_{LL}^M may be a factor of ~ 2 . On the other hand, noting the spread of \sim two orders of magnitude in D_{LL} in Figure 7.7, a factor of 2 does not seem to be of grave consequence.

15.3 Injections

It has been well documented in this thesis that a significant 'injection' of ~ 340 keV electrons deep into the slot region (Figure 10.5) occurred during the beginning of the magnetic storm recovery phase. It is interesting to note that while storm time injections of 100s keV to ~ 1 MeV electrons into the slot region have certainly been reported in the literature for sometime [*Williams, et al.*, 1968; *Lyons and Williams*, 1975], the injection timing relative to storm phases is often not stressed, and perhaps should be. The timing is often difficult to ascertain because of plots spanning several months or because of inadequate time resolution of the data. In *Williams, et al.* [1968], it is implied that these deep storm injections are initiated during the main phase. Although some of the storms analyzed appear to exhibit a main phase injection, others are more questionable.

On the other hand, there are cases in the literature which make unreferenced claims that these injections occur primarily during the recovery phase, as if this were general knowledge. "During the recovery phase, when the dipolarization effect is observed, injections of new electrons seem to be the rule." [*Bourdarie, et al.*, 1996]. "The ~1 MeV electrons are injected to L~3 during strong magnetic storms only when, as a rule, the storms are in their recovery phase." [*Tverskaya*, 1996]. The injection observed during the 9 October 1990 storm analyzed for this thesis certainly is consistent with these claims, but hardly offers firm statistical footing.

The injection dynamic is most often discussed within the context of substorms [*Baker, et al.*, 1982; *Lopez, et al.*, 1989]. During a substorm growth phase the magnetotail becomes stretched to a highly non-dipolar configuration during a period of southward IMF. The expansion phase is triggered by an abrupt dipolarization which injects 10s to 100s keV electrons (and ions) from the tail into the local nighttime geosynchronous region. Substorm injections are relatively localized events and occur more frequently than the globally disruptive magnetic storm. Although it is recognized that injections are associated with both substorms (in isolation from storms) and storms, *Lyons and Schulz* [1989] state that there is an 'important phenomenological distinction' between the two cases. They point out that although injections into the region $L > 4$ are comparable for the isolated substorm and the storm, significant particle increases at $L < 4$ are restricted to storm injections (the case in this thesis). Yet, despite the claims of some [*Bourdarie, et al.*, 1996; *Tverskaya*, 1996] that storm-time injections are typically observed during the recovery phase, *Lyons and Schulz* [1989] restrict their discussion of

storm injections to the main phase, as the implied source of the main phase ring current (as discussed in Chapter 8), with no mention of recovery phase injections.

Obviously, much of this confusion revolves around what exact energies are being discussed. Certainly, lower energy particles are 'injected' into the slot region during the main phase, since these are the ring current particles which produce the main phase. However, it appears that often time the literature gets 'careless' in categorizing all deep storm injections (including energies >300 keV up to ~ 1 MeV) as main phase injections, associating them with the ring current build up. The point here is, that the distinction between a main phase and recovery phase injection may be a significant one, and perhaps warrants a little closer attention.

CHAPTER 16

CONCLUSIONS

This thesis has made a significant step towards understanding the dynamics of the outer zone electrons throughout an entire magnetic storm. This has been accomplished by modeling the radial diffusion process using time dependent outer boundary conditions and time dependent diffusion coefficients throughout the entire storm; something which has never been done before. The time dependent outer boundary conditions are based on geosynchronous flux data which are available throughout the time period of interest, and which account for the sources and sinks outside the modeling region. The time dependent diffusion coefficients D_{LL} are driven by the magnetic activity index K_p , with D_{LL} for the most active period ($K_p \sim 6$) enhanced over those for the quiet period ($K_p \sim 1$) by around two orders of magnitude.

With these enhanced diffusion coefficients, which are required to effectively couple the geosynchronous region to the radiation belt interior, it has been shown that electron enhancements at geosynchronous (when used as an outer boundary condition) act as an effective 'source' to replenish the radiation belt with fresh electrons. It has also been shown that large electron losses at geosynchronous, act as an effective 'sink' to drain a large portion of the radiation belt electrons from deep in the interior. As *Bourdarie, et al.* [1996] commented, "This phenomenon, like flushing, regularly removes

the major part of the high-energy electrons." They conclude their modeling study with the assessment that "A full understanding of this process remains to be constructed."

The work performed in this thesis has certainly provided a viable solution.

The anomalous (for inward radial diffusion) profiles of f seen for the highest μ electrons has raised the question of what mechanism may be acting as an internal source of >1 MeV electrons. The chorus waves seen throughout the recovery phase are a primary candidate for heating the electrons via the type of resonant cyclotron interactions proposed in the past, and certainly deserve some serious investigation.

Thus, this study has seemingly answered some questions, and pointed to still others.

REFERENCES

- Albert, J.M., Quasi-linear Pitch Angle Diffusion Coefficients: Retaining High Harmonics, *J. Geophys. Res.*, **99**, 23,741-23,745, 1994.
- Alfven, H., Cosmical Electrodynamics, Clarendon Press, Oxford, 1950.
- Anderson, R.R. and K. Maeda, VLF Emissions Associated With Enhanced Magnetospheric Electrons, *J. Geophys. Res.*, **82**, 135-146, 1977.
- Anderson, R.R., D.A. Gurnett, and D.L. Odem, The CRRES Wave Experiment, *J. Spacecraft and Rockets*, **29**, 570-573, 1992.
- Arnoldy, R.L., R.A. Hoffman, and J.R. Winckler, *J. Geophys. Res.*, **65**, 1361-1376, 1960.
- Baker, D.N., T.A. Fritz, B. Wilken, P.R. Higbie, S.M. Kaye, M.G. Kivelson, T.E. Moore, W. Studemann, A.J. Masley, P.H. Smith, and A.L. Vampola, Observation and Modeling of Energetic Particles at Synchronous Orbit on July 29, 1977, *J. Geophys. Res.*, **87**, 5917-5932, 1982
- Baker, D.N., J.B. Blake, R.W. Klebesadel and P.R. Higbie, Highly Relativistic Electrons in the Earth's Outer Magnetosphere: 1. Lifetimes and Temporal History 1979-1984, *J. Geophys. Res.*, **91**, p 4265-4276, 1986.
- Bass, J.N., M.S. Gussenhoven, and R.H. Redus, The Importance of Adiabatic Variations in Trapped Particle Distributions Observed by the SCATHA Satellite, *USAF Geophysics Laboratory Technical Report*, GL-TR-89-0233, 1989.
- Beutier, T. and D. Boscher, A Three-Dimensional Analysis of the Electron Radiation Belt by the Salammbô Code, *J. Geophys. Res.*, **100**, 14853-14861, 1995.
- Bhavnani, K.H and R.P. Vancour, Coordinate Systems for Space and Geophysical Applications, *USAF Phillips Laboratory Technical Report*, PL-TR-91-2296, 1991.
- Blake, J.B., W.A. Kolasinski, R.W. Filippus, and E.G. Mullen, Injection of Electrons and Protons with Energies of Tens of MeV into L<3 on March 24, 1991, *Geophys. Res. Lett.*, **19**, 821, 1992.

- Blake, J.B., D.N. Baker, N. Turner, K.W. Ogilvie, and R.P. Lepping, Correlation of Changes in the Outer-Zone Relativistic-Electron Population with Upstream Solar Wind and Magnetic Field Measurements, *Geophys. Res. Lett.*, **24**, 927-929, 1997.
- Bourdarie, S., D. Boscher, T. Beutier, J-A Sauvaud, M. Blanc, Magnetic Storm Modeling in the Earth's Electron Belt by the Salammbro Code, *J. Geophys. Res.*, **101**, 2771-27176, 1996.
- Brautigam, D.H., M.S. Gussenhoven, and E.G. Mullen, Quasi-Static Model of Outer Zone Electrons, *IEEE Trans. Nuc. Sci.*, **39**, 1797, 1992.
- Brown, W.L., Energetic Outer Belt Electrons at Synchronous Altitude, in Earth's Particles and Fields, edited by B.M. McCormac, p 33, Reinhold Publishing Corp., New York, 1968.
- Chapman, S. and V.C.A. Ferraro, A New Theory of Magnetic Storms, *Terrest. Magnetism and Atmospheric Elec.*, **36**, 77, 171, 1931.
- Cornwall, J.M., Scattering of energetic trapped electrons by very-low-frequency waves, *J. Geophys. Res.*, **69**, 1251-1258, 1964.
- Cornwall, J.M., Diffusion Processes Influenced by Conjugate-point Wave Phenomena, *Radio Sci.*, **3**, 740, 1968.
- Davis, L., and D.B. Chang, On the Effect of Geomagnetic Fluctuations on Trapped Particles, *J. Geophys. Res.*, **67**, 2169-2179, 1962.
- Dessler, A.J. and R. Karplus, Some Properties of the Van Allen Radiation, *Phys. Rev. Letters*, **4**, 271-274, 1960.
- Dessler, A.J. and R. Karplus, Some Effects of Diamagnetic Ring Current on Van Allen Radiation, *J. Geophys. Res.*, **66**, 2289-2295, 1961.
- Ding, C., T.W. Hill, and F.R. Toffoletto, Improvement of the Toffoletto-Hill Open Magnetosphere Model, in Physics of Space Plasmas, edited by T. Chang and J.R. Jasperse, MIT Press, Cambridge, MA, 1997.
- Dungey, J.W., Interplanetary Magnetic Field and the Auroral Zones, *Phys. Rev. Letts.*, **6**, 47, 1961.
- Dungey, J.W., Loss of Van Allen Electrons Due to Whistlers, *Planet. Space Sci.*, **11**, 591-596, 1963.
- Dungey, J.W., Effects of Electromagnetic Perturbations on Particles Trapped in the Radiation Belts, *Space Science Reviews*, **4**, 199-222, 1964.

- Fairfield, D.H., The Average Magnetic Field Configuration of the Outer Magnetosphere, *J. Geophys. Res.*, **73**, 7329-7338, 1968.
- Falthammer, C-G., Effects of Time-Dependent Electric Fields on Geomagnetically Trapped Radiation, *J. Geophys. Res.*, **70**, 2503-2516, 1965.
- Falthammer, C-G., On the Transport of Trapped Particles in the Outer Magnetosphere, *J. Geophys. Res.*, **71**, 1487-1491, 1966.
- Frank, L.A., J.A. Van Allen, and H.K. Hills, A Study of Charged Particles in the Earth's Outer Radiation Zone With Explorer 14, *J. Geophys. Res.*, **69**, 2171-2191, 1964.
- Frank, L.A., Inward Radial Diffusion of Electrons of Greater Than 1.6 Million Electron Volts in the Outer Radiation Zone, *J. Geophys. Res.*, **70**, 3533-3539, 1965.
- Freeman, J.W., The Morphology of the Electron Distribution in the Outer Radiation Zone and Near the Magnetospheric Boundary as Observed by Explorer 12, *J. Geophys. Res.*, **69**, 1691-1723, 1964.
- Gold, T., Origin of the Radiation Near the Earth Discovered by Means of Satellites, *Nature*, **183**, 355-358, 1959.
- Gussenhoven, M.S., D.A. Hardy, and N. Heinemann, Systematics of the Equatorward Diffuse Auroral Boundary, *J. Geophys. Res.*, **88**, 5692, 1983.
- Gussenhoven, M.S., E.G. Mullen, M. Sperry and K.J. Kerns, The Effect of the March 1991 Storm on Accumulated Dose for Selected Satellite Orbits: CRRES Dose Models, *IEEE Trans. Nucl. Sci.*, **39**, 1765, 1992.
- Gussenhoven, M.S., E.G. Mullen, and D.H. Brautigam, Improved Understanding of the Earth's Radiation Belts from the CRRES Satellite, *IEEE Trans. Nuc. Sci.*, **43**, 353-368, 1996a.
- Gussenhoven, M.S., E.G. Mullen, and D.H. Brautigam, Phillips Laboratory Space Physics Division Radiation Models, Workshop on Trapped Radiation Belts, Geophysical Monograph, American Geophysical Union, 1996b.
- Haerendel, G., Diffusion Theory of Trapped Particles and the Observed Proton Distribution, in Earth's Particles and Fields, edited by B.M. McCormac, p 171, Reinhold Publishing Corp., New York, 1968.
- Haymes, R.C., Introduction to Space Science, John Wiley & Sons, Inc., New York, 1971.

- Herlofson, N., Diffusion of Particles in the Earth's Radiation Belts, *Phys. Rev. Letters*, **5**, 414-416, 1960.
- Hess, W.N., The Radiation Belt Produced by Neutrons Leaking out of the Atmosphere of the Earth, *J. Geophys. Res.*, **65**, 3107-3115, 1960.
- Hilmer, R.V., and G.H. Hoigt, A Magnetospheric Magnetic Field Model with Flexible Current systems Driven by Independent Physical Parameters, *J. Geophys. Res.*, **100**, 5613-5626, 1995.
- Hilmer, R.V., G.P. Ginet, and T.E. Cayton, A Multi-Satellite View of Energetic Electron Flux Increases at L=4-7 Associated with High Speed Solar Wind Streams, *Eos Trans.*, p593, AGU, Fall Meeting 1996.
- Holzworth, R.H. and F.S. Mozer, Direct Evaluation of the Radial Diffusion Coefficient Near L=6 Due to Electric Field Fluctuations, *J. Geophys. Res.*, **84**, 2559-2566, 1979.
- Ichimaru, S., Basic Principles of Plasma Physics, Addison-Wesley, 1973.
- Jasna, D., U.S. Inan, and T.F. Bell, Equatorial gyroresonance between electrons and magnetospherically reflected whistlers, *Geophys. Res. Let.*, **17**, 1865-1868, 1990.
- Kaufmann, R.L., Substorm Currents: Growth Phase and Onset, *J. Geophys. Res.*, **92**, 7471-7486, 1987.
- Kellogg, P.J., Van Allen Radiation of Solar Origin, *Nature*, **183**, 1295-1297, 1959.
- Kellogg, P.J., Electrons of the Van Allen Radiation, *J. Geophys. Res.*, **65**, 2705, 1960.
- Kennel, C.F. and F. Engelmann, Velocity Space Diffusion from Weak Plasma Turbulence in a Magnetic Field, *Phys. Fluids.*, **9**, 2377, 1966.
- Kennel, C.F., and H.E. Petschek, Limit on stably trapped particle fluxes, *J. Geophys. Res.*, **71**, 1-28, 1966.
- Kennel, C.F., Consequences of a Magnetospheric Plasma, *Rev. Geophys.*, **7**, 379, 1969.
- Kerns, K.J. and M.S. Gussenhoven, CRRESRAD Documentation, PL-TR-94-2218, Phillips Laboratory, AFMC, Hanscom AFB, MA, 1992.
- Kim, H.-J. and A. A.Chan, Fully Adiabatic Changes in Storm Time Relativistic Electron Fluxes, *J. Geophys. Res.*, **102**, 22107-22116, 1997.
- Kivelson, M.G., and C.T. Russell (editors), Introduction to Space Physics, Cambridge Univ. Press, 1995.

- Koons, H.C., and D.A. McPherson, Observation of very-low-frequency whistler-mode waves in the region of the radiation-belt slot, *J. Geophys. Res.*, **77**, 3475-3482, 1972.
- Koons, H.C., A.L. Vampola, and D.A. McPherson, Strong pitch-angle scattering of energetic electrons in the presence of electrostatic waves above the ionospheric trough region, *J. Geophys. Res.*, **77**, 1771-1775, 1972.
- Lanzerotti, L.J., C.G. MacLennan, and M. Schulz, Radial Diffusion of Outer-Zone Electrons: An Empirical Approach to Third-Invariant Violation, *J. Geophys. Res.*, **75**, 5351-5371, 1970.
- Lanzerotti, L.J. and C.G. Morgan, ULF Geomagnetic Power Near L=4, 2. Temporal Variation of the Radial Diffusion Coefficient for Relativistic Electrons, *J. Geophys. Res.*, **78**, 4600-4610, 1973.
- Lanzerotti, L.J., D.C. Webb, and C.W. Arthur, Geomagnetic Field Fluctuations at Synchronous Orbit, 2. Radial Diffusion, *J. Geophys. Res.*, **83**, 3866-3870, 1978.
- Lanzerotti, L.J., and A. Wolfe, Particle Diffusion in the Geomagnetosphere: Comparison of Estimates From Measurements of Magnetic and Electric Field Fluctuations, *J. Geophys. Res.*, **85**, 2346-2348, 1980.
- Li, X., I. Roth, M. Temerin, J.R. Wygant, M.K. Hudson, J.B. Blake, Simulation of the Prompt Energization and Transport of Radiation Belt Particles During the March 24, 1991 SSC, *Geophys. Res. Lett.*, **20**, 2423, 1993.
- Li, X., D. Baker, M. Temerin, D. Larson, R.P. Lin, E.G.D. Reeves, M. Looper, S.G. Kanekal, and R.A. Mewaldt, Are Energetic Electrons in the Solar Wind the Source of the Outer Radiation Belt?, *Geophys. Res. Lett.*, **24**, 923-926, 1997a.
- Li, X., D. Baker, M. Temerin, M. Temerin, T.E. Cayton, E.G.D. Reeves, R.A. Christensen, J.B. Blake, M.D. Looper, R. Nakamura, and S.G. Kanekal, Satellite Observations of the Outer Zone Electron Variation During the 3-4 November 1993 Magnetic Storm, submitted to *J. Geophys. Res.*, 1997b.
- Lopez, R.E., A.T. Y. Lui, D.G. Sibeck, K. Takahashi, R.W. McEntire, L.J. Zanetti, and S.M. Krimigis, On the Relationship Between the Energetic Particle Flux Morphology and the Change in the Magnetic Field Magnitude During Substorms, *J. Geophys. Res.*, **94**, 17105-17119, 1989.
- Lyons, L.R., R.M. Thorne, and C.F. Kennel, Pitch-Angle Diffusion of Radiation Belt Electrons within the Plasmasphere, *J. Geophys. Res.*, **77**, 3455-3474, 1972.

- Lyons, L.R., and R.M. Thorne, Equilibrium structure of radiation belt electrons, *J. Geophys. Res.*, **78**, 2142-2149, 1973.
- Lyons, L.R., General relations for resonant particle diffusion in pitch angle and energy, *J. Plasma Physics*, **12**, 45-49, 1974a.
- Lyons, L.R., Pitch angle and energy diffusion coefficients from resonant interactions with ion-cyclotron and whistler waves, *J. Plasma Physics*, **12**, 417-432, 1974b.
- Lyons, L.R., and D.J. Williams, The quiet time structure of energetic (35-560 keV) radiation belt electrons, *J. Geophys. Res.*, **80**, 943-950, 1975.
- Lyons, L.R., and D.J. Williams, The Storm and Poststorm Evolution of Energetic (35-560 keV) Radiation Belt Electron Distributions, *J. Geophys. Res.*, **80**, 3987-3994, 1975.
- Lyons, L.R., and D.J. Williams, A Source for the Geomagnetic Storm Main Phase Ring Current, *J. Geophys. Res.*, **85**, 523-530, 1980.
- Lyons, L.R., and D.J. Williams, Quantitative Aspects of Magnetospheric Physics, D. Reidel Publishing Co., Hingham, MA., 1984.
- Lyons, L.R., and M. Schulz, Access of Energetic Particles to Storm Time Ring Current Through Enhanced Radial "Diffusion", *J. Geophys. Res.*, **94**, 5491-5496, 1989.
- McIlwain, C.E., Coordinates for Mapping the Distribution of Magnetically Trapped Particles, *J. Geophys. Res.*, **66**, 3681-3691, 1961.
- McIlwain, C.E., Processes Acting Upon Outer Zone Electrons, 1, Adiabatic Perturbations, UCSD-SP-66-5, Preprint of paper presented at Inter-Union Symposium on Solar-Terrestrial Physics, Belgrade, Yugoslavia, 1966; also published in Workshop on Trapped Radiation Belts, Geophysical Monograph xx, American Geophysical Union, 1996.
- Mead, G.D., Deformation of the Geomagnetic Field by the Solar Wind, *J. Geophys. Res.*, **69**, 1181, 1964.
- Mozer, F.S., Power Spectra of the Magnetospheric Electric Field, *J. Geophys. Res.*, **76**, 3651-3667, 1971.
- Mullen, E.G. and M.S. Gussenhoven, A Double-Peaked Inner Radiation Belt: Cause and Effect as Seen on CRRES, *IEEE Trans. on Nuc. Sci.*, **38**, 1713-1718, 1991.
- Nakada, M.P., and G.D. Mead, Diffusion of Protons in the Outer Radiation Belt, *J. Geophys. Res.*, **70**, 4777-4791, 1965.

- Ness, N.F., C.S. Searce, and J.B. Seek, Initial Results of the IMP I Magnetic Field Experiment, *J. Geophys. Res.*, **69**, 3531, 1964.
- Newkirk, L.L. and M. Walt, Radial Diffusion Coefficient for Electrons at $1.76 < L < 5$, *J. Geophys. Res.*, **73**, 7231-7236, 1968.
- Nishida, A., Geomagnetic Diagnosis of the Magnetosphere, Springer Verlag, NY, 1978.
- Northrop, T.G. and E. Teller, Stability of the Adiabatic Motion of Charged Particles in the Earth's Field, *Phys. Rev.*, **117**, 215-225, 1960.
- Northrop, T.G., The Adiabatic Motion of Charged Particles, 1963.
- O'Brien, B.J., Lifetime of Outer Zone Electrons and Their Precipitation into the Atmosphere, *J. Geophys. Res.*, **67**, 3687-3706, 1962.
- O'Brien, B.J., J.A. Van Allen, C.D. Laughlin, and L.A. Frank, Absolute Electron Intensities in the Heart of the Earth's Outer Radiation Zone, *J. Geophys. Res.*, **67**, 397-402, 1962.
- O'Brien, B.J., A Large Diurnal Variation of the Geomagnetically Trapped Radiation, *J. Geophys. Res.*, **68**, 989-995, 1963.
- Olson, W.P., and K.A. Pfitzer, A Dynamic Model of the Magnetospheric Magnetic and Electric Fields for July 29, 1977, *J. Geophys. Res.*, **87**, 5943-5948, 1982.
- Parker, E.N., Geomagnetic Fluctuations and the Form of the Outer Zone of the Van Allen Radiation Belt, *J. Geophys. Res.*, **65**, 3117-3130, 1960.
- Parks, G.K., Physics of Space Plasmas, Addison-Wesley Publishing Co., Redwood City, CA., 1991.
- Paulikas, G.A., J.B. Blake, and S.C. Freden, Precipitation of energetic electrons at middle latitudes, *J. Geophys. Res.*, **71**, 3165-3172, 1966.
- Paulikas, G.A., J.B. Blake, S.C. Freden, and S.S. Imamoto, Observations of Energetic Electrons at Synchronous Altitude, 1. General Features and Diurnal Variations, *J. Geophys. Res.*, **73**, 4915, 1968.
- Paulikas, G.A. and J.B. Blake, Effects of the Solar Wind on Magnetospheric Dynamics: Energetic Electrons at the Synchronous Orbit, p 180-202, Quantitative Modeling of Magnetospheric Processes, AGU Geophysical Monograph 21, Olson, W.P., editor, 1979.

- Pfizer, K.A., Magnetospheric Configuration and Energetic Particle Effects Associated With a SSC: A Case Study of the CDAW 6 Event on March 22, 1979, *J. Geophys. Res.*, **91**, 1459, 1986.
- Press, W.H., Flannery, B.P., S.A. Teukolsky, and W.T. Vetterling, Numerical Recipes, Cambridge University Press, 1988.
- Roberts, C.S., Cyclotron-resonance and Bounce Resonance Scattering of Electrons Trapped in the Earth's Magnetic Field, in Earth's Particles and Fields, edited by B.M. McCormac, p 317, Reinhold Publishing Corp., New York, 1968.
- Roberts, C.S., Pitch-angle Diffusion of Electrons in the Magnetosphere, *Rev. Geophys. Space Phys.*, **7**, 305, 1969.
- Roederer, J.G., On the Adiabatic Motion of Energetic Particles in a Model Magnetosphere, *J. Geophys. Res.*, **72**, 981-992, 1967.
- Roederer, J.G., Dynamics of Geomagnetically Trapped Radiation, Springer and Verlag, New York, 1970.
- Rosen, A., and T. Farley, Characteristics of the Van Allen Radiation Zones as Measured by the Scintillation Counters on Explorer VI, *J. Geophys. Res.*, **66**, 2013-2028, 1961.
- Rosenbluth, M., and C. Longmire, *Ann. Phys. N. Y.*, **1**, 120, 1957.
- Rothwell, P., and C.E. McIlwain, Magnetic Storms and the Van Allen Radiation Belts - Observations from Satellite ϵ , *J. Geophys. Res.*, **65**, 799-806, 1960.
- Rowland, D.E., and J.R. Wygant, The Dependence of the Large Scale Inner-Magnetospheric Electric Field on Geomagnetic Activity, submitted to *J. Geophys. Res.*, 1997.
- Sawyer, D.M., and J.I. Vette, The AP-8 Trapped Proton Environment for Solar Maximum and Solar Minimum, National Space Science Data Center, NSSDC/WDC-A-R&S 76-06, 1976.
- Scarf, F.L., G.M. Crook, and R.W. Fredricks, Preliminary report on detection of electrostatic ion waves in the magnetosphere, *J. Geophys. Res.*, **70**, 3045-3060, 1965.
- Schulz, M. and A. Eviatar, Diffusion of Equatorial Particles in the Outer Radiation Zone, *J. Geophys. Res.*, **74**, 2132-2192, 1969.

- Schulz, M. and L.J. Lanzerotti, Particle Diffusion in the Radiation Belts, Springer and Verlag, New York, 1974.
- Selesnick, R.S., J.B. Blake, W.A. Kolasinski, and T.A. Fritz, A Quiescent State of 3 to 8 MeV Radiation Belt Electrons, *Geophys. Res. Lett.*, **24**, 1343-1346, 1997.
- Selesnick, R.S. and J.B. Blake, Dynamics of the Outer Radiation Belt, *Geophys. Res. Lett.*, **24**, 1347-1350, 1997.
- Singer, H.J., W.P. Sullivan, P. Anderson, F. Mozer, P. Harvey, J. Wygant, and W. McNeil, Fluxgate Magnetometer Instrument on the CRRES, *J. Spacecraft and Rockets*, **29**, 599-601, 1992.
- Smith, E.J., Frandsen, M.A., Tsurutani, B.T., Thorne, R.M., and Chan, K.W., Plasmaspheric Hiss Intensity Variations During Magnetic Storms, *J. Geophys. Res.*, **79**, 2507-2510, 1974.
- Spjeldvik, W.N. and P.L. Rothwell, The Radiation Belts, from Handbook of Geophysics and the Space Environment, scientific editor, Adolph S. Jursa, 1985, Air Force Geophysics Laboratory.
- Stormer, L., Polar Aurora, Clarendon Press, Oxford, 1955.
- Stone, E.C., The Physical Significance and Application of L, B₀, and R₀, to Geomagnetically Trapped Particles, *J. Geophys. Res.*, **68**, 4157-4166, 1963.
- Temerin, M., New Paradigm for the Transport and Energization of Radiation Belt Particles, *Eos Trans.*, p538, AGU, Fall Meeting 1994.
- Thorne, R.M. and C.F. Kennel, Relativistic Electron Precipitation During Magnetic Storm Main Phase, *J. Geophys. Res.*, **76**, p 4446-4453, 1971
- Thorne, R.M., E.J. Smith, R.K. Burton, and R.E. Holzer, Plasmaspheric Hiss, *J. Geophys. Res.*, **78**, 1581-1596, 1973.
- Thorne, R.M., E.J. Smith, K.J. Fiske, and S.R. Church, Intensity Variation of ELF Hiss and Chorus During Isolated Substorms, *Geophys. Res. Lett.*, **1**, 193-196, 1974.
- Tsurutani, B.T., and E.J. Smith, Postmidnight Chorus: A Substorm Phenomenon, *J. Geophys. Res.*, **79**, 118-127, 1974.
- Tsyganenko, N.A., A Magnetospheric Magnetic Field Model with a Warped Tail Current Sheet, *Planet. Space Sci.*, **37**, 5-20, 1989.

- Tverskaya, L.V., Dynamics of Energetic Electrons in the Radiation Belts, in Radiation Belts: Models and Standards, Geophysical Monograph 97, American Geophysical Union, 1996.
- Vampola, A.L., Electron Pitch Angle Scattering in the Outer Zone during Magnetically Disturbed Times, *J. Geophys. Res.*, **76**, 4685-4688, 1971.
- Vampola, A.L., J.V. Osborn, B.M. Johnson, CRRES Magnetic Electron Spectrometer AFGL-701-5A (MEA), *J. Spacecraft and Rockets*, **29**, 592-595, 1992.
- Van Allen, J.A., G.H. Ludwig, E.C. Ray, and C.E. McIlwain, Observation of High Intensity Radiation by Satellites 1958 Alpha and Gamma, *Jet Propulsion*, 588-592, September, 1958.
- Van Allen, J.A., C.E. McIlwain, and G.H. Ludwig, Radiation Observations with Satellite 1958 ε, *J. Geophys. Res.*, **64**, 271-286, 1959.
- Van Allen, J.A. and L.A. Frank, Radiation Around the Earth to a Radial Distance of 107,400 km., *Nature*, **183**, 430-434, 1959.
- Van Allen, J.A., The Geomagnetically Trapped Corpuscular Radiation, *J. Geophys. Res.*, **64**, 1683-1689, 1959.
- Van Allen, J.A., Origins of Magnetospheric Physics, Smithsonian Institution Press, Washington, D.C., 1983.
- Vette, J.I., The AE-8 Trapped Electron Model Environment, National Space Science Data Center, NSSDC/WDC-A-R&S 91-24, 1991.
- Walt, M. and W.M. MacDonald, Energy Spectrum of Electrons Trapped in the Geomagnetic Field, *J. Geophys. Res.*, **66**, 2047-2052, 1961.
- Walt, M. and W.M. MacDonald, The Influence of the Earth's Atmosphere on Geomagnetically Trapped Particles, *Rev. Geophys.*, **2**, 543, 1964.
- Walt, M., Loss Rates of Trapped Electrons by Atmospheric Collisions, in Radiation Trapped in the Earth's Magnetic Field, edited by B.M. McCormac, p 337, D. Reidel Publishing Co., Dordrecht, Holland, 1966.
- Walt, M., Introduction to Geomagnetically Trapped Radiation, Cambridge University Press, 1994.
- Wentworth, R.C., W.M. MacDonald, and S.F. Singer, Lifetimes of Trapped Radiation Belt Particles Determined by Coulomb Scattering, *Phys. Fluids*, **2**, 499, 1959.

- West, H.I., The Signatures of the Various Regions of the Outer Magnetosphere in the Pitch Angle Distributions of Energetic Particles, p 150-179, Quantitative Modeling of Magnetospheric Processes, AGU Geophysical Monograph 21, Olson, W.P., editor, 1979.
- West, H.I., R.M. Buck, and G.T. Davidson, The Dynamics of Energetic Electrons in the Earth's Outer Radiation Belt During 1968 as Observed by the Lawrence Livermore National Laboratory's Spectrometer on Ogo 5, *J. Geophys. Res.*, **86**, 2111-2142, 1981.
- Williams, D.J., and A.M. Smith, Daytime Trapped Electron Intensities at High Latitudes at 1100 Kilometers, *J. Geophys. Res.*, **70**, 541-556, 1965.
- Williams, D.J., A 27-Day Periodicity in Outer Zone Trapped Electron Intensities, *J. Geophys. Res.*, **71**, 1815-1826, 1966.
- Williams, D.J., J.F. Arens, and L.J. Lanzerotti, Observations of Trapped Electrons at Low and High Altitudes, *J. Geophys. Res.*, **73**, 5673-5696, 1968.
- Wygant, J.R., P.R. Harvey, D. Pankow, F.S. Mozer, N. Maynard, H. Singer, M. Smiddy, W. Sullivan, and P. Anderson, CRRES Electric Field/Langmuir Probe Instrument, *J. Spacecraft and Rockets*, **29**, 600-604, 1992.

APPENDIX A

COORDINATE SYSTEMS

The coordinate systems which are used throughout this thesis are defined here [Bhavnani and Vancour, 1991]. They are all Earth - centered coordinate systems.

1. Earth Centered Inertial (ECI)

X-axis: Points in the direction of Aries and is in the equatorial and ecliptic planes.

Y-axis: Completes a right-handed orthogonal set, $\mathbf{Y} = \mathbf{Z} \times \mathbf{X}$, and lies in the equatorial plane.

Z-axis: Coincident with the Earth's rotational axis and is positive towards north.

2. Geocentric Solar Magnetospheric (GSM)

X-axis: Points to Sun.

Y-axis: Perpendicular to the magnetic dipole axis and is positive towards dusk. Axis lies in the geomagnetic equatorial plane and completes a right-handed orthogonal set, $\mathbf{Y} = \mathbf{Z} \times \mathbf{X}$.

Z-axis: Perpendicular to the X-axis and in the plane containing the X-axis and the magnetic dipole axis. It is positive towards north.

3. Solar Magnetic (SM)

X-axis: Perpendicular to the Z-axis and is in the plane containing the Z-axis and the Sun. Positive towards the Sun but does not necessarily point directly at the Sun. Lies in the geomagnetic equatorial plane.

Y-axis: Perpendicular to the Earth-Sun line (positive towards dusk) and lies in the geomagnetic equatorial plane. Completes a right-handed orthogonal set, $\mathbf{Y} = \mathbf{Z} \times \mathbf{X}$.

Z-axis: Coincident with the magnetic dipole axis and is positive towards north.

4. Geocentric Solar Ecliptic (GSE)

X-axis: Points to Sun and is in the ecliptic plane.

Y-axis: Completes a right-handed orthogonal set, $\mathbf{Y} = \mathbf{Z} \times \mathbf{X}$.

Z-axis: Perpendicular to the ecliptic plane and is positive towards north.

The GSE coordinate system is defined by an X-axis which points directly to the Sun. Because the CRRES spin axis was pointed $\sim 5^\circ$ from the Sun, the GSE coordinate are modified slightly to give mGSE coordinates.

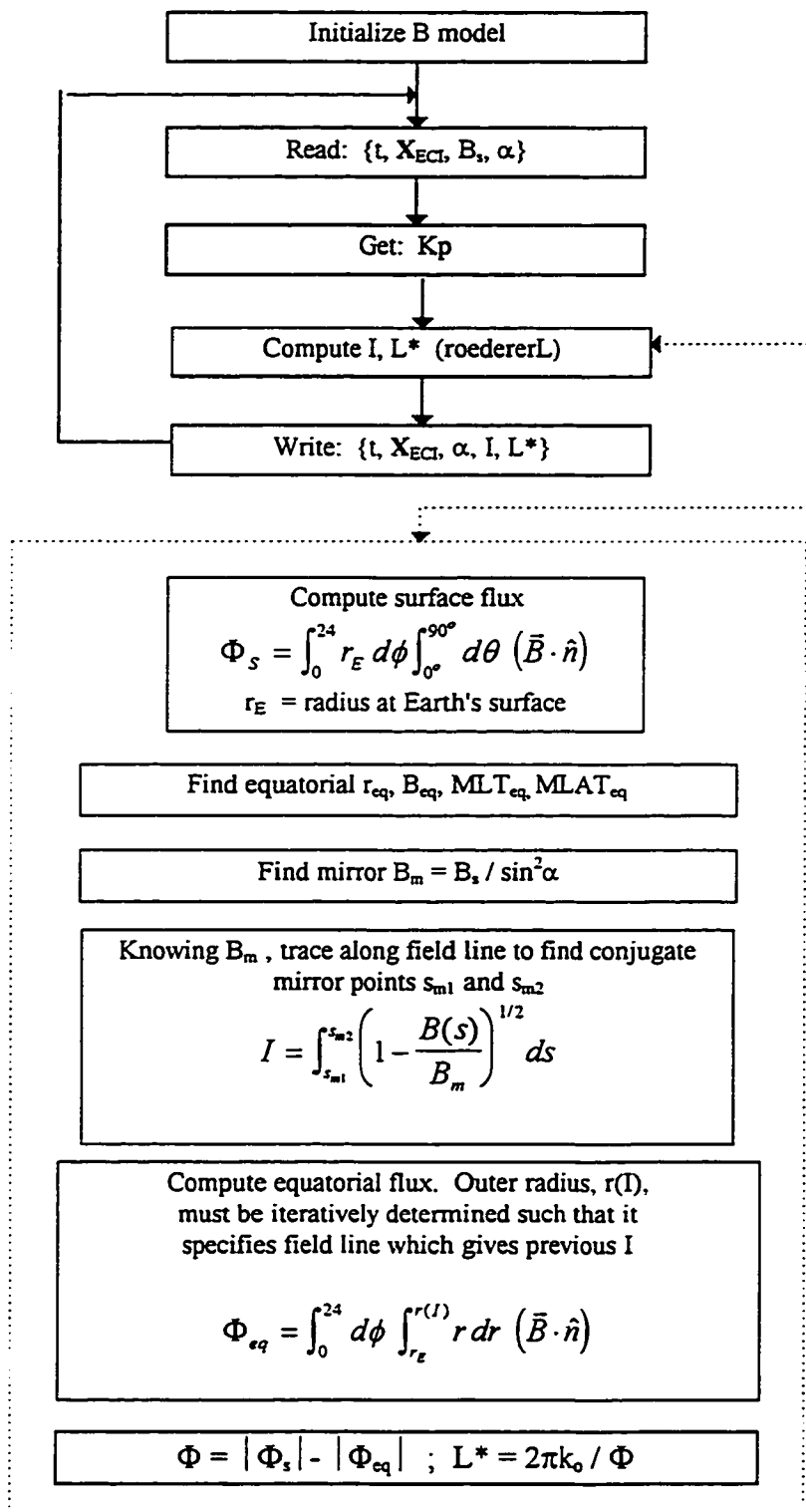
APPENDIX B

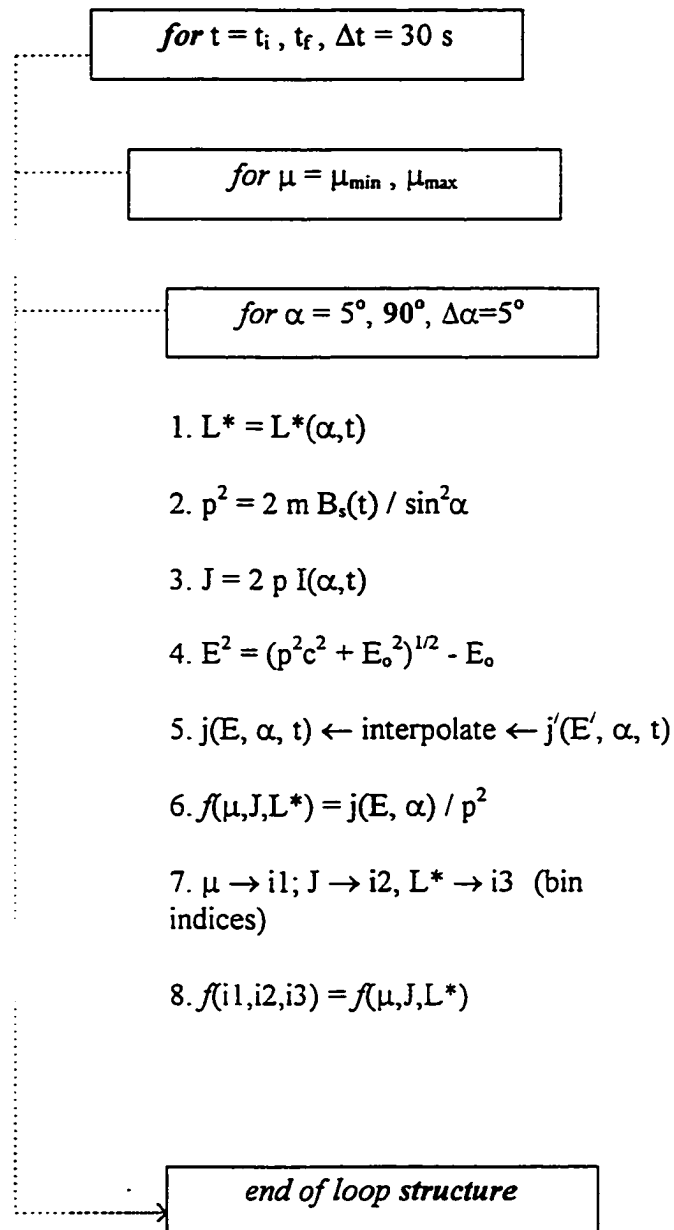
COMPUTER PROGRAM FLOW DIAGRAMS

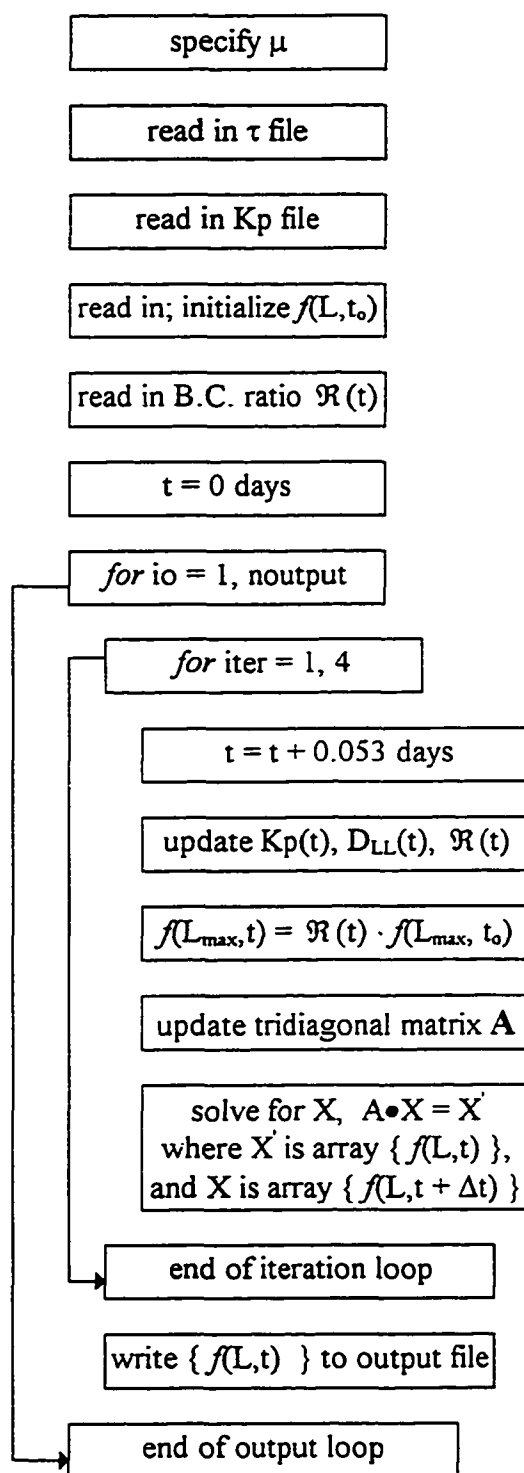
The flow diagrams for the three major computer programs used in this thesis are presented in this appendix. The program *roederer.f* (Figure B.1) calculates the second and third adiabatic invariants (J, L^*). The subroutine *roedererL* is the main subroutine which directs the calculation and its main algorithms are outlined within the dotted structure in Figure B.1. The subroutine *roedererL* was written by Dr. Jay Albert of Boston College, and accesses other significant routines including that for computing the Tsyganenko 1989 magnetic field model [Tsyganenko, 1989], auxiliary routines for interfacing with the T89 model (Dr. Robert Hilmer of Boston College), and commercial numerical routines [Press, et al, 1988].

The program *aibin.c* (Figure B.2) uses the output from *roederer.f* to convert a file of differential flux $j(E, \alpha)$ to a file of phase space density $f(\mu, J, L^*)$.

The program *rdiffuse.f* (Figure B.3) is a modified version of a radial diffusion program written by Dr. Jay Albert of Boston College [Albert, 1994] which solves the diffusion equation using finite difference algorithms. The original code was modified to incorporate time dependent diffusion coefficients, time dependent boundary conditions, and initial $f(L)$ from CRRES data. The routine for inverting the matrix equation is from Press, et al. [1988].

roederer.fFigure B.1 : Flow diagram for *roederer.f*.

aibin.cFigure B.2 : Flow diagram for *aibin.c*.

rdiffuse.fFigure B.3 : Flow diagram for *rdiffuse.f*.